

UNIVERSITY OF CALIFORNIA
Los Angeles

**Nano- and Microscale Architectures
for Energy Storage Systems**

A dissertation submitted in partial satisfaction of the
requirements for the degree Doctor of Philosophy
in Chemistry

by

Lisa Dudek

2014

UMI Number: 3608235

All rights reserved

INFORMATION TO ALL USERS

The quality of this reproduction is dependent upon the quality of the copy submitted.

In the unlikely event that the author did not send a complete manuscript and there are missing pages, these will be noted. Also, if material had to be removed, a note will indicate the deletion.



UMI 3608235

Published by ProQuest LLC (2014). Copyright in the Dissertation held by the Author.

Microform Edition © ProQuest LLC.

All rights reserved. This work is protected against unauthorized copying under Title 17, United States Code



ProQuest LLC.
789 East Eisenhower Parkway
P.O. Box 1346
Ann Arbor, MI 48106 - 1346

ABSTRACT OF THE DISSERTATION

Nano- and Mesoscale Architectures For Energy Storage Systems

by

Lisa Dudek

Doctor of Philosophy in Chemistry

University of California, Los Angeles, 2014

Professor Sarah H. Tolbert, Chair

The properties of a material as given by the crystal structure can be modified or changed completely by the microstructure architecture. Properties attributed to an insignificant fraction of the material, such as the surface atoms or defect sites, can become material-dominant properties if that fraction of the material is amplified through an appropriate architecture. High surface area forms, in which the material is predominantly surface sites, can have completely different properties than a non-architected material of the same composition.

In the first part of this work, we discuss coatings to enable microarchitectures for 3D microbatteries. 3D batteries require high surface area structures in order to expand their electrode mass per limited footprint. Increased electrode magnitudes allow a battery to store more energy, and utilizing a high surface area design allows this without increasing ion diffusion distances as would

thick monoliths of equivalent electrode mass. A variety of anodes and cathodes have been designed and tested following this principle, and require new electrolyte coatings to be developed to suit them. We design and instrument to deposit these coatings, and demonstrate plasma polymerized PEO-like polymer coatings as versatile solid state electrolyte films that should be compatible with a variety of 3D microbattery architectures. Our electrolyte coatings are analyzed by impedance spectroscopy, and their ionic conductivity is compared amongst various classes of depositions and various Li-ion concentrations.

In the second part of this work, we explore the versatility of nano-architected materials. High surface area iron oxide aerogels have already been discovered to be useful scaffolds for the paramagnetic iron oxide nanoparticles that form *in situ* in aerogel synthesis. We have found that the high concentration of surface defects in this material give the aerogels high capacities >100 mAh/g as Li-ion cathodes. Additionally, nanoporous silicon has already been discovered to add stability to and extend the cycle life of silicon as a Li-ion anode. We explore the versatility of this material for the use as anodes in other battery chemistries.

The dissertation of Lisa Dudek is approved.

Richard B. Kaner

Bruce Dunn

Sarah H. Tolbert, Chair

University of California, Los Angeles

2014

*To my parents,
who taught me to read,
encouraged me to think,
and believed I'd succeed*

TABLE OF CONTENTS

List of Figures.....	ix
List of Tables.....	xix
Acknowledgements.....	xx
Vita.....	xxiii
Publications.....	xxiv
Presentations.....	xxv

CHAPTER 1.

Introduction.....	1
1.1 References.....	4

CHAPTER 2. Design and Construction of an Instrument for Plasma Polymer

Deposition	8
2.1 Introduction.....	8
2.2 Power Source and Choice of RF Coupling Mechanism.....	13
2.3 Manifold for Pressure and Flow Control.....	20
2.4 Conclusions.....	25
2.5 References.....	26

CHAPTER 3. Plasma Deposited PEO-like Electrolyte Coatings for Li-ion

Batteries	29
3.1 Introduction.....	29
3.2 Results and Discussion.....	34

3.2.1	Chemical and Structural Analysis.....	34
3.2.2	Electrochemical Analysis.....	42
3.3	Conclusions.....	57
3.4	Experimental.....	58
3.4.1	Instrumentation and Deposition.....	58
3.4.2	Preparation for Analysis.....	59
3.4.3	Physiochemical Characterization.....	60
3.4.4	Electrochemical Characterization.....	61
3.5	References.....	62

CHAPTER 4. Iron Oxide Aerogels as Enhanced Cathode Materials for Li-ion

Charge Storage	66	
4.1	Introduction.....	66
4.2	Results and Discussion.....	68
4.2.1	Physiochemical Nature of FeO_x Aerogels.....	68
4.2.2	Electrochemistry.....	74
4.3	Conclusions.....	79
4.4	Experimental.....	79
4.4.1	Synthesis and Processing.....	80
4.4.2	Characterization and Instrumentation.....	81
4.5	References.....	82

CHAPTER 5. Beyond Li-ion: Silicon as a Host for Emerging Energy Storage

Systems	85
----------------------	----

5.1	Introduction.....	85
5.2	Experimental.....	89
5.2.1	Thin Film Silica Preparation.....	89
5.2.2	Magnesium Reduction.....	90
5.2.3	Electrochemical Setup.....	90
5.2.4	Sample Weight Measurement Preparation.....	91
5.2.5	Analysis Technique.....	91
5.3	Results and Discussion.....	92
5.3.1	Physiochemical Analysis.....	92
5.3.2	Li^+ Intercalation.....	94
5.3.3	Electrochemical Exploration of the Monovalent Cations Na^+ and K^+	94
5.3.4	Electrochemical Exploration of the Divalent Cation Mg^{2+}	104
5.4	Conclusions.....	108
5.5	References.....	109
CHAPTER 6. Conclusions.....		113

LIST OF FIGURES

CHAPTER 2. Design and Construction of an Instrument for Plasma Polymer Deposition

Figure 2.1. Some common results of an impact between electrons and gas phase species in a plasma.³ Elastic collisions occur, transferring energy from electrons to atoms. These are fewer in a cold plasma, resulting in separate electron temperatures and plasma temperatures (temperature of the gas phase species). The energy of the impact can also affect the electronic structure of the atom or molecule. At low energies, excitation to a higher AB orbital (AB*) is possible. This species can relax radiatively to produce the glow associated with plasmas. Higher energies excite molecules into a state resulting in homolytic bond cleavage and the formation of 2 radical species (A+B). These drive the plasma polymerization deposition. More energy results in ionization, creating an AB⁺ state, and providing electrons to sustain the plasma. The ionization of either the AB* or the A+B states requires less energy, as those states exist at a higher energy than ground state.....10

Figure 2.2. (left) diagrams of each of the 3 main mechanisms for coupling RF power to a plasma. Capacitively coupled plasmas have internal electrodes and create sputtering conditions. The electrodeless plasmas both have inductive components, but the

external coil is referred to as an inductively coupled plasma, while an external set of rings is referred to as a capacitively couple plasma. Both of these electrodeless plasmas can be optimized for conformal coatings. (right) the mechanism of coupling of a inductively coupling plasma. Inductively, both a magnetic field and a current are induced in the plasma. Capacitively, a linear current is also introduced, which aligns with the induced magnetic field.....14

Figure 2.3. A commercial variant on a low-pass pi matching network was used to match the impedance of the plasma load to the impedance of the RF generator. This allowed for maximum power to be delivered to the load.....16

Figure 2.4. (top) High powered plasmas arc through the monomer inlet and other tube narrowings. (bottom) Lower powered plasmas are either uneven in the coil (shown), or flicker on and off.....18

Figure 2.5. Schematic of a Baratron capacitive etch manometer, showing the mechanism of pressure sensing through capacitive connections to a mobile diaphragm, and the protective, heated, baffle (which is arranged to force a more complicated vapor pathway than depicted.....22

Figure 2.6. Four configurations of the gas manifold with RF power coupled through an external electrode to the vapors inside of the deposition chamber in order to create a plasma. (top left) inductive coupling with a downstream substrate region. (top

right) electrodeless capacitive coupling with a downstream substrate region. (bottom left) electrodeless capacitive coupling with an upstream deposition region. The chamber is heated to allow for increased vapor transport distances. (bottom right) a specific deposition region just at the afterglow is not heated in order to promote plasma deposition.....24

CHAPTER 3. Plasma Deposited PEO-like Electrolyte Coatings for Li-ion Batteries.

Figure 3.1. The XPS spectrum of a representative plasma polymerized PEO-like film. The C (2p) region is shown, and the solid blue trace is the measured spectrum. It can be seen that there are four distinct envelopes in our spectra. These envelopes are fit to peaks matching the oxidation states of aliphatic oxygen-containing hydrocarbons, and the resulting coalesced fit is shown in a dotted light blue line, which has a good overlay with the original spectrum.....36

Figure 3.2. A comparison of the XPS spectra for representatives from each of the 3 classes of plasma deposition: a purely PEO-like deposition with no adhesion layer (AL), PEO deposited over a 1s adhesion blast, and PEO deposited over a 1, 2, or 3-minute AL. These 3 depositions are also compared to the XPS of a substrate subjected to the 1s adhesion blast, but removed from the deposition chamber without any further deposition.....38

Figure 3.3. AFM height profiles for each class of plasma polymer film, deposited on ITO. All scale bars are 800 nm. (top left) a PEO-like film with no adhesion layer shows a height profile below 5 nm. (top middle) a 1 second adhesion blast layer with no PEO-like over-layer. (top right) a PEO-like film over the 1 second adhesion blast. (bottom left) a PEO-like layer over a 1 minute adhesion layer. (bottom center) a PEO-like film over a 2 minute adhesion layer. (bottom right) a PEO-like film over a 2 minute adhesion layer. Early (1 second and 1 minute) adhesion layer depositions are slightly rougher than the PEO-like over-layers and longer adhesion layer depositions. PEO-like films with no adhesion layers are noticeably flatter.....40

Figure 3.4. Representative Bode plots for a film without an adhesion layer. The data shown belongs to a film with an adhesion blast, but the PEO-like films with no adhesion layers show the same characteristic Bode and Nyquist plots. The red trace is for the film after lithiation, and the blue trace is for the un-lithiated control. (top) the phase angle between current and voltage as a function of frequency. -90° is characteristic of a capacitor, and 0° is characteristic of a conductor. (bottom) the overall impedance of the film—including resistive and reactive components—as a function of frequency. A linear trace is characteristic of a capacitor, and a constant value is characteristic of a conductor.....46

Figure 3.5. The geometric average of salt concentrations for (left) PEO-like films with no adhesion layer, and (right) PEO-like films deposited over a 1s adhesion blast, as a function of the applied salt concentration. Geometric standard deviations are reported for each average.....48

Figure 3.6. Bode and Nyquist plots of the impedance spectra for representatives of each class of film. a) In the upper Bode plot, the phase angle between the current and the voltage goes to -90° for a capacitor and 0° for a conductor. 2 separate frequency-dependent conductivity regimes are evident for films with 2 min adhesion deposition. In the lower Bode plot, the impedance y-axis value becomes constant for a conductor. For the 2 min adhesion deposition film, a small inflection is seen near 1E+4 Hz, representing the same, lower impedance, conductivity regime clearly represented in the phase angle data. b) Nyquist plots calculated from the same data used to create the Bode plots in Figure 3.6a. Each arc represents one conduction regime in the material measured. c) The low impedance regime for the Nyquist plot in Figure 3.6b, showing the beginning of a low impedance arc for the adhesion layer film (corresponding to the inflection in each Bode plot). The dotted line is the simulated fit values for the equivalent circuit, which gives the resistance at the small arc's extrapolated x-intercept.....50

Figure 3.7. Geometric average values of impedance for both the adhesion

layer and the PEO-like layer deposited over the adhesion layer. The adhesion layer has much higher impedance values than seen for the PEO-like layers in each of the 3 film classes, which was expected due to higher cross-linking, and lack of much of the functionality required to coordinate lithium ions. The PEO- like layer shows conductivities similar to the other PEO-like plasma polymers studied, but does not improve upon them.....	53
Figure 3.8. Environmental SEM images of a 3D microbattery post array. All scale bars are 20 μm . The left column shows the uncoated posts arrays at various magnification. The colloidal microstructure is clearly visible. The right column shows a post array after a plasma polymer PEO-like coating was deposited. The colloidal microstructure is filled in but the underlying construction is still visible.....	56

CHAPTER 4. Iron Oxide Aerogels as Enhanced Cathode Materials for Li-ion Charge Storage.

Figure 4.1. Powder X-ray diffraction for the four FeO_x aerogels, after background subtraction. The patterns are indexed relative to the JCPDS patterns for Fe_3O_4 and $\gamma\text{-Fe}_2\text{O}_3$. It can be seen that the argon processing induces crystallization into the magnetite/maghemite phase. No extraneous hematite is seen in any of the processing conditions (although it would be expected in air at higher temperatures)	69
--	----

Figure 4.2. Transmission electron microscopy of the a) AS-SYN, (b) 260-AIR, (c) 260-ARGON, and (d) 260-ARGON-AIR materials.....	71
Figure 4.3. Pore volume distribution from BHJ desorption using Broekhoff-de Boer thickness calculations. Shown above is the full scale pore volume for all four aerogels, and below is the same data for the three heat treated aerogels on a reduced pore volume scale.....	73
Figure 4.4. Cyclic voltammetry for each aerogel in a coin cell against Li. The sweep rate was 0.5mV s^{-1} , and cycles 2 and 3 are shown for each material. The defect-rich AS-SYN and 260-AIR materials show higher capacities than the reduced 260-ARGON material.....	75
Figure 4.5. Galvanostatic cycling of each material against Li in coin cells (gravimetric). Whereas the initial high capacity of the AS-SYN material fades with cycling, the 260-AIR material has much improved capacity retention. 260-ARGON has a much lower capacity, and 260-ARGON-AIR recovers capacity but remains lower than the non-crystalline samples.....	77
Figure 4.5. Surface-area normalized galvanostatic cycling. 260-ARGON-AIR regains its capacity per surface area as compared to the higher surface area 260-AIR material. 260-ARGON has a lower capacity than can be accounted for by its lower surface area, and AS-SYN cannot take advantage of its high surface area without further heat treatments.....	78

CHAPTER 5. Beyond Li-ion: Silicon as a Host for Emerging Energy Storage

Systems

Figure 5.1. A summary of physical characterization and Li-ion intercalation studies of templated porous Si films from previous work in submission by C. Kang. (a) SEM of silica, scale bars are 100 nm. (b) same film after magnesylation followed by HCl/HF treatment. (c) low angle XRD of templated mesoporous silica and silicon. After magnesylation, diffraction peaks shift to lower angle, indicating pore shrinkage in the out-of-plane direction. (d) high-angle XRD, after Mg treatment. Diffraction peaks corresponding to crystalline Si at 17.5, 29.0, and 34.0 nm⁻¹. Peaks corresponding to MgO at 22.5, 26.5, and 28.0 nm⁻¹. After acid treatment, MgO peaks disappear and only Si peaks remain. (e) CV of porous magnesylated and acid-washed Si at 50 mV/s. (f) galvanostatic cycling of templated porous Si. The rate was 1 A/g, corresponding to approximately 1C.....93

Figure 5.2. Cyclic voltammogram of a porous silicon thin film in a sodium perchlorate flooded cell vs a sodium reference electrode, at 4 mV/s. The first 2 cycles are shown, and the capacity does not appear to fade between cycles.....96

Figure 5.3. Galvanostatic cycling of porous silicon thin films in a sodium perchlorate flooded cell. In each case, the capacity over many cycles is shown on the left. To the right, the capacity for a selection of cycles is displayed. The slower rate of 10 µA leads to a much higher capacity in initial cycles, but only a slightly

improved capacity approaching 100 cycles.....	97
Figure 5.4. (left) cyclic voltammogram and (right) galvanostatic cycling of a porous silicon thin film in potassium perchlorate. Capacities are negligible beginning in early cycles.....	99
Figure 5.5. Galvanostatic cycling of a porous silicon thin film in a magnesium perchlorate flooded cell, at 1e-5 A. The film showed a negligible capacity, with only ~ 1 mAh/g per cycle.....	102
Figure 5.6. Cyclic voltammogram of a porous silicon thin film in a magnesium perchlorate flooded cell. The material was cycled three times at each voltage window: from 2 V to 0 V, to -1 V, to -2 V, to -2.5 V, and to -3 V. On the first cycle of each of the voltage windows above -2 V, the SEI layer forms. Each time negligible current is seen on the oxidation sweep, suggesting that the reduction current is from an irreversible process, such as SEI formation, and not due to magnesium insertion. On the second and third cycle, no current is seen on either sweep, suggesting that the silicon surface has grown a self-limiting SEI at these voltages. However upon increasing the reductive voltage, a new SEI-forming region is exposed. Once below -2 V vs the Ag pseudoreference, SEI formation is finished and no further capacity is seen.....	103
Figure 5.7. Pre-lithiation by galvanostatic cycling of a porous silicon thin film in lithium perchlorate, including the initial SEI-forming step. By the third cycle, the film is expected to be amorphous.	

After 5 cycles, the film was lithiated one final time (shown).....106

Figure 5.8. Galvanostatic cycling of a porous silicon thin film that has been pre-lithiated and is amorphous. The film underwent an oxidation step in the magnesium perchlorate before cycling to remove lithium, and the film was held at 2 V vs the Ag pseudoreference in order to ensure all of the lithium was removed. An improved Mg capacity is seen compared to silicon films that are crystalline and have not been pre-lithiated.....107

LIST OF TABLES

CHAPTER 3. Plasma Deposited PEO-like Electrolyte Coatings for Li-ion Batteries

Table 3.1 Summary of height variation and roughness of plasma films by AFM.....	41
---	----

ACKNOWLEDGEMENTS

I would first like to thank my advisor, Sarah Tolbert, without whom I wouldn't be here today. She always supported me in my most ambitious research schemes, and I am grateful for the opportunity she gave me to dream big.

I would like to acknowledge my committee members, Professors Richard Kaner and Bruce Dunn, for their support, especially in the final stretch, and Professor Paul Weiss for serving on my qualifying committee.

Thank you to my collaborators, especially those who helped in the design and construction of the plasma instrument in Chapter 2. I received invaluable advice on plasmas and RF electronics from Professor Francis Chen, Dr. Nathan Marchack, Dr. Joseph Nemanick, and most especially Dr. Winston Ciridon at the University of Washington in Seattle, who hosted me for a tour of his plasma instruments in the lab of Professor Buddy Ratner, and lent me the matching network I used for all of my depositions. Under the direction of Professor Bruce Dunn, Dr. Daniel Membrano worked with me on all the impedance data collection in Chapter 3. Dr. Laura Schelhas spent many weekends and early mornings gathering XPS for each film studied for impedance in chapter 3, as well as for countless more coatings analyzed in the optimization of the plasma instrument and in the following optimization of the PEO-like films.

I would like to thank Dr. Benjamin Hahn for being my mentor and collaborator on a variety of iron oxide projects, including the work in Chapter 4, while I was on internship at the Naval Research Labs. He went above and beyond even to the extent of sharing his bench top, which my samples at times

overwhelmed. Often times. Sorry Ben! I am eternally grateful to my internship advisor Dr. Debra Rolison, for welcoming me into her lab group. I thoroughly enjoyed my summer in your lab group, the opportunity to have you as a mentor, and the many conversations I had with you and all your group members both in lab and over coffee breaks or lunches.

I am and will always be grateful to Dr. Carolyn Knobler for always believing in me. Without her mentorship and words of wisdom, the struggle may have overwhelmed me. Thank you for all your time and kind words. You were the key reason I regained hope and re-committed to this degree on at least 2 occasions. The last time we spoke, you saw a strength and passion in me that I did not think I possessed anymore. Thank you for giving that strength back to me.

I have had the incredible good fortune to be joined in the doctoral trenches with some of the most amazing minds, and the best friends I could ever ask for. Dr. Christina Baker, my Apple Pan recruiter, whose office was my second on-campus home during my first year, and whose house has been my second home throughout graduate school. My first office-roommate and fellow salty oatmeal aficionado, Selma, for all the front lawn lunch breaks and pep talks that got me through the first two years. Beware: some birthday you'll come home again to find Iris and me in your living room. Thanks to Dr. Rachel Harper, my good friend, critic, therapist, neighbor, and Erin-wrangler. I can still hear you some nights at 4 AM, saying, "So, imagine an L, with one side shorter than the other. . ." No matter what you were going through, or how many days you'd gone without sleep, you always had time to keep the rest of us from imploding. To Dr. Iris Rauda, my dear friend and chair space competitor with whom I shared an office for 4 years that did

not actually have room for the both of us. We became close in only a way that people who sit an inch apart can be. We made it through the tough middle years of grad school together and saw each other through the final stage. I don't know how I would have made it to the end without you.

I am so appreciative, lucky, and thankful to have Thom by my side, who intuitively knows exactly what I need to feel grounded. You view every one of my challenges as a team effort, and kept finding ways to take more and more off my shoulders as the thesis piled more and more on. I also have to thank you for seeing the person behind the insanity while I've been finishing. I love you. And thank you to the Buckwalters, who lent me their living room to haunt all hours of day and night while writing this thesis.

Lastly, I would like to thank my parents and siblings, who have always supported me in all of my endeavors. My father, who taught me the importance of a good handshake, and who gave me my first early lessons in electronics and hardware. My mother who always thought we could do anything, especially after someone else told us that we couldn't. And whose question of "Are you done yet?" I can finally answer.

The work in this dissertation was supported by: The Materials Creation Training Program (MCTP) IGERT Fellowship, the California NanoSystem Institute (CNSI); the National Science Foundation (NSF); the Office of Naval Research (ONR); Darpa; Naval Research Labs (NRL); and the UCLA Graduate Division.

VITA

2002	National Merit Scholarship Award Recipient
2002-2006	Eberly College of Science Braddock Fellowship from the Pennsylvania State University
2003	NSF REU Recipient at the University of Georgia
2004	NSF REU Recipient at California State University, Fullerton
2006	B.S. in Chemistry, the Pennsylvania State University
2006	B.S. in Biochemistry and Molecular Biology, the Pennsylvania State University
2006-2007	First Year Graduate Division Award Fellowship at UCLA
2010-2012	NSF IGERT Fellowship in the Materials Creation Training Program (MCTP) at UCLA
2011	Visiting Scholar at the Naval Research Lab (NRL) in Washington, DC

PUBLICATIONS

Lisa Dudek, Daniel Membrano, CJ Kim, Bruce Dunn, Sarah Tolbert. "Plasma deposited PEO-like electrolyte coatings for Li-ion batteries." **2014**, *In Preparation*.

Lisa Dudek, Benjamin P. Hahn, Jeffrey W. Long, Joseph F. Parker, Katherine A. Pettigrew, Debra R. Rolison. "Rust as a viable cathode material for lithium-ion batteries: high surface area aerogels." **2014**, *In Preparation*.

Joseph Nemanick, **Lisa Dudek**, Richard Farrell, Jacob Cox, Sarah Tolbert. "Porous silicon nanowire arrays for Li-ion battery anodes." **2014**, *In Review*.

David Tranchemonagne, **Lisa Dudek**, Omar M. Yaghi. "Synthesis of Metal-Organic Frameworks: MOF-5 and MOF-177." *Inorganic Syntheses*, **2010**, 35, 102-108.

PRESENTATIONS

Lisa Dudek, Benjamin P. Hahn, Jeffrey W. Long, Katherine A. Pettigrew, Debra R. Rolison. "Iron oxide aerogels as cheap and safe active materials for Li-ion cathodes." Oral Presentation at the Gordon Electrochemistry Symposium, Ventura, CA, **January 2012**.

Lisa Dudek, Daniel Membrano, Laura Schelhas, CJ Kim, Bruce Dunn, Sarah Tolbert. "Plasma polymerized PEO-like electrolyte coatings for high aspect ratio electrodes in 3D Li-ion microbatteries." Oral Presentation at the ACS 244th National Meeting, Philadelphia, PA, **August 2012**.

Lisa Dudek, Jeffrey W. Long, *Benjamin P. Hahn*, Katherine A. Pettigrew, Debra R. Rolison. "Enhancing electrochemical energy storage in insertion oxides by creating cation vacancies." Oral Presentation at the MRS Spring Meeting, San Francisco, CA, **April 2012**.

Lisa Dudek, Jeffrey W. Long, *Benjamin P. Hahn*, Joseph F. Parker, Katherine A. Pettigrew, Debra R. Rolison. "Redesigning iron oxides in nanoscale and defective forms for enhanced electrochemical storage in rechargeable lithium batteries." Oral Presentation at the ACS 243rd National Meeting, San Diego, CA, **March 2012**.

Lisa Dudek, Daniel Membrano, Laura Schelhas, CJ Kim, Bruce Dunn, Sarah Tolbert. "PEO-like plasma-polymerized electrolyte coatings for 3D microbatteries." Oral Presentation at the ACS 243rd National Meeting, San Diego, CA, **March 2012**.

Lisa Dudek, Daniel Membrano, Laura Schelhas, CJ Kim, Bruce Dunn, Sarah Tolbert. "PEO-like plasma-polymerized electrolyte films for 3D microbatteries." Oral Presentation at the Naval Research Labs (NRL) Surface Chemistry Branch Seminar, Washington, DC, **May 2011**.

Lisa Dudek, Daniel Membrano, Laura Schelhas, CJ Kim, Bruce Dunn, Sarah Tolbert. "Plasma polymer electrolyte coatings for 3D microbatteries." Recorded Oral Presentation at the Annual National IGERT Summit (accompanying a poster), online: <http://www.igert.org/posters2011/posters/25>, **May 2011**.

Lisa Dudek. "Motivation and Methods for 3D Battery Architectures." Oral Presentation at the Second Annual Joint IGERT UCLA (MCTP) and UCSB (ConvEne) Symposium, UCSB, Santa Barbara, CA, **November 2010**.

Lisa Dudek, Daniel Membrano, Laura Schelhas, CJ Kim, Bruce Dunn, Sarah Tolbert. "PEO-like electrolyte films for 3D lithium-ion batteries." Oral Presentation at the Materials Creation Training Program Ninth Annual Symposium, UCLA, Los Angeles, CA, **November 2010**.

CHAPTER 1

Introduction

The properties of a material as given by the crystal structure can be modified or changed completely by the microstructure architecture. Properties attributed to an insignificant fraction of the material, such as the surface atoms or defect sites, can become material-dominant properties if that fraction of the material is amplified through an appropriate architecture. The properties that can be enhanced or added are varied and material-dependent, but often stem from 1) the greatly enhanced surface areas introduced by the architecture, 2) the ability to arrange non-aggregated particles or clusters in space, or 3) the addition of open transport paths through the material. In this work, we study how these advantages can be applied to materials problems faced in energy storage.

There is currently a focus on the design of nano-architected materials for energy storage.¹ Higher surface areas through templated mesoporous inorganic frameworks,² vanadium oxide aerogels,^{3,4,5,6} and various forms of clean room processed architectures^{7,8,9,10} are useful for increased rate capabilities, because they decrease the diffusion distances that ions travel through the material. Higher surface areas also increase capacities through increased surface energy storage in applications like non-faradaic supercapacitors, and also in the higher energy-storing pseudocapacitors. In non-faradaic capacitive energy storage, increased architectures are available such as electrospinning to produce porous carbon¹¹ and controlled evaporation for shape-engineering of carbon nanotubes¹². Finally, high

surface area forms allow for more electrode mass in devices that would otherwise be limited in film thickness by their diffusion pathways.¹³

The ability to preserve the existing high surface area of nanoparticles by arranging them into a network also has been used extensively in energy storage. Similar techniques to the templated sol gel films can be used to template even higher surface area nanoparticle films.^{2,14,15,16} Aerogels similarly preserve the higher surface area of their sol-derived nanocrystals.³ In high surface area aerogel networks, a large fraction of the material is surface atoms. This introduces the possibility of introducing properties attributed to an insignificant fraction of surface defect sites as a bulk property of the resulting aerogel.

All of these techniques have the added advantage of creating open pathways through a material. These pathways allow for the delivery of ions and electrolyte to the active surfaces. The importance of adding “nothing” for wiring energy storage materials as well as materials for other applications has been written about extensively.^{3,17} Additionally, open spaces in a material allow for the decoupling of lattice expansion during energy storage to the bulk material expansion. Pores and open space on the nano- and microscale allow the material to absorb the expansion into the void spaces on those small scales, reducing bulk volume changes and improving cycle life.^{18,19}

In chapters 2 and 3 of this work, we look not at the creation of microscale architectures, but of their needs for the development of a coating. Microstructured electrodes have been created in order to miniaturize the battery for small applications such as on-chip or MEMS uses.¹³ These electrodes could be incorporated into 3D batteries, if they were coated with a solid state

electrolyte/separator film, such that the opposing electrode can be incorporated into the device without creating shorts. Combining the two ideas that gas phase coatings are conformal over 3D structures, and that polyethylene oxide (PEO) films function well as solid state electrolyte/separator coatings, we developed a gas (plasma) phase coating for PEO-like electrolyte films. We demonstrate the electrical resistance and ionic conductivity of our electrolyte films. Borrowing from PEO-like plasma films for bio-non-fouling, we examine the effects of adhesion layer depositions on the physiochemical properties and lithium impedance spectroscopy of the PEO-like films.

In chapter 4, we examine a normally Li-ion inert material such as iron oxide in a high surface area aerogel form. Nanoscale forms of iron oxide had been observed to insert lithium ion in a cathodic regime as an intercalation electrode.^{20,21,22} In the anodic regime, similar nanoscale forms insert Li^+ as conversion materials.^{21,23,24} While the conversion reactions can be destructive for deliberately designed architectures, intercalation reactions can be more easily tailored to preserve the original structure. We therefore used an aerogel network of iron oxide nanoparticles to examine a very high surface area format for the improvement of Li-ion intercalation at cathodic voltages. Our iron oxide aerogels are mostly composed of surface species, and so they utilize the reactive, vacancy rich iron oxide surface as the Li-insertion material. These architectures are also well-wired with a network of pores to allow for improved Li^+ and electrolyte access throughout the material.¹⁷

Finally, in chapter 5, we use a network of pores for a very different purpose; that of extending high silicon capacities for Li-ion applications to other energy

storage chemistries. Silicon has high capacities for Li-ion insertion and is the heir apparent for next generation Li-ion battery anode materials. However, the large insertion capacities lead to large volume expansions, which cause destruction of the silicon material and low cycle life. This can be improved by utilizing a porous architecture, as the pores can accommodate the volume expansion on the microscale, reducing bulk expansion.^{19,25,18} Porous forms of silicon should also have similar advantages for enhanced cycle life in regards to the insertion of other ions which can alloy with silicon. We explore the electrochemistry of Na^+ , K^+ , and Mg^{2+} in porous silicon films, and discuss future directions for exploration of these systems.

As a whole, this work suggests that nano- and microscale architectured materials can be designed in order to overcome a variety of problems in energy storage. Microscale post arrays are a path to the developments of 3D microbatteries. High surface area iron oxide aerogels enable enhanced reactivity of iron oxide, allowing for a new, low cost cathode material for Li-ion batteries. And templated porous silicon films have the capacity for the absorption of volume expansion that should enable new battery chemistries. Chapter 6 concludes with a summary of the work, including the insight that can be gained and future directions.

1.1 References

1. Baxter, J. *et al.* Nanoscale design to enable the revolution in renewable energy. *Energy Environ. Sci.* **2**, 559 (2009).
2. Brezesinski, T., Wang, J., Polleux, J., Dunn, B. & Tolbert, S. H. Templated

Nanocrystal-Based Porous TiO_2 Films for Next-Generation Electrochemical Capacitors. *J. Am. Chem. Soc.* **131**, 1802–1809 (2009).

3. Rolison, D. R. & Dunn, B. Electrically conductive oxide aerogels: new materials in electrochemistry. *J. Mater. Chem.* **11**, 963–980 (2001).
4. Dong, W., Sakamoto, J. S. & Dunn, B. Electrochemical properties of vanadium oxide aerogels. *Sci. Technol. Adv. Mater.* **4**, 3–11 (2003).
5. Passerini, S. *et al.* XAS and electrochemical characterization of lithiated high surface area V_2O_5 aerogels. *Solid State Ion.* **104**, 195–204 (1997).
6. Rhodes, C. P., Dong, W., Long, J. W. & Rolison, D. R. in *Solid State Ion.* **VI**, 478 (Electrochemical Society, 2003).
7. Wang, C. *et al.* C-MEMS for the Manufacture of 3D Microbatteries. *Electrochem. Solid-State Lett.* **7**, A435 (2004).
8. Notten, P. H. L., Roozeboom, F., Niessen, R. A. H. & Baggetto, L. 3-D Integrated All-Solid-State Rechargeable Batteries. *Adv. Mater.* **19**, 4564–4567 (2007).
9. Nathan, M. *et al.* Three-dimensional thin-film Li-ion microbatteries for autonomous MEMS. *J. Microelectromechanical Syst.* **14**, 879–885 (2005).
10. Kotobuki, M. *et al.* Effect of sol composition on solid electrode/solid electrolyte interface for all-solid-state lithium ion battery. *Electrochimica Acta* **56**, 1023–1029 (2011).
11. Bonso, J. S., Kalaw, G. D. & Ferraris, J. P. High surface area carbon nanofibers derived from electrospun PIM-1 for energy storage applications. *J. Mater. Chem. A* **2**, 418 (2014).
12. Futaba, D. N. *et al.* Shape-engineerable and highly densely packed single-

walled carbon nanotubes and their application as super-capacitor electrodes. *Nat. Mater.* **5**, 987–994 (2006).

13. Long, J. W., Dunn, B., Rolison, D. R. & White, H. S. Three-Dimensional Battery Architectures. *Chem. Rev.* **104**, 4463–4492 (2004).
14. Brezesinski, T., Wang, J., Tolbert, S. H. & Dunn, B. Ordered mesoporous a-MoO₃ with iso-oriented nanocrystalline walls for thin-film pseudocapacitors. *Nat. Mater.* **9**, 146–151 (2010).
15. Rauda, I. E., Augustyn, V., Dunn, B. & Tolbert, S. H. Enhancing Pseudocapacitive Charge Storage in Polymer Tempered Mesoporous Materials. *Acc. Chem. Res.* **46**, 1113–1124 (2013).
16. Rauda, I. E. *et al.* General Method for the Synthesis of Hierarchical Nanocrystal-Based Mesoporous Materials. *ACS Nano* **6**, 6386–6399 (2012).
17. Hahn, B. P., Long, J. W. & Rolison, D. R. Something from Nothing: Enhancing Electrochemical Charge Storage with Cation Vacancies. *Acc. Chem. Res.* **46**, 1181–1191 (2013).
18. Kim, H., Han, B., Choo, J. & Cho, J. Three-Dimensional Porous Silicon Particles for Use in High-Performance Lithium Secondary Batteries. *Angew. Chem. Int. Ed.* **47**, 10151–10154 (2008).
19. Yao, Y. *et al.* Interconnected Silicon Hollow Nanospheres for Lithium-Ion Battery Anodes with Long Cycle Life. *Nano Lett.* **11**, 2949–2954 (2011).
20. Hahn, B. P. *et al.* Electrochemical Li-ion storage in defect spinel iron oxides: the critical role of cation vacancies. *Energy Environ. Sci.* **4**, 1495–1502 (2011).
21. Thackeray, M. M. Spinel electrodes for lithium batteries. *J. Am. Ceram. Soc.* **82**, 3347–3354 (1999).

22. Pernet, M., Strobel, P., Bonnet, B. & Bordet, P. Structural and electrochemical study of lithium insertion into γ - Fe_2O_3 . *Solid State Ion.* **66**, 259–265 (1993).
23. Thackeray, M. M., David, W. I. F. & Goodenough, J. B. Structural characterization of the lithiated iron oxides $\text{Li}_x\text{Fe}_3\text{O}_4$ and $\text{Li}_x\text{Fe}_2\text{O}_3$ ($0 < x < 2$). *Mater. Res. Bull.* **17**, 785–793 (1982).
24. Koo, B. *et al.* Hollow iron oxide nanoparticles for application in lithium ion batteries. *Nanoletters* **12**, 2429–2435 (2012).
25. Wang, X.-L. & Han, W.-Q. Graphene Enhances Li Storage Capacity of Porous Single-Crystalline Silicon Nanowires. *ACS Appl. Mater. Interfaces* **2**, 3709–3713 (2010).

CHAPTER 2

Design and Construction of an Instrument for Plasma Polymer Deposition

2.1 Introduction

New methods for the conformal coating of electrolytes onto electrode microarchitectures are required in the development of 3D microbatteries. Thin film batteries rely primarily upon sputtered LiPON solid electrolyte films, which coat flat substrates but not architectured electrodes.¹ Gas phase coatings, such as ALD or plasma polymerization, could be ideal to coat these architectured electrodes.² Both ceramic materials similar to formulations deposited by ALD,^{3,4} and also polymeric materials^{5,6,7} similar to those deposited by plasma polymerization^{8,9} are known solid state electrolyte materials. However, materials suitable for conformal electrolyte coatings have not been developed for either deposition method. We have chosen to focus on plasma polymerization. In order to develop electrolyte coatings via plasma deposition, we first are required to construct an instrument for plasma deposition of organics.

Plasmas are ionized gasses, which, through an equivalent number of cations and electrons, maintain overall charge neutrality. In Figure 2.1 it can be seen that various excitations are possible when electrons collide with species in the gas phase, some of which lead to the formation of reactive radical species. The reaction of the radical species cause larger molecules to form in the gas phase, which eventually condense and form depositions. These depositions remain

exposed to the plasma, and continue to grow and react, as further condensation adds species to the growing film.

For our depositions, when we refer to plasmas, we are referencing cold plasmas, which are useful for the gentle parameter space required for deposition of functionalized organic species. The temperatures of electrons within a plasma are on the order of 20,000 to 100,000 K.¹⁰ However, in cold plasmas, the electrons and ions are not in thermal equilibrium. This occurs at lower pressures (<10 Torr) and lower ionizing currents, which result in fewer ionized species (~1 in 10,000), and results in ion and non-ionized gas species temperatures on the order of 300 to 1,000 K.¹⁰ The cooler plasma temperature is also more suitable to common materials for construction of a chamber for plasma deposition.

When plasma discharges are composed of or include organic species, the homolytic electron-impact dissociation referred to in Figure 2.1 results in reactive organic fragments, which recombine to make larger products.¹¹ If the conditions are optimized, the recombined product retains large functional pieces of the original organic precursor, and deposits as a cross-linked coating called a plasma polymer.

The instrument for deposition must be designed carefully and optimized in order to facilitate controlled recombination and deposition of these fragments.^{11,12,13} First, the precursor molecule must be introduced into the deposition chamber as a gas or vapor. This is made easier by the low pressures of the deposition process (<100 mTorr), and often requires that the gas manifold leading into the chamber be at controlled low pressures as well, and heated. The vapor phase precursor is exposed to electrodes at the deposition chamber, ionizing a percentage of molecules and creating a plasma discharge. Thus, the electrode configuration and

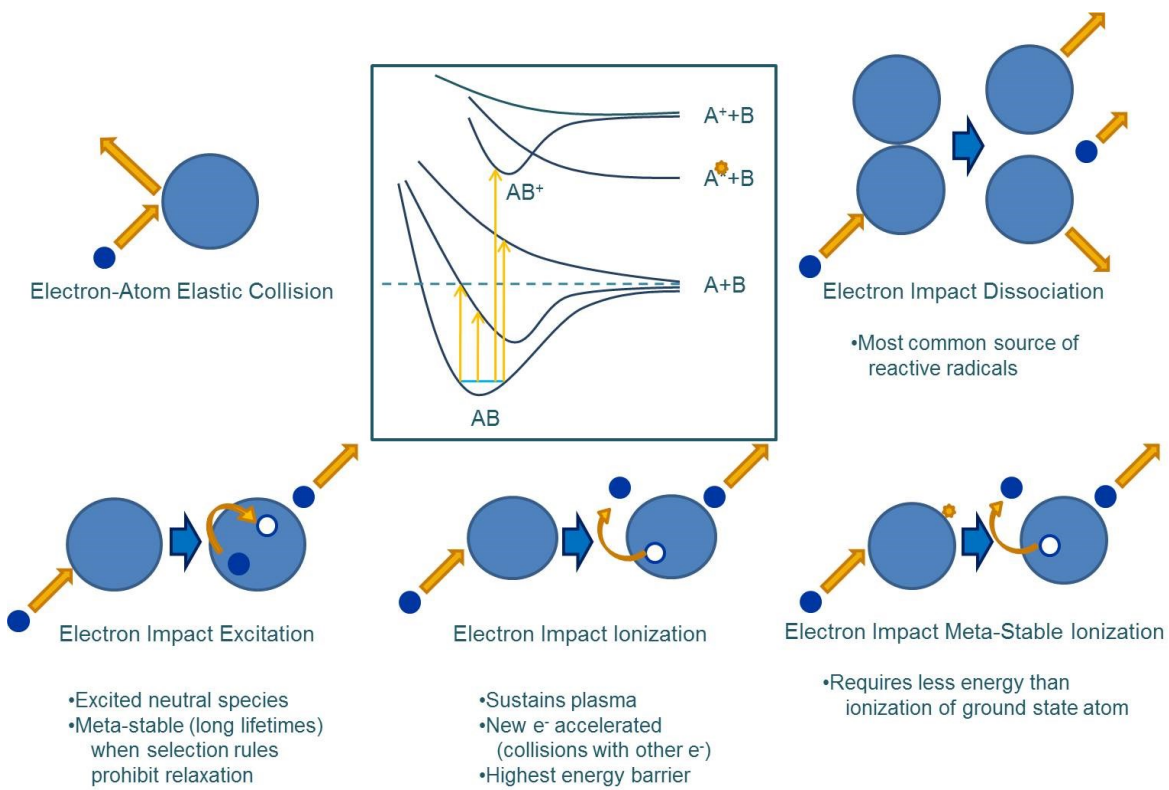


Figure 2.1. Some common results of an impact between electrons and gas phase species in a plasma.¹⁰ Elastic collisions occur, transferring energy from electrons to atoms. These are fewer in cold plasmas, resulting in separate electron temperatures and plasma temperatures (temperature of the gas phase species). The energy of the impact can also affect the electronic structure of the atom or molecule. At low energies, excitation to a higher AB orbital (AB^*) is possible. This species can relax radiatively to produce the glow associated with plasmas. Higher energies excite molecules into a state resulting in homolytic bond cleavage and the formation of 2 radical species ($A+B$). These drive the plasma polymerization deposition. More energy results in ionization, creating an AB^+ state, and providing electrons to sustain the plasma. The ionization of either the AB^* or the $A+B$ states requires less energy, as those states exist at a higher energy than ground state.

power delivery to the electrodes are also an important.¹¹ As mentioned above, in the resulting plasma discharge, some molecules undergo homolytic bond cleavage, forming 2 neutral radical fragments from the original precursor. The radical fragments are the basis for the deposited plasma polymer.

The deposition composition and deposition rate depends on a variety of plasma parameters that can be controlled, all of which are combined into one figure of merit: the energy input level is normalized by the mass of species in the gas phase (J/kg).^{11,13} The more mass is present in the chamber, the lower the fragmentation percent will be for any given applied energy. Conversely, the more energy applied to a given mass, the more fragmentation occurs. In a coating in which the composition of the resulting film matters, it is important to preserve the structure of the organic precursor. This structure is somewhat lost as the molecule is fragmented more, and completely lost if it is fragmented into component atoms.

The energy/mass ratio depends on a few instrument parameters. The power that is coupled to the gas in the deposition chamber over the molar flow rate of the precursor gas gives (W)/(moles/s), or (J/s)/(moles/s), or J/mol. Converting moles of precursor into mass gives back the aforementioned figure of merit of J/kg. So, both applied power and precursor flow rate directly affect the percentage of precursor fragmentation, and thus the chemical composition of the resulting films.^{11,13}

Additionally, the location of the substrate within the plasma, or distance outside of the plasma, controls what species the substrate is exposed to, and thus the conformallity, deposition rate, and deposition composition.^{11,13} The substrate can be placed in the high power region within the electrodes, in the plasma glow

adjacent to the electrodes, or in the afterglow where reactive species concentration decays exponentially with distance. In the afterglow, the substrates can be placed upstream from the electrodes such that most molecules have not yet passed through the fragmentizing electrodes, or downstream so that more have reacted.

The choice of precursor gas/vapor plays a role in the deposition.¹¹ Longer chain molecules are more likely to retain structure, but more influential than chain length is the presence of rings in the precursor. The properties of an 8-crown-6 deposited PEO-like film are different than the properties of a tetraglyme-deposited films.⁸ However, the differences in precursor are often less important than optimizing instrumentation parameters; PEO-like films can be made from ethylene oxide triads as well as from triglyme, tetraglyme, and the crown glymes.^{8,14}

The choice of coupling mechanism of the power source to the precursor gas is also important.¹¹ The plasma can be inductively¹⁵ or capacitively¹¹ coupled (Figure 2.2). Inductively coupled plasmas run RF power through an external coil, which creates magnetic fields within the chamber. A current is created in the plasma to oppose the changing RF current in the coil. Both the magnetic field and the capacitive element of the coil (linearly from one end to the other) give linear directionality to the resulting plasma. Capacitive coupling can be achieved in two ways. The first is to place a capacitor within the chamber. The capacitor can be run at DC or any AC frequency, and results in a highly directional, sputtering plasma deposition. A target can be placed on the opposite electrode to the substrate, causing a film to form from material that is sputtered off of the opposing electrode. These instruments are not conducive to coating micro-architectures, and would instead create shadowed regions where the sputtered ions were intercepted

by a surface that is more directly exposed to the deposition. A second type of capacitive coupling mechanism uses an external ring capacitor and only functions at RF frequencies. This type of capacitive coupling clearly has inductive components, as a purely capacitive set up is not expected to be able to be externally coupled, and also would not require the RF frequencies required by inductive plasmas. Both of the electrodeless coupling schemes can be optimized to deposit conformal coatings over microarchitectures.

2.2 Power Source and Choice of RF Coupling Mechanism

We first set a standard frequency for the power delivered for plasma deposition, and performed all other optimization keeping the frequency constant. RF electrodeless coupling requires a frequency of at least 300 kHz to function. As the frequency increases further, plasma impedance decreases, discharge current increases, and the applied voltage required for a given wattage decreases. Higher frequencies are also more complicated to generate and transmit, but the advantages outweigh the disadvantages up to tens of megahertz. Industrial, scientific, and medical (ISM) radio bands are assigned to specific frequencies such that they are reserved and emissions will not interfere with safety, emergency, or military communications, and so these bands have relaxed emissions limitations and regulations. In the US, these bands are 13.56, 27.12, 40.68, and 915 MHz. 13.56 MHz is the most common frequency used for commercial generators, and is the one we chose to use.

Upon generating power at a frequency of 13.56 MHz, we optimized a mechanism to eliminate reflected power such that the maximum power was

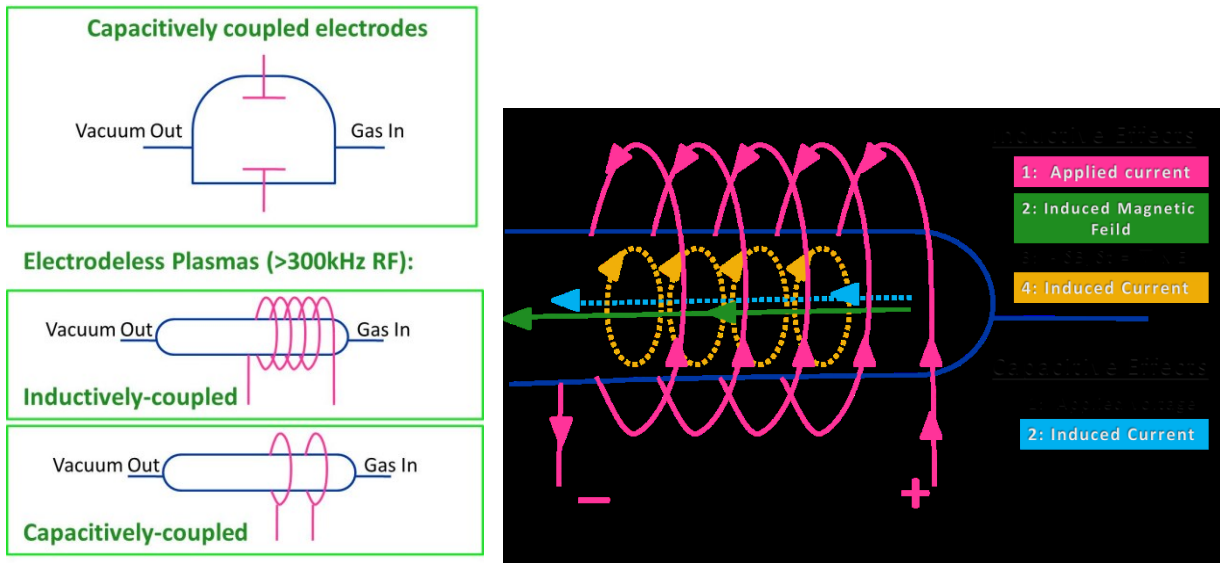


Figure 2.2 (left) diagrams of each of the 3 main mechanisms for coupling RF power to a plasma. Capacitively coupled plasmas have internal electrodes and create sputtering conditions. The electrodeless plasmas both have inductive components, but the external coil is referred to as an inductively coupled plasma, while an external set of rings is referred to as a capacitively coupled plasma. Both of these electrodeless plasmas can be optimized for conformal coatings. (right) the mechanism of coupling of an inductively coupling plasma. Inductively, both a magnetic field and a current are induced in the plasma. Capacitively, a linear current is also introduced, which aligns with the induced magnetic field.

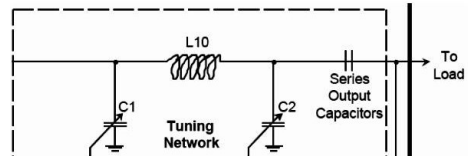
delivered to the electrode. With RF electronics, it is important to match the impedance of the generator to the impedance of all the transmission lines, and also to the impedance of the plasma system (both the electrode and the coupled plasma). The impedance is the vector sum of all of the opposition to current flow, whether electrical resistance or reactance (from inductive or capacitive effects). Matching the impedance ensures the most efficient power transfer and the highest signal to noise ratio. This can be seen very simply for a case in which the impedance is a pure resistor. A power source (P_S) with an internal resistance (R_S) in series can be put in series with a load resistance (R_L). The current that flows in the simple circuit, from $V = IR$, is $I=V/(R_S + R_L)$. The power delivered to the load is $P_L=I^2R_L$. Combining the two elementary definitions, we get $P_L=R_L(V/(R_S + R_L))^2$. Setting the power at the load to be the maximum power, $P_L=P_S$. In that case, $P_L=P_S=R_L(V/(R_S + R_L))^2 = R_S (V/(R_S + R_L))^2$. Canceling the large term present on each side, $R_L=R_S$. In addition to resistive elements, RF impedance also contains capacitive components, which oppose a change in voltage, and inductive components, which oppose a change in current. A full derivation for impedance matching that includes capacitive and inductive elements is present in work by Traficante in 1989.¹⁶

Impedance matching of transmission lines to power generators is straightforward. Power generators are assembled in order to conform to a standard source impedance of 50 or 75 Ω . Our source was 50 Ω . Transmission lines also conform to these same two impedances, such that we could use commercial 50 Ω lines to avoid an impedance mismatch between the source and the power cable.

However, we were required to match the impedance of the plasma to the 50

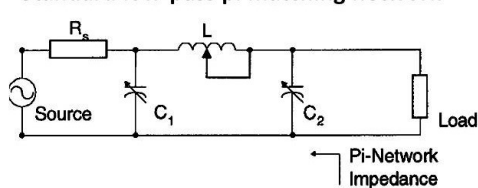


Circuit diagram for my matching network



MKS Instruments. *Operation Manual: MW-10D Automatic Matching Network.* (1999) Revision level C3, p2.

Standard low-pass pi matching network



M. Thompson; J. K. Fidler. *Proc. Int. Conf. HF Radio,*
Nottingham, U.K. (1997).



Figure 2.3. A commercial variant on a low-pass pi matching network was used to match the impedance of the plasma load to the impedance of the RF generator. This allowed for maximum power to be delivered to the load.

Ω impedance of the source and transmission line. The cable was connected to the plasma load through an impedance matching network, shown in Figure 2.3. The matching network sold by MKS was a variation on the standard low pass pi matching network, where the fins visible in Figure 2.3 belong to the 2 variable capacitors. By twisting a rod through the center of the fins, the distance between adjacent fins varies, and the capacitance changes. The top spiral is the inductor. The white bar connects the circuit to one end of the inductor, and the connection position determines the inductance value. By varying both the inductance and capacitance in each of the elements in the matching network, and optimizing the values for 0 W reflected power, the impedance of the plasma was matched.

A Helmholtz coil configuration was employed to solve safety concerns with inductively coupled electrodes. Inductive coupling converts a lot of power to heat, and requires water-cooling. We made the coil using copper tubing, providing an inner conduit for water-cooling. However, the water conducts electricity and becomes a safety hazard. A Helmholtz configuration was chosen because it requires RF power to be delivered to the center of the coil, and for both of the ends to be grounded. The result is that water enters and leaves the coil at ground potential, thereby eliminating the safety risk.

The matching network in Figure 2.3 in conjunction with the Helmholtz coil prototype shown in Figure 2.4 allowed for the plasma to be ignited, but problematically. High voltages (<80 W) were required to ignite the plasma, despite the reflected power being matched to 0 W. Powers as low as 5 W should be sufficient for plasma ignition via an optimized instrument. After ignition, the power was adjusted to as low as 20 W without trouble. High powered plasmas resulted in

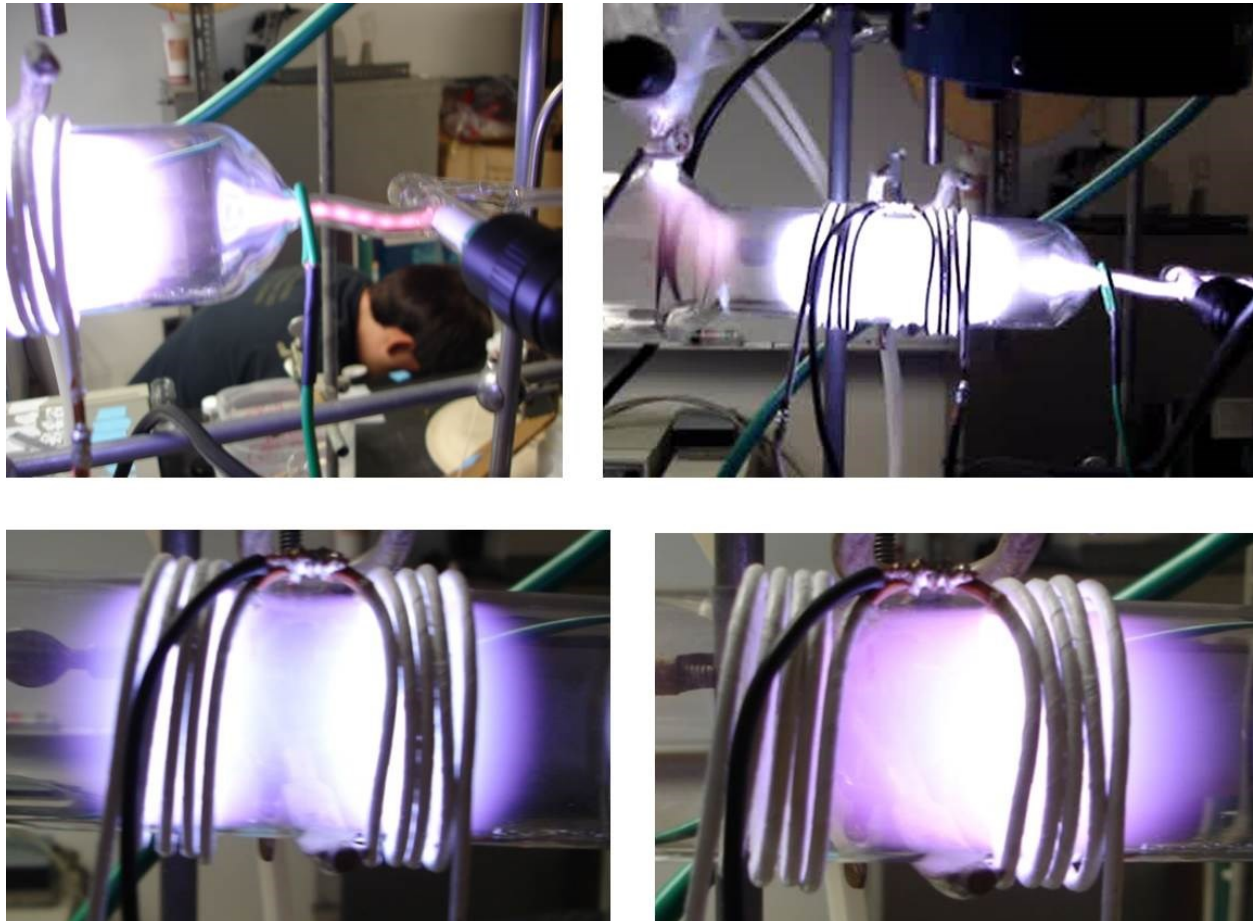


Figure 2.4 (top) High powered plasmas arc through the monomer inlet and other tube narrowings. (bottom) Lower powered plasmas are either uneven in the coil (shown), or flicker on and off.

arching up the precursor inlet, which would result in highly fragmented precursors (Figure 2.4 top). Lower powers resulted in uneven and unstable plasmas, which often flickered on and off, and sometimes extinguished. While many variations in coil architecture were explored (turn-turn separation, left-right coil separation, number of coils), only negligible changes in performance were noted.

In comparison, we found that a system built using a home-made simple circuit as a matching network resulted in much greater stability in the plasma discharge than the system described above using the commercial matching network. This home built network consisted only of a variable inductor in parallel with a single variable capacitor. Ignition occurred at 30-40 W, and arcing was noticeably reduced. This can be attributed to an enhancement in the signal to noise ratio by the simpler network. The variable inductor and capacitor in the simpler circuit are both hand operated, and no additional circuitry is present. In contrast, the initial MKS matching network was an automated matching network, and contained circuitry for receiving feedback from the power generator of the reflected power, motors for adjusting the 2 variable capacitors, and a network for adjusting the motors to minimize the observed reflected power. When the automated matching network was in operation nearby speaker wires acted like antennas, picking up feedback from the noisy network. In contrast, the homemade matching network did not broadcast a noisy feedback, and more of the power likely went into producing the signal.

The improvement we saw by simplifying the matching network to reduce noise was once again seen when comparing the digital power generator with enhanced features to that of a simpler analogue RF power generator. The

combination of the analogue power generator and the hand operated matching network allowed plasma ignition at 5 W. Arcing was eliminated, but instabilities such as uneven discharge between the electrodes, and flickering, remained.

A system using capacitive electrodeless external ring electrodes instead of the Helmholtz coil inductive electrodes improved the plasma discharge further. The simpler operation of the two rings in addition to the elimination of the water cooling (not required for capacitive coupling) likely aiding the stability of the system by reducing another potential source of noise.

2.3 Manifold for Pressure and Flow Control

In addition to the control and coupling of RF power, precise pressure control is required for deposition reproducibility. As mentioned above, cold plasmas require low pressures. Cold plasmas contain a smaller fraction of ionized species, allowing for more control over resulting film composition. Also, plasma discharges are not constant over space in the deposition chamber in terms of either delivered power or the distribution of active species concentrations, but instead the power and concentrations of reactive radicals resemble an onion structure. Increased pressure reduces the spacing of the onion layers around each electrode, leaving less active precursors in the space adjacent the electrodes.¹³ Thus, changing the pressure changes the plasma environment over a substrate that is a set distance from a plasma discharge.

We used a combination of flow control and measurement to control the pressure of our system during depositions. We used a direct drive vacuum pump to create low pressures, connected to the chamber through a Teflon regulating valve

to provide the flow control, and ultimate deposition chamber pressure. Pressure was measured using a Baratron capacitance etch monometer, shown in Figure 2.5, near the precursor inlet. Capacitance monometers function independently of the analyte gas, making them ideal for complicated mixed species systems such as plasmas. They give high precision over a wide pressure range, and do not show interference from RF electronics. The Baratron etch monometer is heated and contains baffles as a protection from plasma etching or deposition. Plasma deposition is a condensation process, and so having a cool monometer attached to a heated chamber would result in continued deposition and finally destruction of the monometer. A heated monometer is expected to have a larger lifetime.

Another important parameter that must be controlled is the precursor flow rate. The flow rate of the precursor directly impacts the degree of fragmentation of the precursor, due to the aforementioned figure of merit: $(\text{applied power}) / (\text{molar precursor flow rate})$. Thermal mass-flow meters allow for unparalleled control over flow rates of calibrated species. They control flow rates independent of pressure and temperature variations. However, they are not cost effective, as they have a limited working lifetime while metering a sticky glyme precursor. Floating ball rotometers are far more economical, and give reproducible flow rates so long as either the inlet or outlet pressure is controlled. They can be opened and cleaned if tetraglyme causes the floating ball to stick intermittently. However, in our system it was discovered that they became stuck within seconds of use, and so were not suitable to meter our precursor. Instead, a regulating valve was employed. At a constant precursor temperature, and a constant pressure, the precursor delivery was reproducible at a constant valve position, as judged by our deposition rates.

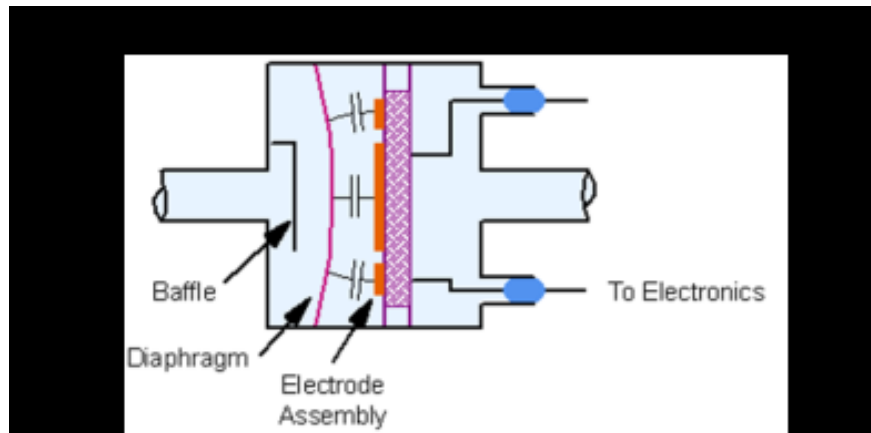


Figure 2.5. Schematic of a Baratron capacitive etch manometer, showing the mechanism of pressure sensing through capacitive connections to a mobile diaphragm, and the protective, heated, baffle (which is arranged to force a more complicated vapor pathway than depicted).

Argon carrier gas was employed in order to assist the tetraglyme precursor in achieving higher vapor pressures and to allow for additional control over the flow rate of the introduced precursor. However, the addition of bombarding inert gas molecules adds to the fragmentation of the precursor molecules, and is not ideal for control over resulting film structure.⁸ It was found that by increasing the heating of the precursor vial and gas manifold, no carrier gas was required for tetraglyme deposition.⁸

In addition to controlling the pressure and flow rate of the precursor, the manifold can be configured such that the plasma deposition occurs upstream or downstream of the plasma discharge (Figure 2.6). When the precursor gas passes through the discharge before encountering the substrate, the precursor was highly fragmented even at low powers, and the desired low fragmentation states could not be reached. Conversely, when the substrate is placed upstream of the discharge, in between the discharge and the monomer inlet, deposition only occurs via back-migrating species (i.e. species which turbulently go against the precursor flow). The resulting percentage of fragmented monomer that the substrate is exposed is much lower, allowing for us to gain improved control over the composition of the deposited film. In this upstream configuration, at low powers, almost none of the precursor that encounters the substrate was fragmented. Increasing the power or decreasing the flow rate increases the percentage of fragmented monomer, giving a wide window of potential film compositions.

Lastly, we found that the temperature of the deposition chamber was very important. Plasma deposition is a condensation process. As precursors react in the gas phase, they eventually reach a critical mass and condense. Once deposited,

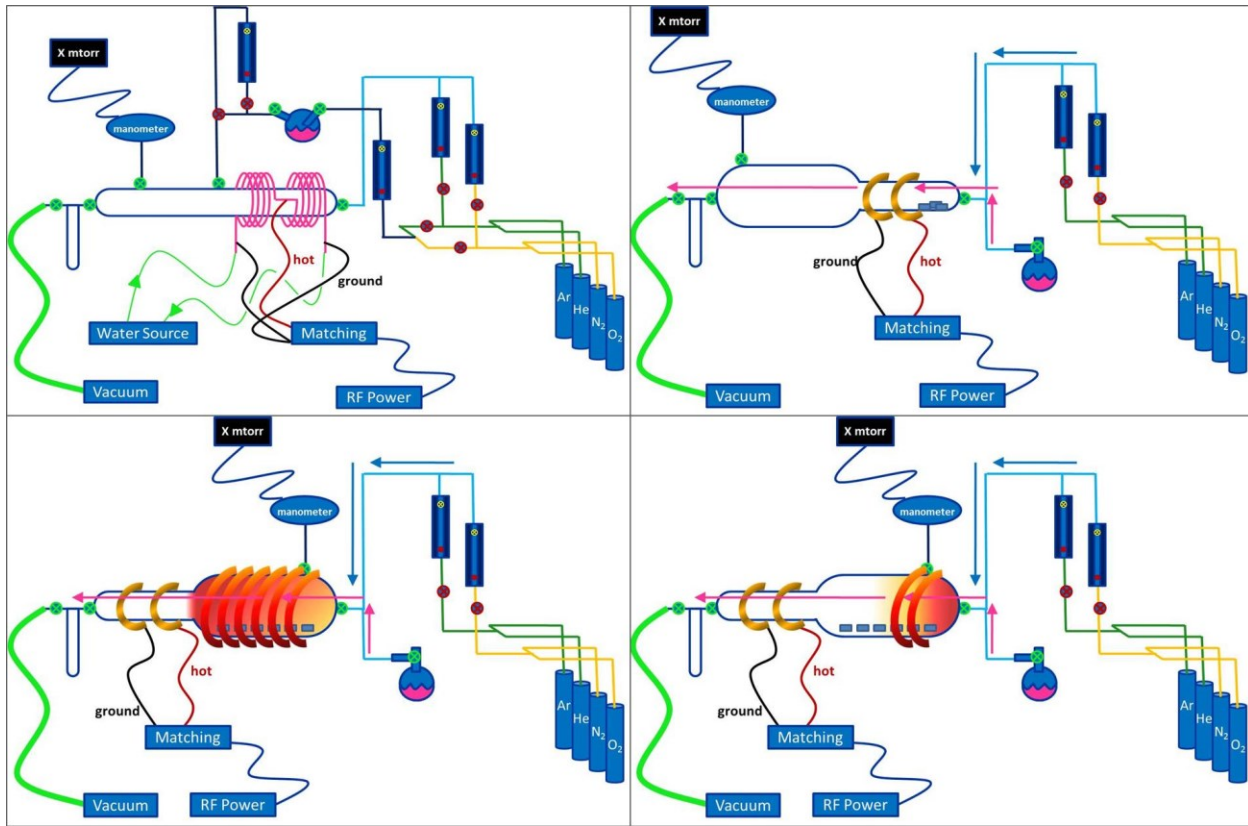


Figure 2.6. Four configurations of the gas manifold with RF power coupled through an external electrode to the vapors inside of the deposition chamber in order to create a plasma. (top left) inductive coupling with a downstream substrate region. (top right) electrodeless capacitive coupling with a downstream substrate region. (bottom left) electrodeless capacitive coupling with an upstream deposition region. The chamber is heated to allow for increased vapor transport distances. (bottom right) a specific deposition region just at the afterglow is not heated in order to promote plasma deposition.

the exposed surface of the coating continues to fragment and react in the afterglow region of the plasma. The growth mechanism at the surface competes with further condensation of reactive agglomerates from the gas phase. When the temperature was too cool, the condensation rate was too high, and even unreacted tetraglyme liquid condensed. This created a barrier to plasma polymerization. When the temperature was too warm, condensation was too slow, and (more limited) film growth occurred primarily through plasma fragmentation of the surface of the film. This led to a more cross-linked film, and less control over the film composition. We found that the condensation rate fell in between these two extremes when the chamber was heated by wrapping heating tape around the portion near the precursor inlet, but not around the location for the deposition (Figure 2.6). By subtly varying the temperature of the heating tape, it was found that the condensation rate was acceptable in the range of 70°C to 80°C. Small (5°C) changes in this narrow window resulted in noticeable changes to the structure of the polymer deposition. At 70°C, lower powers and higher precursor flow rates were required for a less fragmented deposition. At 80°C, higher powers and lower precursor flow rates were required to keep the results consistent.

2.4 Conclusions

A manifold has been constructed for metered delivery of various gasses and tetraglyme precursor into a deposition chamber. The system achieves pressure-control independent of flow-rates, allowing for better control over variation of plasma polymer density and structure. A reaction chamber has also been constructed to allow for a variety of sample positions and monomer-to-antenna

distances. This variable distance is important for the gentle polymerization of ethers to PEO-like polymers without excessive cross-linking. The pumping system and connections allow for pressures down to 2 mTorr for high batch-to-batch purity.

RF power is coupled to the plasma from a low-noise analogue power source, through impedance matched transmission lines, to a low-noise matching network which matches the impedance of the plasma to the RF source. The electrodes are a pair of electrodeless capacitively coupled copper foil rings, which eliminate the requirement of water cooling by inductive coupling systems, further reducing the noise in the system. Using this instrument, controlled deposition of PEO-like films has been achieved, and these films are studied in Chapter 3 for their use as solid state battery electrolyte coatings.

2.5 References

1. Dudley, N. J. Thin Film Micro-batteries. *Electrochem. Soc. Interface* **44–48** (2008).
2. Long, J. W., Dunn, B., Rolison, D. R. & White, H. S. Three-Dimensional Battery Architectures. *Chem. Rev.* **104**, 4463–4492 (2004).
3. Xu, F. *et al.* Properties of lithium phosphorus oxynitride (Lipon) for 3D solid-state lithium batteries. *J. Mater. Res.* **25**, 1507–1515 (2010).
4. Perre, E. *et al.* Electrodeposited Cu₂Sb as anode material for 3-dimensional Li-ion microbatteries. *J. Mater. Res.* **25**, 1485–1491 (2010).
5. Ratner, M. A. & Shriver, D. F. Ion transport in solvent-free polymers. *Chem. Rev.* **88**, 109–124 (1988).
6. Plylahan, N. *et al.* Highly conformal electrodeposition of copolymer

electrolytes into titania nanotubes for 3D Li-ion batteries. *Nanoscale Res. Lett.* **7**, 349–354 (2012).

7. Rhodes, C. P., Long, J. W., Doescher, M. S., Fontanella, J. J. & Rolison, D. R. Nanoscale Polymer Electrolytes: Ultrathin Electrodeposited Poly(Phenylene Oxide) with Solid-State Ionic Conductivity. *J. Phys. Chem. B* **108**, 13079–13087 (2004).
8. Johnston, E. E., Bryers, J. D. & Ratner, B. D. Plasma Deposition and Surface Characterization of Oligoglyme, Dioxane, and Crown Ether Nonfouling Films. *Langmuir* **21**, 870–881 (2005).
9. Menzies, D. J. *et al.* An X-ray and neutron reflectometry study of 'PEG-like' plasma polymer films. *J. R. Soc. Interface* **9**, 1008–1019 (2011).
10. Chang, J. P. & Chen, F. F. *Lecture Notes on Principles of Plasma Processing*. (Springer-Verlag, 2003).
11. Yasuda, H. Glow Discharge Polymerization. *J. Polym. Sci. Macromol. Rev.* **16**, 199–293 (1981).
12. López, G. P. *et al.* Glow discharge plasma deposition of tetraethylene glycol dimethyl ether for fouling-resistant biomaterial surfaces. *J. Biomed. Mater. Res.* **26**, 415–439 (1992).
13. Ledernez, L., Yasuda, H., Olcaytug, F., Gemetz, F. & Urban, G. Pressure Dependence of Plasma Polymerization of Methane at Constant W/FM. *Plasma Process. Polym.* **4**, S794–S796 (2007).
14. Inagaki, N. & Suzuki, K. Highly wettable films plasma-polymerized from ethylene oxide. *J. Polym. Sci. Part Polym. Chem.* **25**, 1633–1639 (1987).
15. Hopwood, J. Review of inductively coupled plasmas for plasma processing. *Plasma Sources Sci. Technol.* **1**, 109–116 (1992).

16. Traficante, D. D. Impedance: What it is and why it must be matched.
Concepts Magn. Reson. **1**, 73–92 (1989).

CHAPTER 3

Plasma Deposited PEO-like Electrolyte Coatings for Li-ion Batteries

3.1. Introduction

As on-chip energy demands grow and micron-scale electronic devices become ubiquitous, there is a growing need for integrated microscale batteries to allow for self-contained on-chip energy storage. Directly scaling down macroscale battery sandwich architectures (a flat anode and a flat cathode layer separated by an electrolyte-soaked separator layer) to microscale on-chip dimensions results in thin film batteries. Thin-film microbatteries have exceptional capacities and rate capabilities per unit volume.¹ The problem is that thin film batteries are primarily two-dimensional devices. Their volume per areal footprint is limited by a maximum device thickness of 10-15 μm .^{2,3} Thus, despite having better energy densities per volume than can be achieved by a macroscale battery, in the limited areal footprint of a microdevice the areal energy density of a thin film battery is scant.

The solution is to leave the flat layered architecture behind for a three-dimensional structure.^{2,3,4,5} By using a 3-D anode such as an array of posts or a gel network, the energy density can increase with the height of the structure, while transport distances (i.e. post or gel wall thicknesses) remain constant, preserving high power density. Six architectures have been proposed that meet this goal^{4,5} and we have chosen the anode post array as our target architecture. The post array can be paired with an appropriate cathode material that can be added in such a way that the entire space between the posts is filled in.

In order to keep the anode and cathode electrically isolated, however, we must first apply an appropriate electrolyte coating between the two materials. A major challenge has been to develop such a suitable electrolyte coating.^{4,2} It must be conformal so as to cover the anode architecture in a pinhole-free manner while leaving the space between posts free.

The standard electrolyte materials for thin film Li-ion batteries, lithium phosphate oxynitride (LiPON) and relatives, are deposited by directional processes such as sputtering that were historically assumed to be unable to coat the posts conformally.⁵ Studies are underway to develop conformal LiPON coatings in "shadowed" regions of the deposition chamber by blocking direct access of the sputtered ions to the 3D substrate. Successful shadowed depositions have been demonstrated for flat substrates, and 3D optimization is underway.⁶ Attempts are also ongoing to electropolymerize optimized conductive electrolyte coatings conformally onto posts, with the challenge being the conformallity.^{3,7} By electropolymerizing a resistive coating, the electrolyte self-limits and can be made to coat structures conformally.^{8,9,10} These coatings are less ionically conductive, but so thin that the overall conductance is still high enough, especially at lower scan rates.

We opted to design a new electrolyte material around the properties of an existing material with desirable ionic conductivity properties. Polyethylene oxide (PEO) is a standard dry solid electrolyte coating for macroscopic batteries. The polymer has a crown-ether-like backbone, and will coordinate ions in a polydentate crown-ether like fashion.¹¹ Above its glass transition temperature, ion conduction occurs, utilizing the chain mobility. The chains move in a swing-like fashion, such

that each crown-ether-like coordination site escorts the ion to the neighboring crown-ether-like site, whereupon ion-hopping to the second site can easily occur.¹¹

Many methods exist to depress or destroy the glass transition temperature of dry solid PEO electrolytes so as to extend the temperature range of ionic conductivity. All of these methods work through increasing disorder, which raises or eliminates the glass transition temperature, enhancing chain mobility which in turn enhances measured ionic conductivity. Disorder leading to eliminated glass transition temperatures are seen when adding in inorganic nanocrystals to make composites,^{12,13,14} choosing anions for the lithium salt that promote disorder,^{12,15,16,17} and adding ionic liquids as non-volatile plasticizers.^{18,19} We focus on a fourth method: the cross-linking of PEO chains to intentionally enforce disorder.^{11,14,20} All of the various cross-linking methods examined result in better depressed glass transition temperatures, which should lead to enhanced ionic conductivity.²¹

Conventionally, PEO is formed into a planar film through spin coating. Our goal is to develop a material that is modeled after PEO, but can be deposited conformally over higher surface area micro electrode architectures. Gas-phase depositions are ideal for such coatings, and so we chose to focus on plasma polymerization. Fortunately, in the field of bio-nonfouling, PEO-like plasma polymer surfaces have already been developed.^{22,23,24} Plasma polymers are gas-phase depositions formed from small oligomers of the intended polymer. Vapors of these oligomers are introduced into an ionized gas (plasma). Rather than keeping monomers whole and expanding a network or chain of the starting monomers, the plasma splits each oligomer into radical fragments. These fragments serve as the

monomers in that each fragment contains radical end-points which serve as a bridge to attach to other radical fragments. The re-combining of radical fragments results in a deposited film consisting of the cross-linked fragments of the original oligomer.²⁵

Utilizing these PEO-like plasma polymers for our electrolyte coatings is beneficial for two reasons. Firstly, gas-phase coatings are exceptionally conformal over structures like our microstructured architectures. Plasma polymers in particular have been shown to coat micro- and nano-structured architectures with a high degree of conformality, whether crosslinking monomers that have been absorbed into an architecture from the vapor phase,²⁶ or depositing a coating by introducing the precursor into a plasma chamber.²⁷ Cross-sectional views of high aspect ratio coated trenches show that the films are capable of depositing at a constant thickness at both the bottom and top of the trenches as well as on the sidewalls.²⁷ Secondly, the PEO-like plasma coating is inherently cross-linked, which, as discussed above, will introduce disorder that may be beneficial over a non-cross-linked PEO-like structure for room temperature ionic conductivity.²¹

This gives us a design strategy for our coatings, but introduces 2 primary challenges. Firstly, the bio-engineered plasma PEO-like coatings are PEO-like at their surfaces only. Bio-non-fouling only requires a functionalized surface layer, and using a highly cross-linked base layer (called an adhesion layer) provides for a robust film. This is a problem in that our electrolytes must conduct ions through the entirety of their structure, from one electrode at one surface to a second electrode at the other surface, and so must have a continuous PEO-like composition the entire way through. The reason that films are not deposited PEO-like through

their entirety is that to be useful, the films must also be robust, and the PEO-like portion is not typically robust. The product of plasma polymerization contains a distribution of chemical compositions.²⁵ The more PEO-like the plasma polymer, the less fractured the monomer will be in the film, but also the more completely unreacted monomer will be present as completely un-cross-linked deposit. This causes completely PEO-like plasma polymers to be very delicate, as regions may have few or no cross-links, and also less well-adhered to their substrate. One must thus find the compromise between PEO-like enough to conduct ions, but cross-linked enough for practicality, so that the films have the same blended composition the entire way through.

A second challenge presents itself in the point above that slightly more cross-linking than is necessary for pure PEO-like films must be introduced for robustness of the films. This is an issue because studies on cross-linking of traditionally polymerized PEO do not explore the upper limits of cross-link density on the ionic conductivity of PEO.²³ Chain motion is required for ion conduction, and so cross-linking to depress the glass transition temperature is beneficial. However, at some cross-link density, the chain movement should be retarded, lowering the conductivity. The cross-linking density in plasma polymers is much higher than that present in the studies on traditional PEO, and so this limit needs to be explored.

The goal of this work is thus to build upon the rich fields of plasma polymerization and PEO electrolytes in order to solve new problems that have arisen in the design of 3D microbatteries. The knowledge gained from the development of plasma polymerized films for bio-nonfouling applications is utilized,

and new depositions are developed to eliminate the adhesion layer. We optimize the films to be PEO-like throughout, and study their properties as electrolytes. We will show that they are electrically insulating as synthesized, but display ionic conductivity when a suitable lithium salt is introduced.

We further study the films by comparing three classes of depositions: those in which PEO was the target composition during the entire deposition, PEO-like films deposited over a 1-second high power adhesion layer blast, and films which are deposited over thin traditional bio-nonfouling adhesion layers of increasing thicknesses. All three classes of film use the same tetraglyme precursor for the entire deposition, but vary the degree of fragmentation and the rate of deposition by varying the deposition power. High deposition powers are used to create the highly fragmented and cross-linked adhesion blast and adhesion layer under-layers, and low deposition powers are utilized for the mostly un-fragmented PEO-like top layers.

3.2 Results and Discussion

3.2.1 Chemical and Structural Analysis

The PEO-like plasma films were prepared by capacitively coupling 30 W from a 3.56 MHz RF generator to a tetraglyme vapor in a deposition chamber, and depositing from the resulting tetraglyme plasma for 10 minutes onto clean ITO substrates, which were upstream from the electrodes. The upstream location ensures less fragmenting of the tetraglyme molecules, as the deposited tetraglyme never passes through the most intense region of the plasma between the electrodes. This is known specifically to aid in the retention of PEO-like character in

plasma films.²³

Before we investigate our films as conformal battery electrolyte coatings, we first explore their chemical relation to the PEO target material by XPS, and their conformallity by AFM. In the C (2p) peak on the X-ray photoelectron spectrum, shown in Figure 3.1, our films can show up to 4 distinct peaks. These can be fit as to their quantitative contribution to the overall spectrum in order to determine the chemical makeup of the films. Each peak represents a slight shift in the electron binding energies, in the carbon 2p shells, due to the 4 possible oxidation numbers of the carbon atoms. In the case of our films, containing only -C-O-, -C-C-, and -C-H— bonds, those oxidation states represent the number of oxygen atoms covalently bound to each carbon atom. The hydrocarbon film has the lowest binding energy oxidation state, representing the carbon atoms present in the film with no bonds to oxygen. The ether oxidation state represents those with 1 oxygen bond. The ketone oxidation state represents carbon atoms with 2 bonds to oxygen, and the ester oxidation state represents 3. There is no way to differentiate actual functional groups from this data. For example, the ketone oxidation state encompasses ketones as well as -O-C-O- and -O-C-OH groups, as each of those functionalities contain a carbon atom with 2 bonds to oxygen atoms.

We can use this data to determine the similarity of our plasma-deposited films to traditional, long chain PEO. PEO has a repeat unit of -C-O-C-C-O-C-, in which each carbon is part of an ether functional group, and bound to exactly one oxygen. Thus, in PEO, the C (2p) signal is a sole ether peak. Tetraglyme, which is a PEO oligomer, was used as the precursor in all of our plasma polymer depositions, and so every carbon in our precursor was also in the ether oxidation state. A

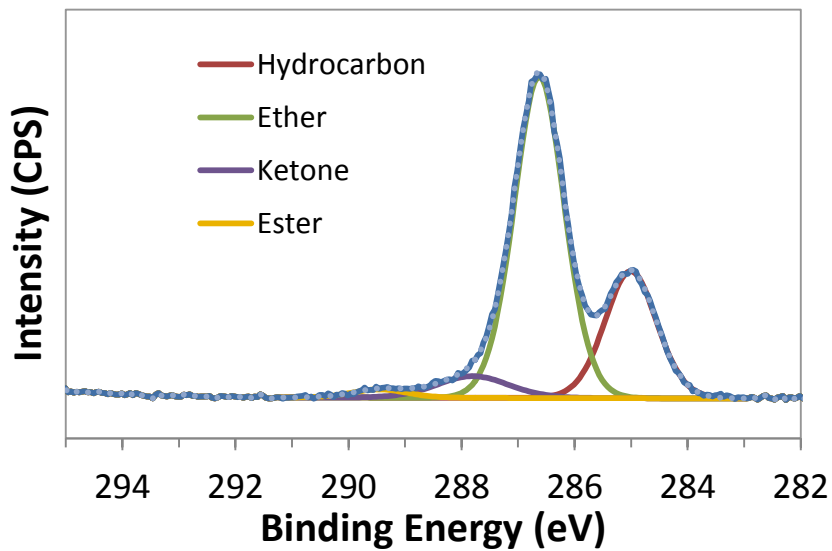


Figure 3.1. The XPS spectrum of a representative plasma polymerized PEO-like film. The C (2p) region is shown, and the solid blue trace is the measured spectrum. It can be seen that there are four distinct envelopes in our spectra. These envelopes are fit to peaks matching the oxidation states of aliphatic oxygen-containing hydrocarbons, and the resulting coalesced fit is shown in a dotted light blue line, which has a good overlay with the original spectrum.

heavily cross-linked tetraglyme plasma film loses oxygen as CO and CO₂, resulting in a large increase in the hydrocarbon peak at the expense of the ether peak in the resulting film. Additionally, small quantities of the carbon in the film form additional bonds to the increased number of intermediate oxygen radicals, resulting in small increases in both the ketone and ester peaks. We can use the ether peak percent-composition of the C (2p) region to quantify the amount of PEO-character remaining in our film. The percentage of PEO chains remaining is inversely proportional to the degree of cross-linking in the film. It should thus correlate well with the mobility of the chains in the film, and should also be proportional to the amount of the film that can coordinate and thus solvate lithium ions. Both of these factors (mobility and ion-coordination) make the PEO content of the film an essential factor in its performance as an electrolyte.

We were able to deposit PEO-like plasma films without the traditional adhesion layer. These films are attached to their underlying substrates, and do not soak off in water, acetonitrile, ethanol, or hexane (or any other solvent we have attempted). However, they are extremely delicate, and form scratches easily upon contact. In Figure 3.2, it can be seen that these films are highly PEO-like, with the ether oxidation state dominating. There is a small hydrocarbon shoulder, which is necessary for an adhering plasma-polymerized film. Plasma polymers contain a range of compositions, and if the range included no hydrocarbon atoms, then the ether oxidation state would be the most cross-linked species in the film, and the film would be heavily composed of un-reacted precursor.

We were also able to deposit PEO-like plasma films over an adhesion blast, consisting of an initial 1 second long 60W deposition, before applying the low power

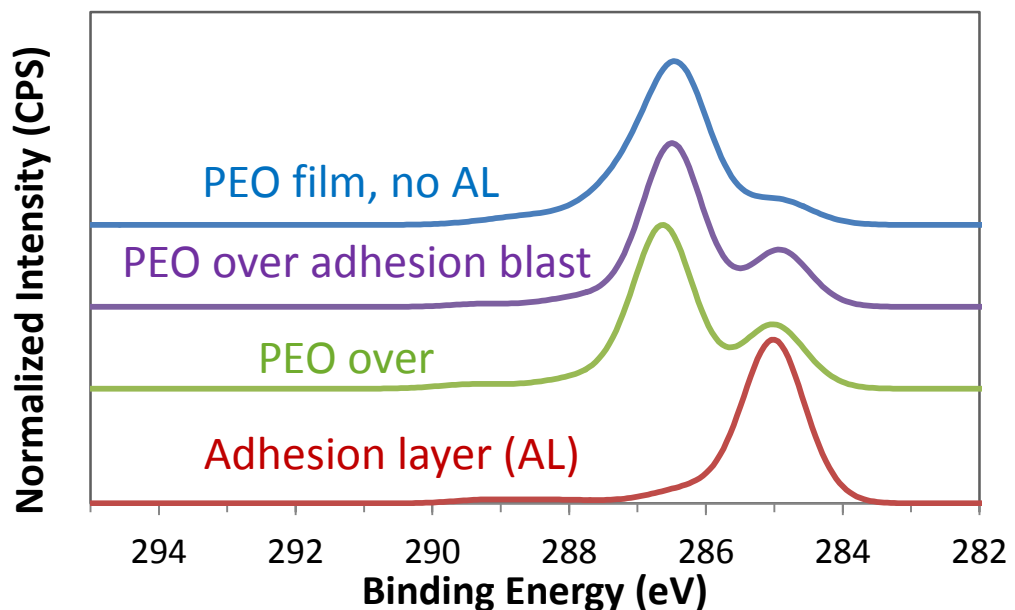


Figure 3.2. A comparison of the XPS spectra for representatives from each of the 3 classes of plasma deposition: a purely PEO-like deposition with no adhesion layer (AL), PEO deposited over a 1s adhesion blast, and PEO deposited over a 1, 2, or 3-minute AL. These 3 depositions are also compared to the XPS of a substrate subjected to the 1s adhesion blast, but removed from the deposition chamber without any further deposition.

PEO-targeted deposition. This high power is known to cause most oxygen to be lost from the tetraglyme precursor, resulting in a highly cross-linked hydrocarbon like film. Indeed, we stopped the deposition after the 1 second blast, and XPS analysis (Figure 3.2) shows that the carbon in the adhesion layer is almost entirely in the hydrocarbon oxidation state. These underlying hydrocarbon adhesion layers are useful in the field of bio-nonfouling in that they form a very resilient base, and are thought to result in much more conformal films. However, such an adhesion layer (which is traditionally many microns thick) would be expected to completely shut down the ion conduction through the film, disabling its function as an electrolyte. We have examined the function of a 1 second adhesion blast under our films, to find out if a very thin, tougher base layer enhanced the film properties.

As a comparison, we also made films with true adhesion layers, deposited for 1, 2, and 3 minutes before depositing the overlying PEO layer. These were not expected to be ion conductors through their entirety, but are useful to study the continuation of our series. In both the case of the adhesion blast and adhesion layer samples, XPS signals from some of the underlying hydrocarbon adhesion layer is visible through the thinner PEO-like layer (Figure 3.2).

All three types of film were also examined for their conformallity by AFM (Figure 3.3), and all were found to be relatively flat and conformal. The PEO-like films were extremely flat, with a maximum height of under 5 nm and a 0.54 nm RMS. The roughness data obtained by AFM is summarized in Table 3.1. It can be seen that the 1 s adhesion blast had a much higher roughness than the PEO-like film. However, the sample in which a PEO-like film was deposited over the 1 s adhesion blast shows a much flatter profile than the sample that only contains the

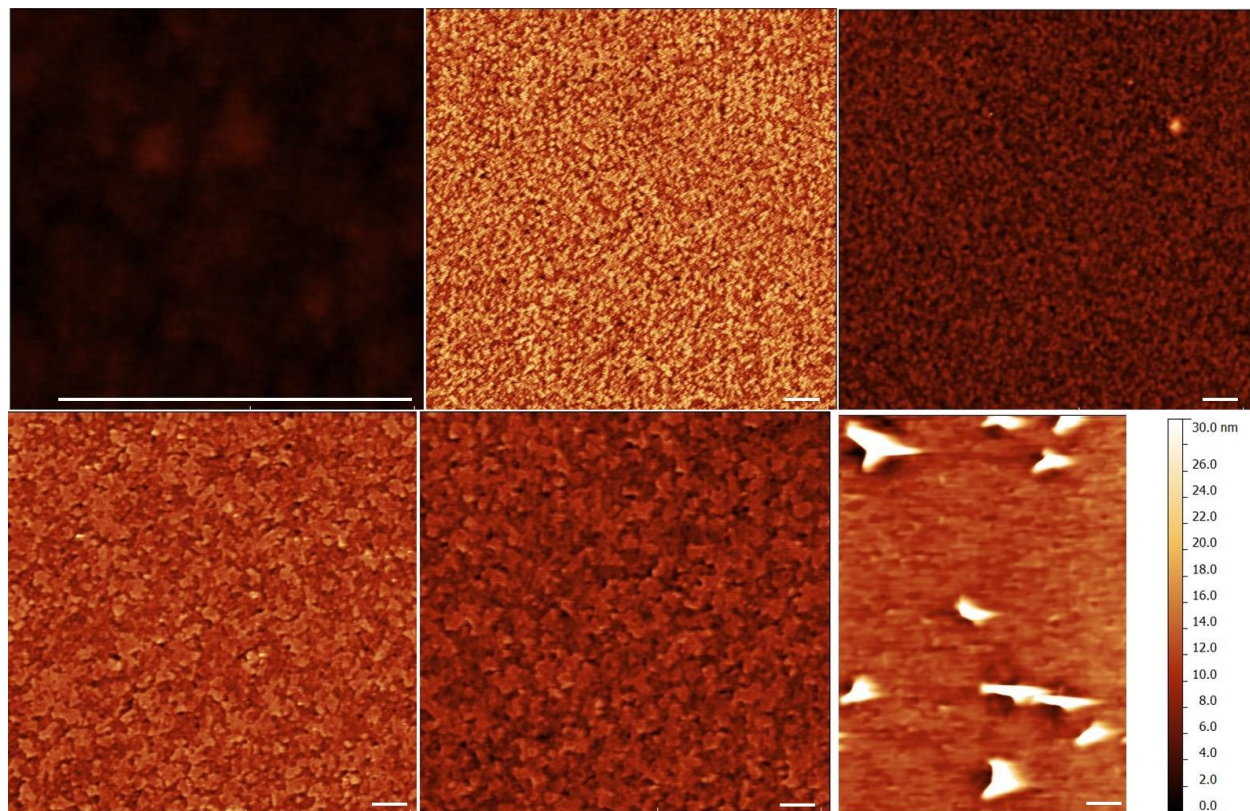


Figure 3.3. AFM height profiles for each class of plasma polymer film, deposited on ITO. All scale bars are 800 nm. (top left) a PEO-like film with no adhesion layer shows a height profile below 5 nm. (top middle) a 1 second adhesion blast layer with no PEO-like over-layer. (top right) a PEO-like film over the 1 second adhesion blast. (bottom left) a PEO-like layer over a 1 minute adhesion layer. (bottom center) a PEO-like film over a 2 minute adhesion layer. (bottom right) a PEO-like film over a 2 minute adhesion layer. Early (1 second and 1 minute) adhesion layer depositions are slightly rougher than the PEO-like over-layers and longer adhesion layer depositions. PEO-like films with no adhesion layers are noticeably flatter.

Table 3.1. Summary of height variation and roughness of plasma films by AFM.

Deposition Type	Tallest	Average	RMS Roughness
	Height (nm)	Height (nm)	(nm)
PEO-like	4.94	1.72	0.54
Adhesion Blast	28.16	13.88	3.69
PEO-like over adhesion blast ^a	10.61	5.23	1.43
PEO-like over 1 min adhesion layer	28.28	10.79	2.20
PEO-like over 2 min adhesion layer	17.25	8.08	1.96
PEO-like over 3 min adhesion layer ^b	18.6	12.0	1.5

^a Does not include particle in upper right corner

^b Does not include particles

adhesion blast. When a 1 minute adhesion layer was deposited, with a PEO-like film over top, the films displayed a higher roughness than was seen for the PEO-like film over the adhesion blast. This suggests that the adhesion layer continues to get rougher up until the 1 minute deposition point. The roughness is similar, but slightly less, for a PEO-like film deposited over a 2 minute adhesion layer.

While many microns-thick adhesion layers are known to enhance the consistency of plasma depositions, it seems in our case that a nano-metric adhesion layer starts out rough and non-conformal, and as thickness builds becomes more conformal and regular. At the one-minute point, the films have reached a maximum roughness (for all films with the same PEO-like over-layer). This suggests that the early precursor exposed to high power plasma in the empty deposition chamber began to polymerize quickly in the vapor phase, and cross-linked particles deposited in spaced out aggregates, rather than pairs and small groupings of cross-linked vapor-phase tetraglyme reacting further at the surface to form a film.²⁵ As the precursor continues to fill the chamber under constant power, over the course of a minute, the power/precursor ratio decreases, and the apparent power each precursor molecule is exposed to decreases. As the conditions equilibrate, the adhesion layer becomes more consistent as is expected from the common use of micron-thick adhesion layers to promote conformallity.²³

However, as the conditions equilibrate, the adhesion layer grows thicker. This layer is hydrocarbon-like, and not expected to conduct ions. One purpose of this study is thus to weigh the advantages and disadvantages of adhesion layers at the lower limits of their thickness: thick enough to provide an advantage in conformallity, and thin enough to minimally affect ion conductivity.

3.2.2 Electrochemical analysis

Once the films are characterized in regard to chemical composition and roughness, their function can be explored as thin film electrolytes. The effect of the adhesion blast and the adhesion layers on the electrolyte properties can also be explored. In order to quantify the lack of electrical conductivity and the high ionic conductivity that define an electrolyte, we utilize impedance spectroscopy. The PEO films are delicate, and so mercury drop electrodes were used to make electrical contact to the top of the films, which were deposited over ITO bottom electrodes. The mercury drop method has the added advantage of leaving the film uncovered by a permanent top electrode, such that the salt concentration in the film at each measurement spot can be varied between measurements.

As deposited, the films are purely organic materials, with no ionic or electro-mobile species. The films are also electron insulators. To confirm the insulating properties of the as-synthesized films, they were heated in vacuo to remove any water or solvent contaminants, and impedance spectroscopy was performed under argon atmosphere. The results are shown (Figure 3.4) in a Bode plot, which indicates the frequency dependence of the impedance. The blue trace is the as-deposited polymer film, and the linear frequency dependence of the impedance is clear. The film is sandwiched between an ITO electrode and the mercury top contact, and it would be expected that an insulator between two electrodes would function as a capacitor. This is exactly what is seen for the as-synthesized films, in that linear impedance as a function of frequency is characteristic of a capacitor. As a further confirmation of electrical insulation, the phase angle between the voltage and the current can be examined as a function of frequency (Figure 3.4). A

capacitor has a -90° phase angle between the voltage and current at all frequencies, and it can be seen that our as-deposited films are additionally confirmed to be an insulator by the fact that they hold to a -90° phase angle when sandwiched between 2 electrodes to form a capacitor.

Having achieved the desired insulating properties of our electrolyte, a next goal is to optimize our films to conduct ions. In order to demonstrate ionic conductivity, a lithium salt must be delivered into the film. Impedance analysis can then determine the conductivity of the coordinated ions. Previous groups used exotic methods to intercalate lithium salt into plasma films^{28,29}. However, the deposited films readily incorporated a variety of lithium salts from solution. Soaking the films in salt solutions proved problematic, however, due to the problem of how to dry the films afterwards. Films removed from the soaking solutions and allowed to dry had excess salt solution residue on their surfaces, which dried very unevenly leading to salt deposits. Using a high airflow to remove the solvent residue from the surface also results in salt deposits where the solvent was dried too quickly. We solved these problems by using spin coating to apply salt solutions such that the solvent dried evenly. The salt concentration used for spin coating was varied. We found that over a threshold concentration of 10 mM (in acetonitrile) the films saturated, and salt crystals were deposited on the surface and throughout the films. However, below this threshold concentration, salt was delivered into the film such that no salt crystals were detected on the film surface. At examined applied salt concentrations of 0.01 through 1 mM, all of the salt remaining on the substrate after spin coating was incorporated into the films. Lithium bis(triflate)imide was chosen as the primary salt for our conductivity study

for its high transference number and high conductivities in traditional polymer electrolytes.

A few of the 1 mM Li-intercalated films were analyzed by ICP elemental analysis to correlate applied salt concentrations to a resulting Li : (-C-O-C—) molar ratio in the films. This ratio is used by traditional long chain PEO electrolytes to characterize the salt dependence of their ionic conductivities. Even with identical 1800 RPM spin coating conditions, the 1 mM solution inserted somewhat different lithium densities into each of the different classes of plasma polymer. In pure PEO-like films with no adhesion layer, 3 films were examined, and the Li per polymer repeat unit ratio ranged from 0.03 to 0.07. In the films with an adhesion blast, 4 films were examined in duplicate, and ranged from 0.002-0.006 Li per repeat unit. The films that are likely to have more cross-linking at the base, due to the adhesion blast, take in less salt. The cross-linking may inhibit salt intercalation.

To further understand the connection between salt concentration and resulting film lithiation, two of the 0.5 mM adhesion blast films were examined by ICP, and found to have roughly half of the lithium content of the same films at 1 mM applied salt, suggesting that there is a linear correlation between applied salt and delivered salt, but the delivery depends on the nature of the film. Extrapolating this trend, the 1 mM adhesion blast films are expected to have about the same lithium content as the 0.1 mM PEO-like films with no adhesion blast. The adhesion blast films intercalate fewer lithium ions, probably due to the higher cross-linking density, as stated above. The ionic conductivity is relatively independent of salt concentrations, in the concentrations analyzed, and so the lower salt concentrations do not seem to affect the adhesion blast films adversely.

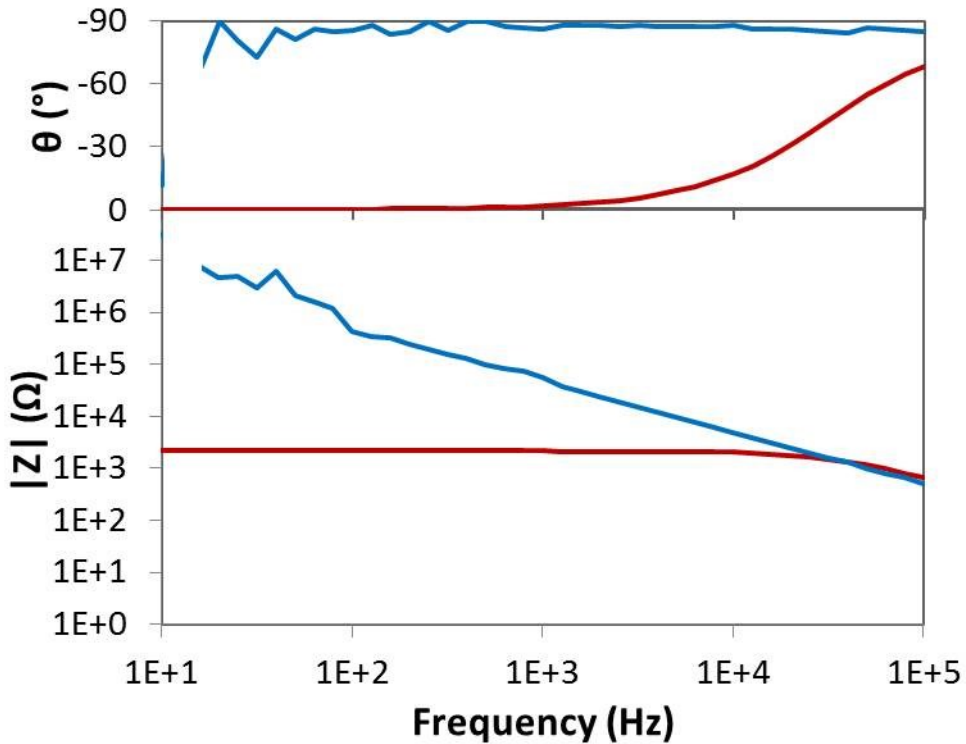


Figure 3.4. Representative Bode plots for a film without an adhesion layer. The data shown belongs to a film with an adhesion blast, but the PEO-like films with no adhesion layers show the same characteristic Bode and Nyquist plots. The red trace is for the film after lithiation, and the blue trace is for the un-lithiated control. (top) the phase angle between current and voltage as a function of frequency. -90° is characteristic of a capacitor, and 0° is characteristic of a conductor. (bottom) the overall impedance of the film—including resistive and reactive components—as a function of frequency. A linear trace is characteristic of a capacitor, and a constant value is characteristic of a conductor.

In traditional long-chain PEO dry electrolytes, optimal ionic conductivity is usually seen in a window of 0.1-1 lithium ions per PEO repeat unit. Our pure PEO and adhesion blast films cannot intercalate that much lithium; the salt crystalizes and ionic conductivities disappear. It would be interesting to be able to study the films at the higher lithium salt concentrations used in linear PEO films, to see if those salt concentrations lead to an increase in ionic conductivity.

In almost every instance of successful salt delivery (i.e. using spin coating at salt concentrations below the crystallization concentration), we saw clear evidence of ionic conductivity. Looking at the same Bode plot in Figure 3.4, the red trace is the same film as the blue control, after spin coat-intercalating with a 0.5 mM lithium bis(triflate)imide solution in acetonitrile. After the film has been lithiated, the impedance spectrum shows a shape characteristic of ionic conductivity. At high frequencies the red trace follows the path of the insulator. Ions cannot conduct above a threshold frequency because the oscillations of the field are faster than the response of the ions to the field. As the oscillations slow, the ions can change directions with the changing field, and conductivity turns on. Below these frequencies, the Bode trace resembles electron conduction, and has constant impedance with no further frequency dependence. This combination of insulation at high frequency and conductor at lower frequency is the characteristic impedance of ionic conductivity. In all our samples, we have ruled out electronic conductivity by measuring a non-lithiated control, as well as observing the lack of conduction in the high frequency region for the lithiated samples.

Just as before, after lithiation the ionic conductivity can be further confirmed by examining the phase angle of the impedance. A conducting film has a phase

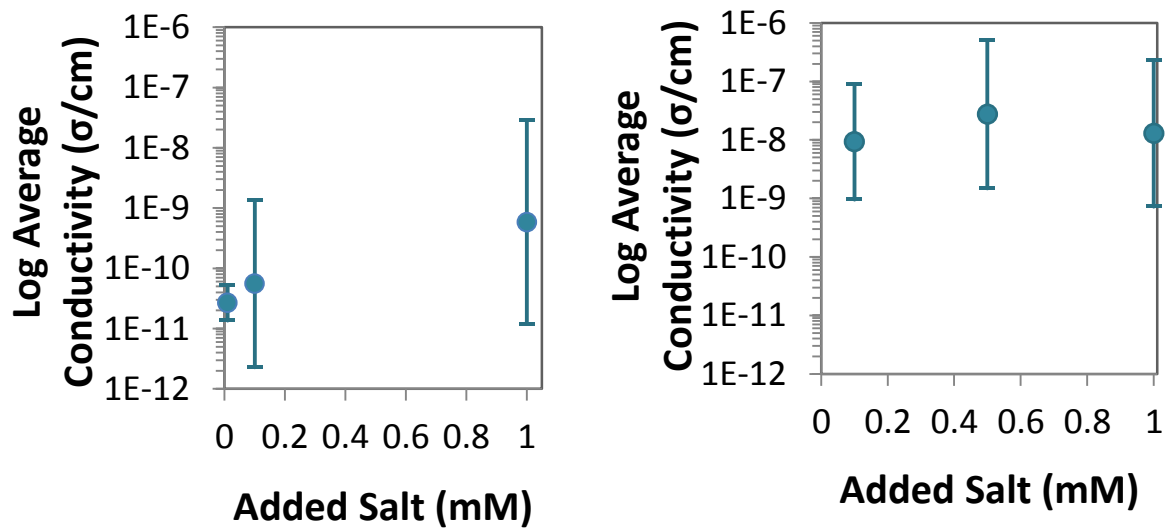


Figure 3.5. The geometric average of salt concentrations for (left) PEO-like films with no adhesion layer, and (right) PEO-like films deposited over a 1s adhesion blast, as a function of the applied salt concentration. Geometric standard deviations are reported for each average.

angle of 0° , and it can be seen that at 10^4 Hz, when the lithium shows a constant impedance magnitude, the phase angle of the impedance goes to 0° , further confirming the ionic conductivity of the films.

Using the values of impedance from the Bode plots, the various plasma PEO films can be compared as electrolytes. Films with crystallized salt showed no ionic conductivity, but at applied values of 1 mM salt and below, ionic conductivity was observed for nearly all films, at all of the examined salt concentrations.

For PEO films with no adhesion layer, in Figure 3.5, films show a slight salt dependence, with decreasing ionic conductivities at lower salt concentrations. However, the measurements display such a high standard deviation at 1 and 0.1 mM that a trend is difficult to confirm. It seems that the films are fairly consistent in ionic conductivities over 2 orders of magnitude in intercalated salt concentrations. Although the error becomes small at lower salt concentrations, the conductivities at 0.01 mM are generally lower than at higher salt concentrations, and so the decreased error range is not an advantage.

When a 1 s adhesion blast is deposited ahead of the PEO layer, improved conductivities are seen. In addition, the error range is smaller than the error seen at 1 mM (best conductivities) for the purely PEO-like films. In these films, negligible salt dependence was observed. The impedance values measured are for ions conducting through the entire film, including the base layer that is the adhesion blast. It can be seen that the thin adhesion blast does not impede the ionic conductivity. Instead, it adds consistency to the impedance results. This suggests that although the XPS data indicates the pure adhesion blast is highly hydrocarbon-based, it is too thin or does not have complete enough coverage to

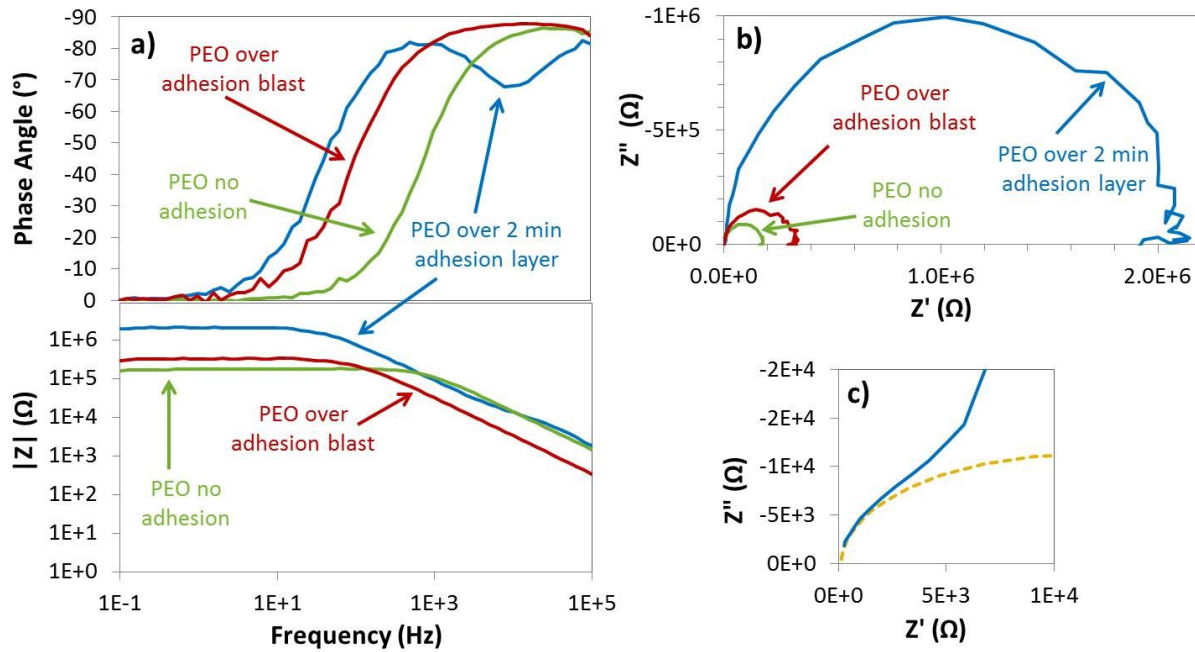


Figure 3.6. Bode and Nyquist plots of the impedance spectra for representatives of each class of film. a) In the upper Bode plot, the phase angle between the current and the voltage goes to -90° for a capacitor and 0° for a conductor. Two separate frequency-dependent conductivity regimes are evident for films with 2 min adhesion deposition. In the lower Bode plot, the impedance y-axis value becomes constant for a conductor. For the 2 min adhesion deposition film, a small inflection is seen near $1E+4$ Hz, representing the same, lower impedance, conductivity regime clearly represented in the phase angle data. b) Nyquist plots calculated from the same data used to create the Bode plots in Figure 3.6a. Each arc represents one conduction regime in the material measured. c) The low impedance regime for the Nyquist plot in Figure 3.6b, showing the beginning of a low impedance arc for the adhesion layer film (corresponding to the inflection in each Bode plot). The dotted line is the simulated fit values for the equivalent circuit, which gives the resistance at the small arc's extrapolated x-intercept.

affect ionic conductivity. The PEO plasma polymer could infiltrate into the blast layer, if it's not dense, or polymerizes directly on the ITO surface, if the adhesion blast is only present at anchor points.

The films that have a defined adhesion layer show 2 steps in their Bode plots, representing 2 separate frequency-dependent conductivity regimes in the material. Likely, the higher impedance regime represents the impedance for the adhesion layer, and the lower regime represents the overlying PEO-like layer. In Figure 3.6a, the inflection between the 2 steps is easily evident in the phase angle between the current and voltage, which starts at -90°, as the insulating component of a capacitor, and begins to approach 0°, showing the onset of ionic conductivity. However, the phase angle quickly re-approaches -90° again, and then approaches 0° again in a second step. The presence of a second step indicates a second region with an independent, higher, impedance value. The first step can be seen as well in the lower Bode plot, which shows a small inflection near 1e+4 Hz, where a constant impedance begins to appear, before a second insulating regime dominates and the upward slope reappears.

To analyze the adhesion layer and PEO layer impedance regions separately for these films, an equivalent circuit model can be fit to the arcs of a Nyquist plot. It should be noted that the high adhesion layer impedance would dominate the overall behavior of the films, and so although we can analyze the PEO-like layer to better understand the effects of an adhesion layer on the PEO-like layer deposition, the films are not suitable for electrolytes (as was expected). In Figure 3.6b we compare characteristic Nyquist plots for the three types of films, which are calculated from the same data as was used for the Bode plots in Figure 3.6a. Here,

the constant impedance intercepts in the Bode plots are represented as an intercept with the x-axis. It can be seen that the adhesion layer films have a much larger intercept than the other two film types, representing the higher impedance from the adhesion layer. One can see on the right in Figure 3.6c that this spectrum also contains a smaller arc, which can be fit to an intercept, or impedance, of its own. This represents the PEO layer of the film. The smaller arc was not seen for either of the other two types of films.

We fit the data using a resistor to represent the combined instrument and connectivity resistivities, in series with two identical circuits: one for each of the ionic conductivity arcs. These circuits each consisted of a resistor in parallel with a capacitor. They also included a transmissive finite Warburg element in series with the resistor, which incorporates roughness, or in our case gradient chemical composition, of the PEO electrolyte, which results in depressed semi-circles in the Nyquist plot, and intercept angles of less than 90°C. For each of these circuits, the resistor represents the ionic resistance of the film, or x-intercept of each arc, with the capacitor and constant phase element giving the reactance, or y-axis, component of the data. The instrument and connection resistor values for all samples fit to $\sim 10^2 \Omega$, which is slightly outside of the range of our instrument to measure with any measure of accuracy, but produces a slight perturbation in the very first point or two of our data. Although the values cannot be known with certainty, they low enough that they should not interfere with the measurements of the properties of our films.

The geometric averages of the fit values for both the adhesion layer arc and the PEO-like arc are shown in Figure 3.7. The impedance of the films was

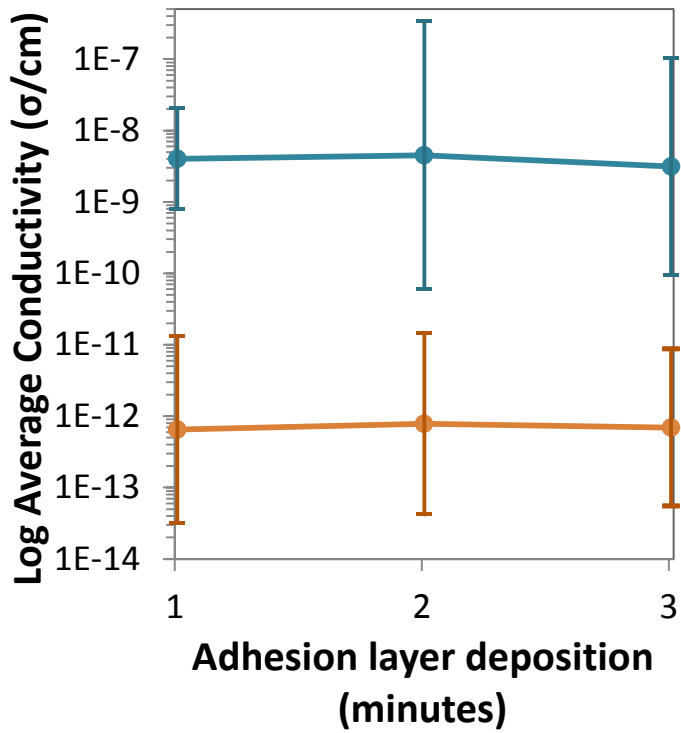


Figure 3.7. Geometric average values of impedance for both the adhesion layer and the PEO-like layer deposited over the adhesion layer. The adhesion layer has much higher impedance values than seen for the PEO-like layers in each of the 3 film classes, which was expected due to higher cross-linking, and lack of much of the functionality required to coordinate lithium ions. The PEO-like layer shows conductivities similar to the other PEO-like plasma polymers studied, but does not improve upon them.

measured under both 1 mM and 10 mM salt intercalations, and the two concentrations produced similar values for each of the adhesion layer thicknesses. The films over adhesion layers did not show salt saturation until 40 mM salt solutions were used for incorporation, unlike the PEO with no adhesion layer, in which crystalline Li deposits were visible when solutions of 10 mM salt were applied. This indicates that these films may be able to intercalate lithium in the 0.1-1 lithium to PEO segment range that produces good ionic conductivities in long chain PEO electrolytes. However, they do not display overall advantages or increased ionic conduction in the PEO-like layer despite the higher Li concentrations. Not surprisingly, the PEO-like impedance values and also the adhesion layer impedance values do not change with increased deposition time for the adhesion layer, as their compositions were not expected to change with varied deposition times.

The conductivities of the PEO-like layer, and their standard deviations, are comparable to the films without adhesion layers. The averages are slightly lower than the values seen for the other two types, but they are comparable within a standard deviation. However, the films are shown to be dominated by the much higher impedance of the adhesion layers, which renders them useless as electrolytes.

To briefly summarize our planar depositions, we have shown that a short 1 s adhesion blast incorporates into the PEO-like film, adding stability and consistency, both by AFM and impedance spectroscopy. However, a fully covering, thicker, adhesion layer harms both the conformallity of the films and the ionic conductivities, even at low thicknesses. We have shown that PEO-like plasma films deposited in a number of ways function as electrolytes, being both electrically

insulating and ionically conducting. We have shown that lithium salt incorporation into these films is straightforward, and that there is a small salt dependence below salt saturation and crystallization.

Having characterized our films in 2-dimensions, we examined the conformallity of our coatings over a 3D Li-ion battery anode. The chosen anode is a post array, seen in Figure 3.8, formed from a colloidal graphite solution that was pressed into a silicon mold. The graphitic posts are held together using a PvDF binder, and electrically wired using carbon black, both of which were incorporated into the material in the solution phase. Our plasma deposited coatings should be ideal to coat such a post array because of the inhomogeneous nature of the surface of the colloidally formed posts. The surface is a mixture of graphitic colloids, and exposed carbon black and polymeric binder. Reactive coating processes such as ALD may have varying precursor reactivities for each of the surface types, and may show uneven growth initiation. However, plasma polymerization occurs through a condensation mechanism, and can coat all exposed surfaces without regard to chemical functionality.

In Figure 3.8, it can be seen that the resulting posts are porous, with a surface structure originating from their colloidal precursor. After the coating, the non-smooth microstructure of the posts is still visible beneath a smoothing layer of polymeric coating. On the tops of the posts, neighboring colloidal nodules have been coalesced into a larger lump, with surface roughness still visible beneath. On the sides of the posts the porosity has been filled in, leaving only a slightly rough surface. The posts appear to be coated conformally, with the coating outlining the larger post-architecture of the underlying array, covering the smaller colloidal

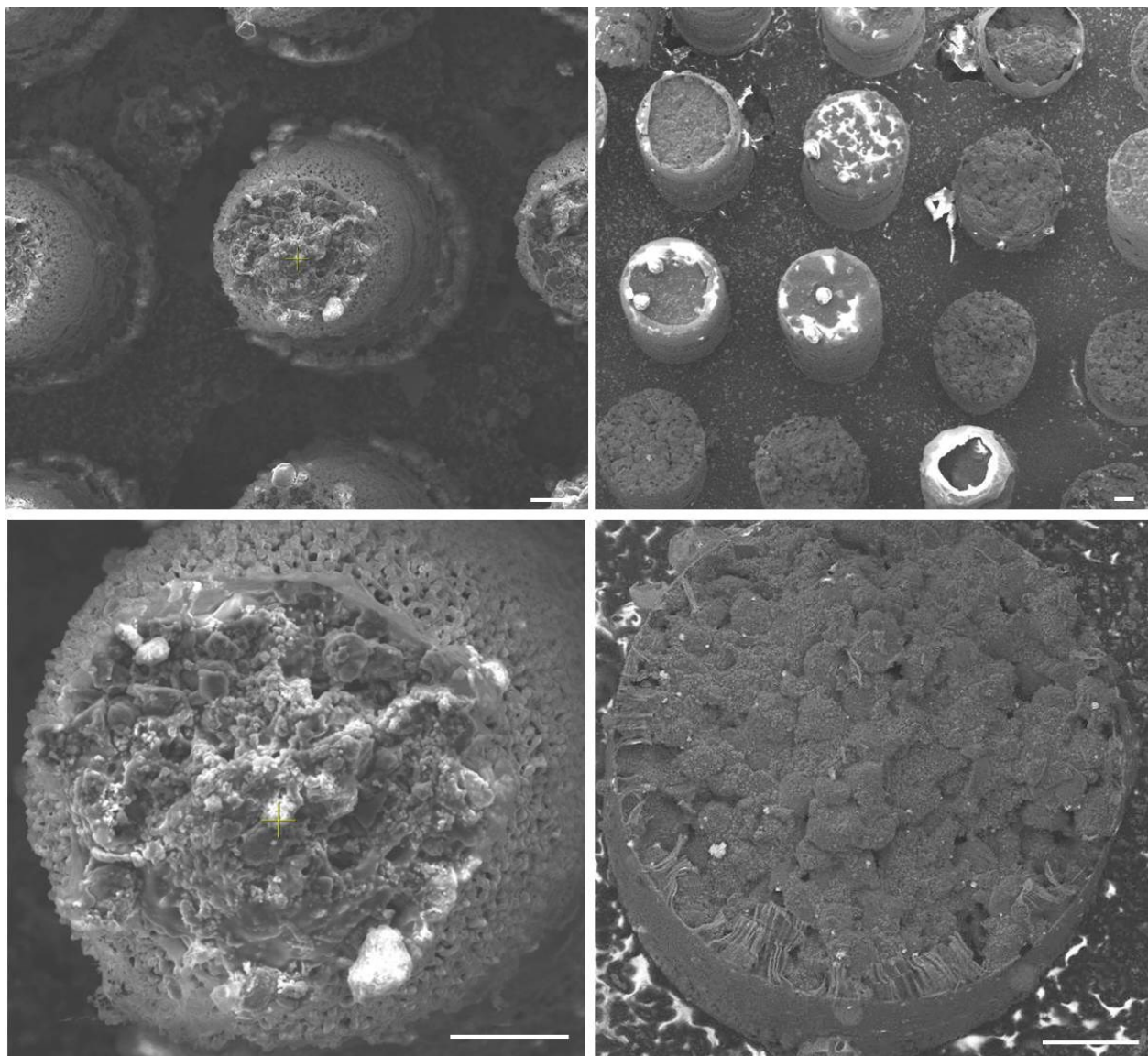


Figure 3.8. Environmental SEM images of a 3D microbattery post array. All scale bars are 20 μm . The left column shows the uncoated posts arrays at various magnification. The colloidal microstructure is clearly visible. The right column shows a post array after a plasma polymer PEO-like coating was deposited. The colloidal microstructure is filled in but the underlying construction is still visible.

structure without any visible bare areas, and leaving the space between posts clear. Whether or not the coating is pinhole-free remains to be tested. One common method of testing electrolytes for pinholes is to measure the accessibility of a redox active solution species to the underlying coated electrode. However, polymeric films swell in solution, creating space for solution species to pass through, and so the construction of a full battery may be the best test of the film as a pin-hole-free electron barrier.

3.3 Conclusions

Depositing plasma polymer PEO-like coatings from the vapor phase, we were able to intercalate lithium salt and create conformal electrolyte coatings. Our coatings were electrically resistive, and displayed ionic conductivities of up to 10^6 S/cm. We were able to show for the first time that plasma polymerized PEO-like coatings could be deposited without an adhesion layer and still form stable and strongly adhered films. However, we found that the ionic conductivity was slightly improved, and had lower standard deviation, if a 1 s adhesion blast was applied prior to PEO-like deposition. We showed, as expected, that a full adhesion layer is not conducive to ionic conductivity, and, furthermore, does not give overall advantages in film flatness. Finally, we showed that our electrolyte coatings can form a coating over a high aspect ratio post array, which follows the contours of each post well, without filling any of the space between the posts. We have demonstrated the development of a new electrolyte for 3D microbatteries, which can be further optimized after testing in a full 3D cell with a suitable colloidal cathode.

3.4 Experimental

3.4.1 Instrumentation and Deposition

The development of the instrument for plasma deposition is described fully in Chapter 2. Briefly, the final design consisted of a glass tube reaction chamber for deposition, which had a regulated pressure (via a valve to a downstream Alcatel vacuum pump), and inlets for heated monomer and metered argon to enter. The chamber was heated near the monomer inlets, and room temperature at the substrate site, to aid in film deposition. Capacitively coupled, external copper electrodes were located 3.3-4.5" downstream from the substrates, so that the deposition could occur with minimal fragmentation of monomers, which did not pass through the most intense region of the plasma before depositing. Likewise, to minimize monomer fragmentation, the vapor inside of the chamber consisted purely of tetraglyme, with no carrier gas.

The chamber was cleaned thoroughly with an acetone soaked cloth, and then rinsed with acetone and ethanol prior to each deposition. It was evacuated to 50 mTorr under a 14 sccm argon flow, and plasma cleaned at 70W for two 3 minute segments, separated by a 10 minute interlude of flowing argon with no RF power, for the chamber to cool.

All films were deposited onto flat ITO, unless otherwise noted. The ITO was thoroughly cleaned prior to deposition with Alconox, followed by water, and finally ethanol, before being dried via a high pressure nitrogen stream.

Tetraglyme (Aldrich) was used as received. 4 mL were placed in a vacuum flask, and placed on the gas manifold for the deposition chamber. Three cycles of

freeze-pump-thaw were completed to degas the precursor, and the precursor flask and all of the manifold lines were heated to 120°C for the deposition. The deposition chamber near the precursor inlet was heated to 80°C to aid precursor flow across the chamber. PEO-like films with no adhesion layer were deposited at 30 W for 10 minutes, at a pressure of 50 mTorr. The precursor was allowed to enter the chamber 1 minute before the plasma was ignited, and flowed for an additional 2 minutes after it was extinguished.

PEO-like films with a 1 s adhesion blast, or the 1, 2, or 3 minute adhesion layer, were deposited in a similar instrument in the Ratner Lab Group at the University of Washington in Seattle. The parameters for a PEO-like film were separately optimized for their instrument, and found to be 10 W at a pressure of 350 mTorr, and all PEO-like layers were deposited for 15 minutes. The underlying adhesion blast and adhesion layers were deposited at the same 350 mtorr, but at a much higher 60 W power.

3.4.2 Preparation for Analysis

All films were rinsed with 18 MΩ water to remove surface unreacted precursor, and immersed in fresh 18 MΩ water overnight to make sure that the film was cleared of any internal unreacted or non-adhered components. The films were dried at 65°C in a vacuum oven for at least 5 hours, backfilled with argon, and immediately analyzed by XPS. The time in the vacuum oven was the only time post-deposition that the films were not immersed in water, in order to prevent irreversible carbon contamination from airborne particulates.

Impedance controls (to ensure electrical resistance) were performed on every sample, after XPS. The films were freshly dried at 65°C in a vacuum oven

overnight, before being backfilled again with argon, and immediately pumped into an argon-filled glove box, while still warm. Adsorption of moisture from the air would cause proton conduction to appear in the impedance spectrum. Conductivity was not detected during our controls for any member of the deposition series included in this study, and so our drying methods were considered effective.

After the controls were acquired, the polymers were lithiated by spin coating acetonitrile solutions of lithium (bis)triflate imide (in the desired concentration) onto the surface of the film. The film was ramped for 6 s to 1800 RPM, held at that speed for 45 s, and then ramped back to stillness for 6 s. The films were solvent annealed as follows in order to ensure micro- distribution of the salt. They were placed in a sealed container for 5 hours with an open vial of acetonitrile, and held at 60°C. Following which, they were placed in a vacuum oven at 65°C overnight, backfilled with argon, and then pumped into an argon-filled glovebox while still warm for impedance spectroscopy.

If a film were reused for spectroscopy at a new salt concentration, the rinsing and soaking steps in 18 MΩ water were repeated to remove all salt. The initial 10 times the films were dried in a vacuum oven as above, and the impedance controls were repeated to insure no residual salt remained. These samples were found to be salt-free. Subsequently, the films were vacuum dried and then intercalated by spin coating in the same manner as previously described.

3.4.3 Physiochemical Characterization

XPS was performed on a Kratos AXIS Ultra Delay-Line Detector instrument with a magnetic immersion lens and a charge neutralization system. A monochromatized Al K α source was used, and a hemispherical analyzer. XPS data

analysis was performed using Casa XPS software, into which the Kratos instrument parameters were loaded. The data was calibrated using the ether peak, at 286.5 eV. It was then fit to a set of 4 envelopes, at 285.0 eV for hydrocarbon peaks, 286.5 eV for ether, 288 eV for ketone, and 289.5 eV for ester.²³ These restraints were lifted when the program performed a final fit.

AFM measurements were made using a Veeco AFM, with a MPP-21100 tip in tapping mode, at a resonance frequency of 83 kHz, and a spring constant of 3 N/m. The images were acquired using an 0.700 V amplitude setpoint and a 45.00 mV drive amplitude, with a drive phase of 40.84 degrees. The tip scanned at 1 Hz (20 $\mu\text{m}/\text{s}$) for 516 lines.

3.4.4 Electrochemical Characterization

Impedance spectroscopy was measured on dry samples in an argon atmosphere in a glove box. The ITO substrate served as a bottom contact, and a pair of mercury drop electrodes contacted the ITO and the top of the films in order to complete the measurement circuit for measuring impedance through the height of the film. Before each measurement, the mercury drop electrodes were tested on a clean ITO surface to ensure that electrode resistance was low (20Ω or below), and did not suffer from trapped air in the electrode tip or poor mercury wetting of the electrode wire.

The impedance was measured using a Solatron 1260 analyzer at an AC polarization of 10 mV, in the frequency range of 10^6 to 0.1 Hz, measuring 10 points per each frequency decade.

For impedance data consisting of a single arc (PEO-like films with no adhesion layer and the adhesion blast films), the conductivity of the film was taken

as the intercept of the arc with the real axis of the Nyquist plot (or the corresponding constant impedance reached on a Bode plot). For the more complicated spectra of the films with adhesion layers, the data was analyzed using MEISP 3.0, using an equivalent circuit consisting of the Transmissive Finite Warburg option in their library modified with an additional electrolyte loop (a charge transfer resistor in series with a transmissive diffusion element, both in parallel with a double layer capacitor) to account for our two electrolyte segments. This equivalent circuit matched the shape of the impedance data for all of the adhesion layer samples with errors less than a 0.01 standard deviation.

3.5 References

1. Dudley, N. J. Thin Film Micro-batteries. *Electrochem. Soc. Interface* **44–48** (2008).
2. Long, J. W., Dunn, B., Rolison, D. R. & White, H. S. Three-Dimensional Battery Architectures. *Chem. Rev.* **104**, 4463–4492 (2004).
3. Roberts, M. et al. 3D lithium ion batteries—from fundamentals to fabrication. *J. Mater. Chem.* **21**, 9876 (2011).
4. Arthur, T. S. et al. Three-dimensional electrodes and battery architectures. *MRS Bull.* **36**, 523–531 (2011).
5. Oudenhoven, J. F. M., Baggetto, L. & Notten, P. H. L. All-Solid-State Lithium-Ion Microbatteries: A Review of Various Three-Dimensional Concepts. *Adv. Energy Mater.* **1**, 10–33 (2011).
6. Xu, F. et al. Properties of lithium phosphorus oxynitride (Lipon) for 3D solid-state lithium batteries. *J. Mater. Res.* **25**, 1507–1515 (2010).

7. Perre, E. *et al.* Electrodeposited Cu₂Sb as anode material for 3-dimensional Li-ion microbatteries. *J. Mater. Res.* **25**, 1485–1491 (2010).
8. Rhodes, C. P., Long, J. W., Doescher, M. S., Dening, B. M. & Rolison, D. R. Charge insertion into hybrid nanoarchitectures: mesoporous manganese oxide coated with ultrathin poly(phenylene oxide). *J. Non-Cryst. Solids* **350**, 73–79 (2004).
9. Rhodes, C. P., Long, J. W., Pettigrew, K. A., Stroud, R. M. & Rolison, D. R. Architectural integration of the components necessary for electrical energy storage on the nanoscale and in 3D. *Nanoscale* **3**, 1731 (2011).
10. Rolison, D. R. *et al.* Multifunctional 3D nanoarchitectures for energy storage and conversion. *Chem. Soc. Rev.* **38**, 226–251 (2009).
11. Ratner, M. A. & Shriver, D. F. Ion transport in solvent-free polymers. *Chem. Rev.* **88**, 109–124 (1988).
12. Kumar, B. *et al.* Structural evolution and conductivity of PEO:LiBF₄--MgO composite electrolytes. *Electrochimica Acta* **46**, 1515–1521 (2001).
13. Croce, F., Appeticchi, G. B., Persi, L. & Scrosati, B. Nanocomposite polymer electrolytes for lithium batteries. *Nature* **394**, 456–458 (1998).
14. Comer, A. C., Kalika, D. S., Kusuma, V. A. & Freeman, B. D. Glass-transition and gas-transport characteristics of polymer nanocomposites based on crosslinked poly(ethylene oxide). *J. Appl. Polym. Sci.* **117**, 2395–2405 (2010).
15. Tao, R., Zhao, Y. & Fujinami, T. Lithium borate–PEO polymer electrolytes characterized with high lithium ion transference numbers. *Mater. Sci. Eng. B* **137**, 69–73 (2007).
16. Rietman, E. A., Kaplan, M. L. & Cava, R. J. Lithium ion-poly(ethylene oxide)

- complexes. I. Effect of anion on conductivity. *Solid State Ion.* **17**, 67–73 (1985).
17. Ito, Y., Kanehori, K., Miyauchi, K. & Kudo, T. Ionic conductivity of electrolytes formed from PEO-LiCF₃SO₃ complex with low molecular weight poly(ethylene glycol). *J. Mater. Sci.* **22**, 1845–1849 (1987).
18. Shin, J. Ionic liquids to the rescue? Overcoming the ionic conductivity limitations of polymer electrolytes. *Electrochim. Commun.* **5**, 1016–1020 (2003).
19. Shin, J.-H., Henderson, W. A., Scaccia, S., Prosini, P. P. & Passerini, S. Solid-state Li/LiFePO₄ polymer electrolyte batteries incorporating an ionic liquid cycled at 40°C. *J. Power Sources* **156**, 560–566 (2006).
20. Le Nest, J. F., Callens, S., Gandini, A. & Armand, M. A new polymer network for ionic conduction. *Electrochimica Acta* **37**, 1585–1588 (1992).
21. Le Nest, J. F. & Gandini, A. Electrolytes for solid-state batteries: glass transition temperature of polyether networks with and without alkali metal salts. *Polym. Bull.* **21**, 347–351 (1989).
22. López, G. P. et al. Glow discharge plasma deposition of tetraethylene glycol dimethyl ether for fouling-resistant biomaterial surfaces. *J. Biomed. Mater. Res.* **26**, 415–439 (1992).
23. Johnston, E. E., Bryers, J. D. & Ratner, B. D. Plasma Deposition and Surface Characterization of Oligoglyme, Dioxane, and Crown Ether Nonfouling Films. *Langmuir* **21**, 870–881 (2005).
24. Menzies, D. J. et al. An X-ray and neutron reflectometry study of 'PEG-like' plasma polymer films. *J. R. Soc. Interface* **9**, 1008–1019 (2011).
25. Menzies, D. J. et al. An X-ray and neutron reflectometry study of 'PEG-like' plasma polymer films. *J. R. Soc. Interface* **9**, 1008–1019 (2011).

26. Serrano Aroca, A., Monleón Pradas, M. & Gómez Ribelles, J. L. Plasma-induced polymerisation of hydrophilic coatings onto macroporous hydrophobic scaffolds. *Polymer* **48**, 2071–2078 (2007).
27. Parikh, D., Craver, B., Nounu, H. N., Fong, F.-O. & Wolfe, J. C. Nanoscale Pattern Definition on Nonplanar Surfaces Using Ion Beam Proximity Lithography and Conformal Plasma-Deposited Resist. *J. Microelectromechanical Syst.* **17**, 735–740 (2008).
28. Uchimoto, Y., Ogumi, Z., Takehara, Z. & Foulkes, F. R. Ionically Conductive Thin Polymer Films Prepared by Plasma Polymerization V. Preparation and Characterization of Solid Polymer Electrolyte Composed of Plasma Polymerized Complex. *J. Electrochem. Soc.* **137**, 35–40 (1990).
29. Uchimoto, Y., Ogumi, Z. & Takehara, Z. Ionically conductive thin polymer films prepared by plasma polymerization. Part 6. Plasma-parameter-dependent characteristics of solid polymer electrolytes composed of plasma polymerized tris (2-methoxyethoxy) vinylsilane-lithium perchlorate hybrids. *Solid State Ion.* **35**, 417–423 (1989).

CHAPTER 4

Iron Oxide Aerogels as Enhanced Cathode Materials for Li-ion Charge Storage

4.1 Introduction

High-performance cathode materials used in Li-ion batteries often contain expensive, toxic, and/or strategic metals (in the form of pure or mixed-metal oxides such as LiCoO_2), driving the search for less expensive, non-toxic alternatives. One such example is lithium-iron phosphate (LiFePO_4), which offers a thermodynamically favorable Li^+ -insertion potential of ~ 3.5 V vs. Li and a high reversible capacity ≥ 160 mA h g^{-1} , in conjunction with the cost and environmental benefits of iron-based materials¹. Binary iron oxides (i.e., rust) also exhibit promise as electrode materials, but inherent material limitations must be addressed, such as undesirable structural transformations during ion-insertion, the middling redox potential of the $\text{Fe}^{2+/3+}$ couple, and low insertion capacities (as observed with “classic” microcrystalline materials).^{2,3}

Iron oxides show enhanced activity for Li-ion insertion when prepared in forms that are inherently defective. For example, maghemite ($\gamma\text{-Fe}_2\text{O}_3$, or more properly $\text{Fe}^{3+}_{2.67}\square_{0.33}\text{O}_4$) is a cation-deficient spinel that inserts Li^+ into structural cation vacancies prior to the spinel→rocksalt transformation. This allows Li^+ storage at more positive potentials than observed for the defect-free analogue, magnetite (Fe_3O_4),⁴ allowing $\gamma\text{-Fe}_2\text{O}_3$ and related defect-spinel ferrites to be explored as candidates for positive electrodes. The cation vacancy population of

the γ -Fe₂O₃ structure can be increased further by substituting a fraction of the Fe³⁺ content with more highly oxidized cations (e.g., Mo⁶⁺, V⁵⁺),^{5,6} as we recently reported for a nanocrystalline Mo-substituted ferrite ($\text{Mo}_{0.59}\text{Fe}_{1.50}\square_{0.91}\text{O}_4 \cdot n\text{H}_2\text{O}$), which provides improvements in both Li⁺-insertion potential and charge-storage capacity relative to an analogous γ -Fe₂O₃ material.⁷

The population of electrochemically active defects in metal oxides can also be amplified when these materials are expressed in nanoscale forms,⁸ ranging from hollow nanospheres⁹ to 3-D ultraporous nanoarchitectures such as aerogels.¹⁰ Aerogels exhibit high specific surfaces areas (100–600 m² g⁻¹) that encourage surface-based defect formation, while also providing other structural characteristics that are advantageous for electrochemical functionality: (i) through-connected, nanometer-sized networks of solid particles that electrically wire the electrode architecture; (ii) through-connected networks of mesopores and/or macropores that enable efficient diffusion and transport of molecules and ions (e.g., the components of an electrolyte); (iii) nanoscale domains that minimize the solid-state diffusion distance for ion insertion. Previous investigations of V₂O₅ aerogels as Li⁺-insertion hosts illustrate how the aerogel framework can enhance electrochemical performance. For example, while microcrystalline V₂O₅ only accommodates ~2 Li per formula unit, V₂O₅ aerogels insert >4 Li per formula unit (chemically or electrochemically).^{11,12} Spectroscopic analysis of the Li⁺-insertion process implies that, beyond 2 Li⁺ per V₂O₅, Li⁺-insertion into V₂O₅ xerogels does not occur by traditional insertion mechanisms, but rather by processes at accessible defect sites that are not accompanied by a change in the oxidation state of V sites.¹³

Our goal is to explore the electrochemical charge-storage properties of FeO_x

aerogels, with an emphasis on compositions that are more defective. The composition of the FeO_x aerogels are varied by exploring 4 post-synthetic treatments: (i) in their as-synthesized, supercritically dried state (AS-SYN), and with additional mild temperature/atmosphere treatments: (ii) in air at 260°C (designated 260-AIR); (iii) argon at 260°C (designated 260-ARGON); and (iv) subsequently heating 260-ARGON in air at 260°C (designated 260-ARGON-AIR). These treatments promote specific crystalline forms such as Fe_3O_4 and $\gamma\text{-Fe}_2\text{O}_3$, while still retaining an aerogel-like architecture. We found that a reversible Li^+ -insertion capacity approaching 100 mAh g⁻¹ could be reached by heating the AS-SYN FeO_x to 260°C in air to form a more electrochemically stable relative of the AS-SYN FeO_x aerogel (which exhibits significant capacity fade over tens of cycles). When the AS-SYN FeO_x aerogels are heated in a low partial-pressure of O_2 (under argon flow to form 260-ARGON), the nanoparticles comprising the aerogel network transform into nanocrystallites with the spinel Fe_3O_4 -phase, resulting in lower Li-ion capacity and lower specific surface area. Subsequent thermal oxidation to form the 260-ARGON-AIR aerogel induces a topotactic conversion to nanocrystalline $\gamma\text{-Fe}_2\text{O}_3$, accompanied by the formation of cation vacancies that increase Li^+ -insertion capacity.

4.2 Results and Discussion

4.2.1 Physiochemical Nature of FeO_x Aerogels

As-prepared FeO_x aerogels are amorphous by X-ray diffraction (XRD), but as we demonstrated previously, post-synthetic thermal treatments under controlled atmospheres can be used to further tune the crystallinity, morphology, and porosity

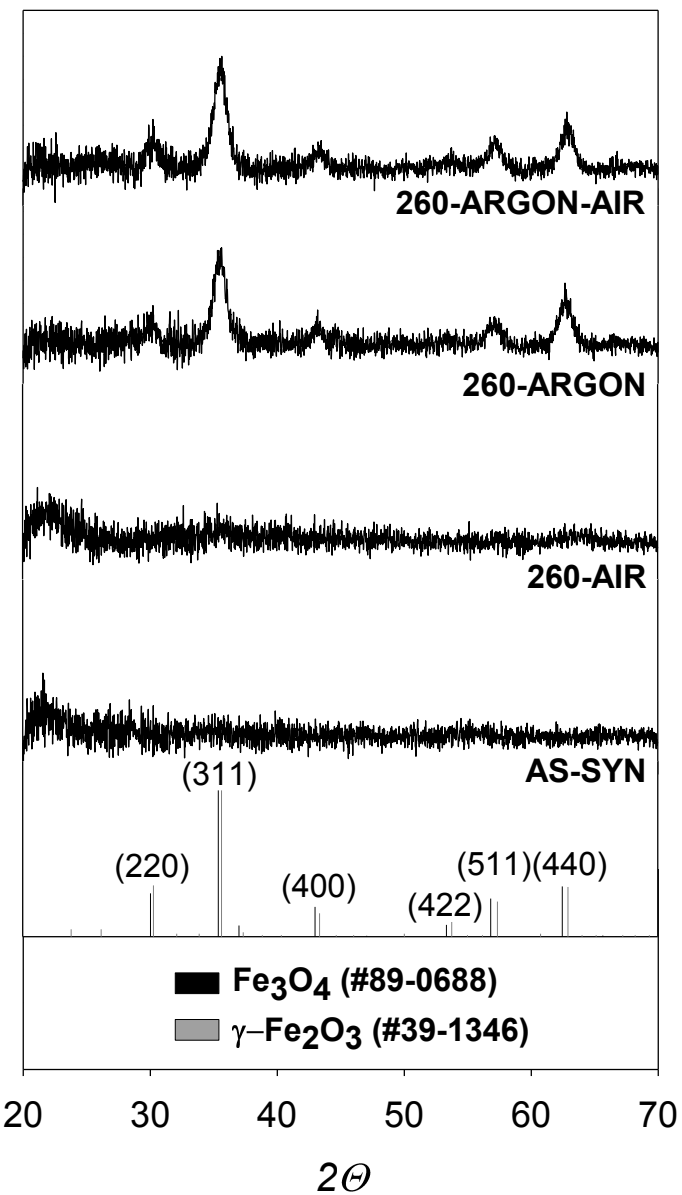


Figure 4.1. Powder X-ray diffraction for the four FeO_x aerogels, after background subtraction. The patterns are indexed relative to the JCPDS patterns for Fe_3O_4 and $\gamma\text{-Fe}_2\text{O}_3$. It can be seen that the argon processing induces crystallization into the magnetite/maghemite phase. No extraneous hematite is seen in any of the processing conditions (although it would be expected in air at higher temperatures).

of the aerogel. For example, heating FeO_x aerogels at 260°C in a low partial pressure of O_2 (i.e., flowing argon) yields a blackish, moderately densified solid, whose XRD pattern is consistent with nanocrystalline inverse spinel Fe_3O_4 (Figure 4.1). With further heating of this nanocrystalline Fe_3O_4 aerogel at 260°C in the presence of O_2 (static air), the crystallites undergo the well-known topotactic rearrangement to the cation-deficient spinel, $\gamma\text{-Fe}_2\text{O}_3$, with the aerogel becoming rust brown in color. A Scherrer analysis of the 311 reflection yields average crystallite sizes of 10.8 nm and 9.8 nm for the 260-ARGON and the 260-ARGON-AIR samples, respectively. With such small particle sizes, it is difficult to distinguish predominantly Fe_3O_4 aerogels from predominantly $\gamma\text{-Fe}_2\text{O}_3$ aerogels by XRD. Based on previous work by Long et al.¹⁴, we also heated the AS-SYN FeO_x aerogel in air at 260°C to form a still-disordered but moderately densified product to compare with the more nanocrystalline FeO_x aerogels.

Micrographs of our samples obtained by transmission electron microscopy (TEM) demonstrate that the average particle size for FeO_x materials remains < 10 nm in all cases, with minimal particle-size dispersity. As shown in Figure 4.2, the AS-SYN and 260-AIR materials both have average particle sizes of ca. 4 and 4.5 ± 1.1 nm respectively. Once the AS-SYN aerogel undergoes heat-treatments in the presence of argon, lattice fringes become more apparent and the average particle size increases to $6.5 \text{ nm.} \pm 1.8 \text{ nm.}$ Subsequent heating in air causes minimal change in particle size (260-ARGON-AIR, $6.6 \pm 1.8 \text{ nm.}$).

Raman spectra taken previously indicate that amorphous AS-SYN material contains vacancy content that correlates well with a maghemite ($\gamma\text{-Fe}_2\text{O}_3$) local structure.¹⁴ The 260-AIR, which appears to be poorly crystalline, preserved many of

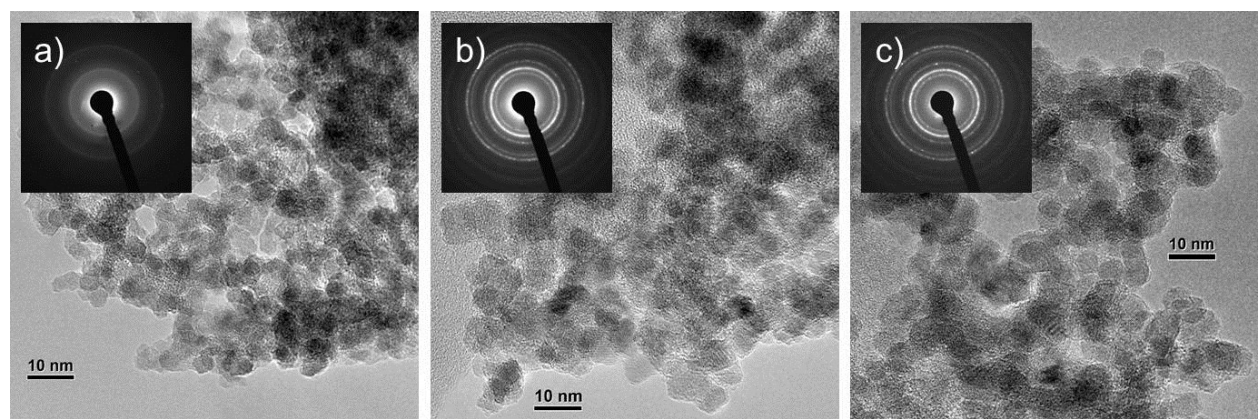


Figure 4.2. Transmission electron microscopy of the a) AS-SYN, (b) 260-AIR, (c) 260-ARGON, and (d) 260-ARGON-AIR materials.

these defect sites correlating with maghemite. The reductive heat treatment that induces crystallization (260-ARGON) reduces the amount of defects, producing nanocrystalline structures that are closer to the magnetite (Fe_3O_4) structure. And the follow-up oxidative heat treatment (260-ARGON-AIR), which retains the crystallization, reverses the phase as the structure regains vacancies and a maghemite character.

The iron oxide network is only half of the interpenetrating pair of networks in each aerogel. Its dual is the connected network of pores, which can be studied by porosimetry. The thin tendrils of the AS-SYN network impart a very high surface area of $616.2 \text{ m}^2 \text{ g}^{-1}$. This framework shows narrow pore-necks from the BHJ fitting of the gas desorption (Broekhoff-de-Boer method), with a focused distribution averaged at 21.5 nm (Figure 4.3). Oxidative heating in 260-AIR causes a decrease in surface area (to $262 \text{ m}^2 \text{ g}^{-1}$) which is commiserate with the thickening of the tendrils or pore walls. The 260-AIR material also displays a loss of pore volume for 20-nm pores. However the microporosity increases over a very broad, plateau-like range of larger micropores, centering around 36.8 nm in diameter. The reductive heat treatments (which beget long range order and crystal growth) are more destructive to the tendon architecture of the framework. 260-ARGON, correspondingly, shows the largest reduction in surface area, at $156 \text{ m}^2 \text{ g}^{-1}$. In the remaining aerogel-like regions, the pore size has grown to 29.0 nm in diameter. Interestingly, while this reductive heat treatment is destructive of the aerogel structure, it produces a more solid, stable structure as evidenced by the porosimetry study of further heat treatments. Although subsequent heating in air recovers the defect concentration by Raman,¹⁴ it does not significantly change the microstructure as can be seen by

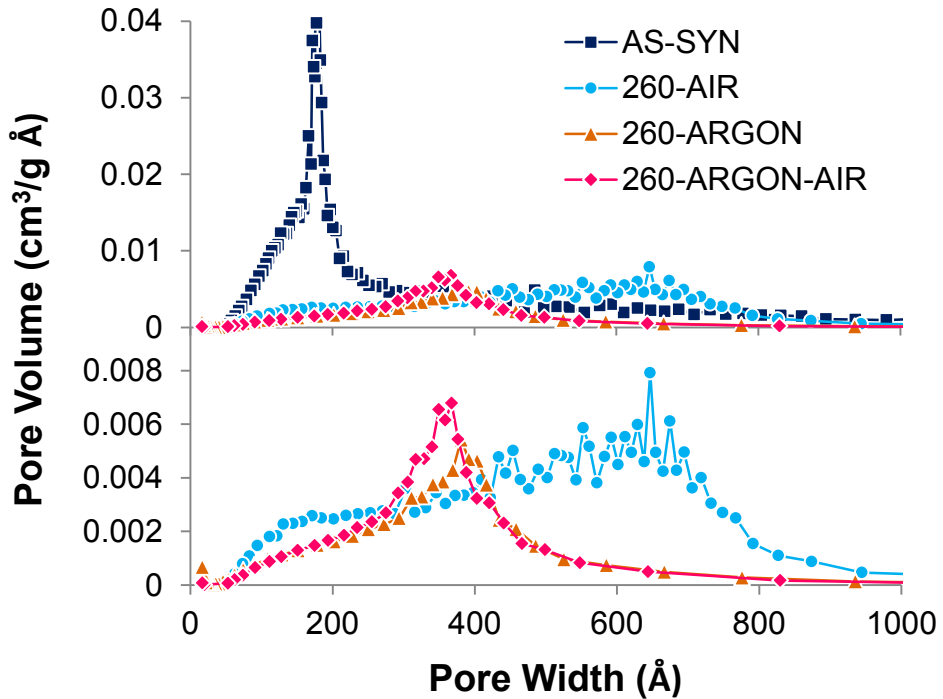


Figure 4.3. Pore volume distribution from BHJ desorption using Broekhoff-de Boer thickness calculations. Shown above is the full scale pore volume for all four aerogels, and below is the same data for the three heat treated aerogels on a reduced pore volume scale.

both the micrographs and the porosimetry data. The surface area ($171\text{ m}^2\text{ g}^{-1}$) and pore size distribution remain the same within the error that can be expected from sample activation.

In terms of local structure and defect density, we have seen previously by Raman that the oxidative and reductive heat treatments are reversible.¹⁴ However, in terms of long range order and macrostructure, the initial reduction induces crystallization and framework destruction that are irreversible.

4.2.2. Electrochemistry

We have characterized the effects of the heat treatments on the physiochemical properties of our four frameworks. We can now explore how these properties pertain to their electrochemical performance against lithium in a half-cell.

Using cyclic voltammetry we see a blended insertion for our materials across the cathode-appropriate voltage range of 2 to 4 V. This region typically shows negligible lithium insertion for binary iron oxides. The AS-SYN amorphous maghemite and 260-AIR weakly crystalline maghemite materials both show large capacities across the full range investigated in Figure 4.4. However the AS-SYN material loses capacity with every cycle, whereas the 260-AIR material shows stable cycling at these high capacities. After a reducing heat treatment, the crystalline magnetite (Fe_3O_4) 260-ARGON with a low surface area and microporosity displays a large reduction in capacity. It also shows a cut-off potential for intercalation near 3.5 V, whereas before reduction the materials intercalate up to 4 V. This supports our vacancy model of intercalation as increasing the amount of vacancies is expected to increase not only the capacity but also the upper limit of the

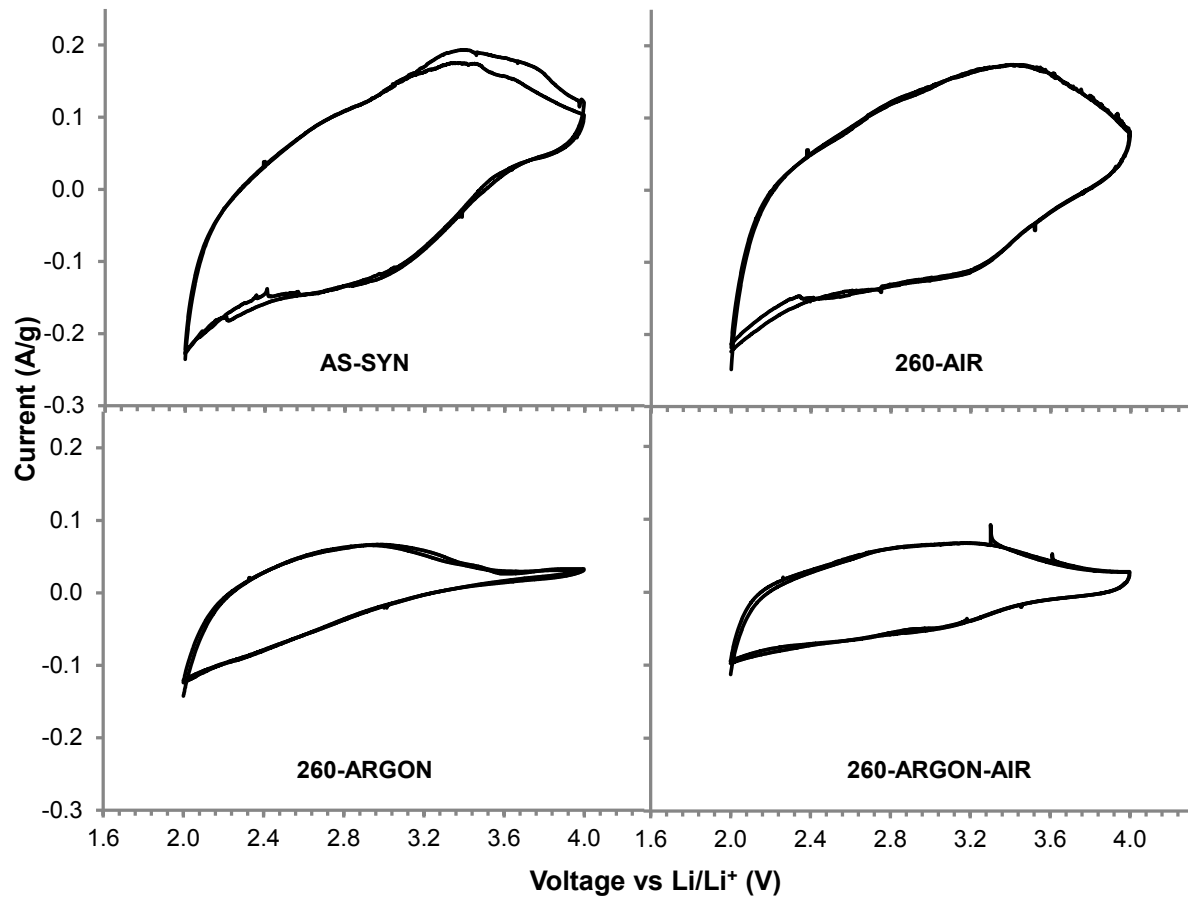


Figure 4.4. Cyclic voltammetry for each aerogel in a coin cell against Li. The sweep rate was 0.5mV s^{-1} , and cycles 2 and 3 are shown for each material. The defect-rich AS-SYN and 260-AIR materials show higher capacities than the reduced 260-ARGON material.

intercalation window. Upon restoring the vacancies to the reduced material through a further oxidative heat treatment, the 260-ARGON-AIR has an increased capacity. However, it cannot recover to match the 260-AIR sample which was never crystallized and has higher surface area and microporosity.

Looking at the same samples galvanostatically at a 20 mA g^{-1} rate in Figure 4.5, we see excellent performance, at almost 100 mA h g^{-1} , from the disordered, defect-rich maghemite framework (260-AIR). This demonstrates that a high surface area architecture of a simple rust (binary iron oxide) can have appreciable capacity as a lithium-ion cathode. A much lower performance is observed from the reduced framework (260-ARGON) which has a lower surface area and fewer vacancies. The AS-SYN amorphous maghemite initially compares well to the 260-AIR weakly crystalline maghemite structure, but it suffers from low cycling stability. And as before, regaining the vacancy content in the 260-ARGON-AIR is not sufficient to regain the capacity of the 260-AIR.

However, when normalizing the galvanostatic data to surface area in Figure 4.6, it becomes clear that the 260-ARGON-AIR does regain full capacity per exposed surface along with the return of its vacancy content. It is the destruction of porosity that prevents the material from regaining its gravimetric capacity. It can also be seen in this graph that the AS-SYN material cannot fully utilize all of its surface area, showing a much lower capacity per exposed surface than all of the other materials. The weak local ordering provided by the air heat treated sample (260-AIR) provides an increase in capacity per exposed surface area, even though the treatment somewhat lowers the overall surface area of the framework.

Furthermore, the lesser gravimetric capacity of the 260-ARGON framework is

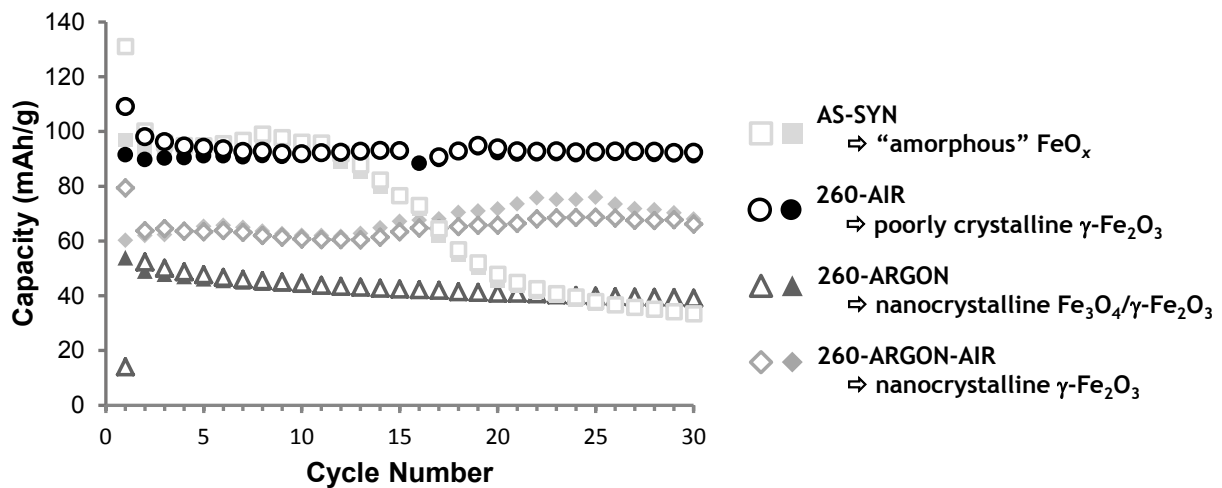


Figure 4.5. Galvanostatic cycling of each material against Li in coin cells (gravimetric). Whereas the initial high capacity of the AS-SYN material fades with cycling, the 260-AIR material has much improved capacity retention. 260-ARGON has a much lower capacity, and 260-ARGON-AIR recovers capacity but remains lower than the non-crystalline samples.

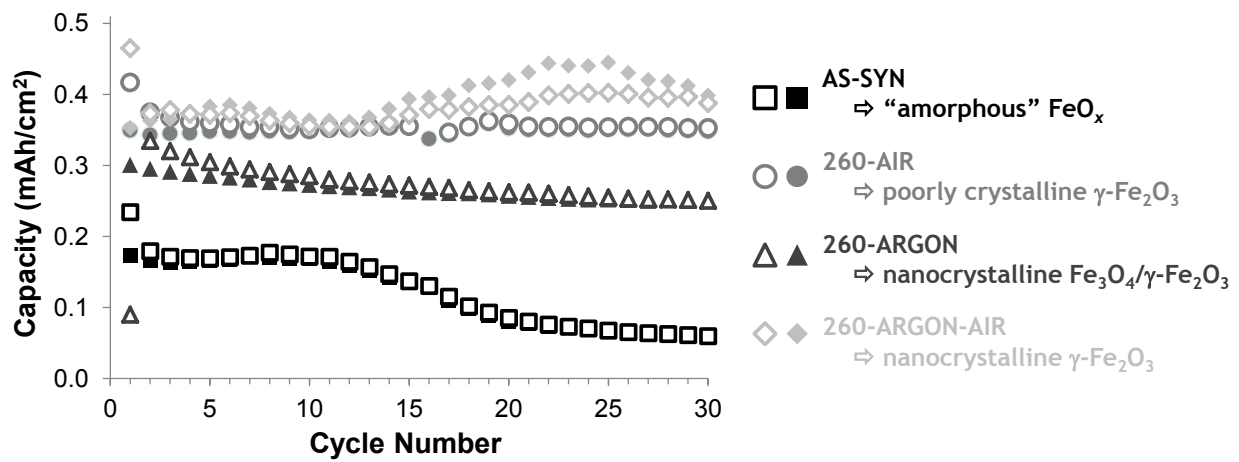


Figure 4.6. Surface-area normalized galvanostatic cycling. 260-ARGON-AIR regains its capacity per surface area as compared to the higher surface area 260-AIR material. 260-ARGON has a lower capacity than can be accounted for by its lower surface area, and AS-SYN cannot take advantage of its high surface area without further heat treatments.

not exclusively a factor of the decreased surface area, but is also an innate property of the less-defective material, which has a lower capacity per its remaining exposed surface.

4.3. Conclusions

Using a high surface area aerogel framework to create a defect-rich structure with high accessibility to the defect (surface) sites, we were able to synthesize an unadulterated binary iron oxide with high lithium insertion capacity (almost 100 mA h g^{-1}) and high cycling stability at cathode-appropriate voltage potentials. We were able to show that the high capacity was correlated with increased defect concentration and increased surface area (with the expectation that truncation at the surface is the source of our defects). Additionally, we were able to show that a completely amorphous framework lacked both the fully enhanced capacity expected for its exceptionally high surface area, and also the cycling stability that was gained by the heat-treated frameworks. This behavior supports the fact that a threshold-degree of local ordering is beneficial for both capacity and cycling stability. However, the optimal gravimetric capacity depends on the retention of a high surface area structure, which requires that heat treatments not only retain defects and impart local ordering, but also refrain from inducing long range ordering, as crystallization allows for irreversible framework destruction. This work shows that high Li-ion capacities can be achieved for materials with inherently poor insertion capacities by utilizing high surface area materials with tailored surface-chemistry.

4.4. Experimental

4.4.1 Synthesis and Processing

Iron oxide aerogel monoliths were prepared following our previous work on magnetic FeO_x aerogel frameworks, using epichlorohydrin as the proton scavenging epoxide that drives the condensation of the Fe^{3+} aquo-ions into a slow-forming gel.¹⁴

Briefly, epichlorohydrin (3.88 mL, Aldrich) was added to a stirring 0.33 M solution of $\text{FeCl}_3 \cdot 6\text{H}_2\text{O}$ (1.338 g, Aldrich) in anhydrous ethanol (15 mL, Warner-Graham). The sol was allowed to stir for an additional 5 min, and then decanted into HDPE vials open at both ends. The vials were sealed with Parafilm M and aged for 17 h. The gels were transferred into solvent exchange jars by removing both the bottom (caps) and the top (Parafilm) from the vials to release the monoliths for gentle decanting. The mother liquor in the pores was exchanged with ethanol, to remove any impurities, followed by acetone to allow for the best miscibility with liquid CO_2 .

The wet gels were transferred under acetone into a super critical drier (Polaron, Quorum Technologies), and solvent exchanged with liquid CO_2 at 10°C. The CO_2 was then taken to 44°C and 9 MPa, well beyond its super critical point of 31°C and 7.4 MPa, and held for an hour before the pressure was released overnight. AS-SYN samples were studied with no further heat treatments.

The high pO_2 heat treatments were performed in alumina boats in a Thermolyne muffle furnace under static air. The temperature was raised at 5°C min^{-1} from room temperature to 260°C, held for 10 h, then allowed to cool (260-AIR).

The low pO_2 heat treatments were performed in the same boats in a fused

quartz tube in a Lindberg model 55033 tube furnace modified such that the temperature was measured inside the quartz tube. Argon was flowing over the samples at $37 \text{ cm}^3 \text{ min}^{-1}$, starting 2 h before the heat ramp began, and continuing until the samples had cooled completely. This furnace was also ramped at 5°C min^{-1} from room temperature to 260°C , held for 10 h, then allowed to cool (260 -ARGON).

Samples referred to as 260-ARGON-AIR were first subjected to a low pO_2 heat treatment, followed by a separate high pO_2 heat treatment.

4.4.2 Characterization and Instrumentation

Surface areas and porosities were measured using nitrogen adsorption (Micromeritics ASAP2010 porosimeter). All samples were degassed at 80°C for 24 to 36 h in a vacuum oven, before being backfilled with nitrogen at room temperature and immediately placed on the instrument and evacuated. Pore size distributions were calculated from adsorption isotherm data using Micromeritics DFTPlus software (classical model, cylindrical pores, Broekhoff-de Boer theory).

X-ray diffraction was run on a Bruker D8. Scans were recorded between 20 and $70^\circ 2\theta$, with a step size of degrees and an integration time of s per step. For scans showing crystallinity, particle sizes were calculated from the peak indexed to the (311) peak of the magnetite/maghemite crystal structure

Transmission electron microscopy was performed on well ground samples which were drop-cast from suspension onto a holey carbon film on a copper grid. The micrographs were obtained using a JEOL 2010F TEM with a Gatan CCD camera.

Electrochemical measurements were all performed in LIR 2032 coin cells that consisted of (working outward to center) a Teflon-separated outer shell, a spring

(on the lithium side), 2 stainless steel spacers, the two electrodes (our cathode and a lithium piece, and a 2400 Celgard spacer at the center. The cells were assembled in an argon filled glove box. The cathode consisted of a 0.005" aluminum current collector which was painted with a well-mixed slurry of 10:10:80 weight % acetylene black (Alfa Aesar): PVDF: active material in NMP. The electrode was partially dried at 50°C under argon overnight before being thoroughly dried at 120°C under vacuum for 3 h. Both the cathode and the Celgard were infiltrated with electrolyte at -20 mmHg for 1 h, with agitation to gently remove trapped bubbles after 30 min. Electrochemical measurements were made using the Arbin BT2000, in the range of 2 V to 4 V. Unless otherwise noted, all cycling was done at 20 mA g⁻¹ of active material.

4.5 References

1. Ohzuku, T. & Brodd, R. J. An overview of positive-electrode materials for advanced lithium-ion batteries. *J. Power Sources* **174**, 449–456 (2007).
2. Thackeray, M. M. Spinel electrodes for lithium batteries. *J. Am. Ceram. Soc.* **82**, 3347–3354 (1999).
3. Thackeray, M. M., David, W. I. F. & Goodenough, J. B. Structural characterization of the lithiated iron oxides $\text{Li}_x\text{Fe}_3\text{O}_4$ and $\text{Li}_x\text{Fe}_2\text{O}_3$ ($0 < x < 2$). *Mater. Res. Bull.* **17**, 785–793 (1982).
4. Pernet, M., Strobel, P., Bonnet, B. & Bordet, P. Structural and electrochemical study of lithium insertion into $\gamma\text{-Fe}_2\text{O}_3$. *Solid State Ion.* **66**, 259–265 (1993).

5. Bouet, L., Tailhades, P., Rousset, A., Domenichini, B. & Gillot, B. Mixed valence states of iron and molybdenum ions in $\text{Mo}_x\text{Fe}_{(3-x)}\text{O}_4$ magnetites and related cation deficient ferrites. *Solid State Ion.* **52**, 285–286 (1992).
6. Gillot, B. & Nivoix, V. New cation-deficient vanadium-iron spinels with a high vacancy content. *Mater. Res. Bull.* **34**, 1735–1747 (1999).
7. Hahn, B. P. *et al.* Electrochemical Li-ion storage in defect spinel iron oxides: the critical role of cation vacancies. *Energy Environ. Sci.* **4**, 1495 (2011).
8. Hahn, B. P., Long, J. W. & Rolison, D. R. Something from nothing: enhancing electrochemical charge storage with cation vacancies. *Acc. Chem. Res.* **46**, 1181–1191 (2013).
9. Koo, B. *et al.* Hollow iron oxide nanoparticles for application in lithium ion batteries. *Nanoletters* **12**, 2429–2435 (2012).
10. Rolison, D. R. & Dunn, B. Electrically conductive oxide aerogels: new materials in electrochemistry. *J. Mater. Chem.* **11**, 963–980 (2001).
11. Dong, W., Sakamoto, J. S. & Dunn, B. Electrochemical properties of vanadium oxide aerogels. *Sci. Technol. Adv. Mater.* **4**, 3–11 (2003).
12. Passerini, S. *et al.* XAS and electrochemical characterization of lithiated high surface area V_2O_5 aerogels. *Solid State Ion.* **104**, 195–204 (1997).
13. Rhodes, C. P., Dong, W., Long, J. W. & Rolison, D. R. in *Solid State Ion.* **VI**, 478 (Electrochemical Society, 2003).
14. Long, J. W. *et al.* Nanocrystalline iron oxide aerogels as mesoporous

magnetic architectures. *J. Am. Chem. Soc.* **126**, 16879–16889 (2004).

CHAPTER 5

Beyond Li-ion: Silicon as a Host for Emerging Energy Storage Systems

5.1. Introduction

Li-ion batteries with graphite-based anodes are well established as the dominant commercial battery archetype for portable electronics, and recently have captured the market for electric vehicles and larger scale applications as well.¹ They have high energy densities and also high cycle life, with newer formulations such as those including a LiFePO₄ cathode providing enhanced safety and cycle life.²

Silicon is the heir-apparent for the next generation of Li-ion battery anode materials, as an earth abundant element with ten times the theoretical capacity of conventional graphite anodes (Li₁C₁ vs. Li_{4.4}Si₁). However, bulk Si cannot reversibly utilize its theoretical capacity because it cannot withstand the mechanical stresses associated with repeated swelling (up to 400% of its initial volume) and de-swelling as it cycles. Nanostructured Si alleviates the mechanical stresses by enabling the material to swell on the nanoscale without propagating the volume change to the bulk. We can make mesoporous Si films through a Mg-vapor reduction of diblock-copolymer-templated mesoporous SiO₂.³ This material presents an interconnected network of cubic pores (10 – 15 nm) demarcated by walls composed of 13 – 20 nm polycrystalline Si grains. Thin films of our porous silicon show reversible cycling behavior at a variety of C rates. Lithium capacity ranges from 3000 mAh/g at 1C to 2100 mAh/g at 20C. Coulombic efficiency was near 100 % and the capacity values

at 1C were recoverable at each of the various C rates. These data suggest that a nanostructured silicon material with thin walls surrounded by ordered pores has the ability to override the longstanding problem of poor cycle life in Si materials for Li-ion batteries, while maintaining the high capacities that make Si a desirable anode material.

Silicon thermally alloys with a large selection of metal ions besides lithium, and a logical extension of the progress in Li-ion systems would be to explore the potential of porous silicon films in other monovalent (Na^+ , K^+) and multivalent (Mg^{2+} , Al^{3+}) energy storage systems. All four elements are lower in cost and higher in natural abundance than lithium, and the multivalent cations provide for doubled or tripled electron storage per cation.

One particular system of interest is Na-ion batteries. Sodium is a cheaper alternative to lithium, but has the disadvantage of having a somewhat larger radius and thus being more difficult to reversibly store. It may be difficult to overcome the lack of reversibility for larger ions in intercalation systems or as participants in conversion reactions, because in both cases the ion has to fit into and conduct through set crystal structures. However, an electrode material such as Si that stores ions through alloying processes may allow for much greater flexibility in the size of its guest ions. Just as in regard to lithium, bulk silicon traditionally has poor cycle life in sodium systems due to the inherent volume expansions and contractions that accompany the large storage capacities. It is expected that an architecture which provides pores to accommodate the expansion would give a more robust structure for Na-ion storage in the same way it does for Li-ion storage.

Following this logic, systems similar to silicon have been optimized with

exciting results. A Sb-C milled composite system, which alloys with sodium, shows sodium capacities >600 mAh/g.⁴ Capacities fade when cycled traditionally, but when optimized with a 5% flouroethylene carbonate (FEC) additive, the capacity remains steady for over 100 cycles.⁴ SbSn nanocomposites recently achieved over 400 mAh/g in a new study, without utilizing such optimizations.⁵ Another alloying anode, Pb, also shows promise for Na-ion systems. Rather than the importance of the electrolyte, it was found that the lead system required optimization of the composite⁶ (although this type of optimization is routinely performed now with silicon composites). The authors found reversible insertion into lead of over 125 mAh/g.

The concept of accommodating a larger volume expansion can be extended further to examine potassium storage in porous Si films. Potassium ions in solution have a smaller Stokes radius than lithium due to fewer solvating ions, and so have higher diffusion rates. Additionally, potassium is cheaper and more abundant than lithium, and the K/K⁺ couple occurs at almost the same potential. The interstitial tetrahedral spaces in silicon can accommodate species with a radius of 92.7 pm with no expansion (from the lattice parameters of crystalline silicon). Elemental lithium has a radius of 152 pm, explaining the large expansion of the Si lattice upon lithiation. Elemental sodium and potassium have radii of 186 and 231 pm respectively. Whereas sodium is similar to lithium, storing potassium represents an appreciable difference in the requirements for lattice expansion when inserting into electrodes. This has been achieved in cathode intercalation materials by finding structures with exceptionally large interstitial spacing, such as Prussian Blue.^{7,8} An alloying anode structure like silicon is disordered by the insertion of guests, and

becomes amorphous after a certain number of cycles. A material like this which has the ability to store cations even when in an amorphous state may present advantages as a storage system for such large guests, as local atomic disorder caused by their insertion does not necessarily reduce the capacity.

In the case of the multivalent cations, Mg²⁺ is of interest due to its similarity in size to lithium and the high volumetric capacity of the metallic magnesium anode (3833 mAh/cm³).⁹ Magnesium forms a variety of SEI layers depending on the solvent and electrolyte present. However, the SEI layers that form on the magnesium anode in most solvents is passivating and does not conduct magnesium or electrons. Large overpotentials are required in order for the cyclic dissolution of the magnesium, due to the prerequisite breakdown of that SEI layer.¹⁰ In contrast to Li-ion and Li metal anodes, which require the optimization of their SEI layer in order to achieve high capacity retention and cycling efficiency, magnesium anodes only function when there is no SEI layer.¹⁰ Magnesium is reactive with many of the common electrolyte salts (TFSI, ClO₄, PF₆), and readily forms a passivating layer in the presence of these anions.⁹ However, magnesium organohaloaluminate salts developed by Aurbach et al. are soluble in glyme ethers and allow for reversible plating and dissolution of magnesium, with no passivating film formation.^{11,12} These organomagnesium salts suffer from oxidative instability at non-inert current collectors, leading to a voltage window of only 2.2V. This can also be circumvented by using more complex, tailored cations, in a study that is ongoing at Toyota.¹²

Another solution to the small voltage window is to move away from the complex, oxidatively unstable, electrolyte solutions and use conventional battery electrolytes. This is possible if the anode of the Mg²⁺-ion battery were not the

easily passivated Mg metal anode, but instead a more amenable material that had a high capacity for reversible Mg²⁺ insertion. Such a material would need to have large open spaces to accommodate the divalent cation, and a high stability of its crystal structure in order to be able to withstand the divalent reduction. The open interstitial sites of metallic Tin have performed well in this regard, reaching reversible capacities of over 200 mAh/g for 10 cycles at 0.01C rates.⁹ The magnesylation of tin is an alloying reaction rather than an intercalation reaction, and this may be a favorable strategy for storing magnesium reversibly.

First we will explore the porous silicon thin films physiochemically, and then we can explore their electrochemical performance as potential battery anodes for a variety of energy storage systems. Specifically, we compare the excellent performance as a lithium-ion anode to the capacities and cycling stabilities of the same porous thin films when inserting other cations. We examine sodium, and briefly look at potassium, and then examine magnesium as an example of a multi-valent energy storage ion.

5.2 Experimental

5.2.1 Thin Film Silica Preparation

Synthesis of the silica mesoporous film utilizes the diblock copolymer PEP-PEO. Poly((ethylene-*a/t*-propylene)-*b*-block-poly(ethylene oxide), with a mass ratio of PEP(3900)-*b*-PEO(4000), a block ratio of PEP₅₆-*b*-PEO₉₁, and with a PDI = 1.05, was synthesized using reported methods.^{13,14} Briefly, polyisoprene was grown by anionic polymerization, terminated with an -OH group and then hydrogenated over Pd/C. The resulting PEP-OH was subsequently extended by anionic polymerization

of ethylene oxide.

PEP-PEO (0.03 g) is dissolved in ethanol (1.5 mL) at 60 °C overnight, after which TEOS (400 µL), 200 µl of 18 MΩ water, and 200 µl of a 1N HCl solution in ethanol were simultaneously added to the polymer solution. The 2 solutions are stirred together for 1 h and let age for 1 day. The final solution is used in a <20% relative humidity controlled chamber. Films are pulled out of the resultant solution on clean substrates at a withdrawal rate of 1 cm/min. Unless otherwise noted the substrates consist of a 200 nm thick film of nickel deposited on p-doped Si by e-beam evaporation. The dry films are immediately transferred to an 80 °C oven, and kept at 80 °C for at least an hour. The films are then calcined at 400 °C in air using a 3 h ramp to 150 °C, followed by a 150 °C soak for 3 h, followed by a second 3 h ramp to 400 °C, and a second 3 h soak at 400 °C.

5.2.2 Magnesium Reduction

3 cm x 1 cm SiO₂ films were placed into a stainless steel chamber, which has an inner volume of 15 cm³, in a glove box with an argon atmosphere. 50 mg of Mg pellets were placed 2 cm away from the films, and the chamber was capped with a stainless steel lid. To generate Mg vapor pressure, the chamber was heated to 680°C, with a 3 h ramp followed by a 3 h soak. To remove magnesia, the film was immersed in 1M HCl for 5 min, followed by 4.8% HF for 1 min to remove residual silica. Sample substrates were thoroughly washed with ethanol after each acid treatment.

5.2.3 Electrochemical Setup

To prepare samples for electrochemistry, the back of the silicon substrate was sealed to prevent contact with the electrolyte. The back and edges of each

sample was covered in Loctite adhesive: a hard epoxy that is inert in the electrolyte. To cycle the samples, an Arbin Instruments BT-2000 potentiostat was connected through a N₂ filled glove box. The electrolyte was prepared by dissolving 1.07 g lithium perchlorate in 10 mL propylene carbonate to make a 1 M solution. Samples were cycled in a three electrode configuration utilizing the sample as the working electrode and lithium foil as both the counter and reference electrodes. The voltage window used was 0.07 V to 1.5 V vs Li/Li⁺. Samples were tested at cycling rates between 1 C and 20 C. C rates here are calculated assuming 1C corresponds to complete charge or discharge in 1 hour at the measured capacity. If the theoretical capacity of 4200 mAh/g is used instead, all C rates would increase by about a factor of 2. This corresponds to current densities ranging from 2 A/g to 40 A/g.

5.2.4 Sample Weight Measurement Preparation

Sample weight was determined by fully dissolving each film after cycling and using ICP to determine the total silicon mass. To dissolve the porous silicon without disrupting the silicon substrate, the whole sample was first immersed in HNO₃, which dissolved the nickel or titanium coating and allowed the mesoporous silicon film to de-adhere from the substrate and float into the solution. The nitric acid also served to oxidize the silicon. After removing the bulk silicon substrate, 10% HF was added to fully dissolve the oxidized mesoporous silicon film without the problem of contamination.

5.2.5 Analysis Techniques

Low angle X-ray diffraction (XRD) was collected using a Panalytical Xpert PRO diffractometer ($\lambda = 1.54 \text{ \AA}$). Films were sealed in Mylar to prevent oxidation during

data collection. Data was collected in a θ - θ geometry with the incident beam near grazing incidence. This experiment thus allowed us to examine mesoscale periodicity normal to the substrate (out-of-plane diffraction). High angle XRD was measured with a Bruker AXS D8 Discover instrument on a sample sealed under argon atmosphere with a Kapton film. SEM utilized a JEOL 6700F with an EDAX attachment and the sample was loaded within a minute of removal from the glove box to minimize oxygen exposure.

5.3 Results and Discussions

5.3.1 Physiochemical Analysis

Physiochemical analysis was performed on these films in prior work, by C. Kang. To summarize, the success of the magnesylation reaction was confirmed by a combination of SEM, low angle XRD, and high angle XRD. Figure 5.1a shows the porosity of the silica films by SEM, and Figure 5.1b shows the same film after magnesylation. After reduction by magnesium and the subsequent HCl and HF washes, the surface retains the ordered porosity, although more disorder is present. Small-angle X-ray diffraction in Figure 5.1c re-confirms that the mesostructure is preserved upon magnesium reduction, and additionally quantifies the contraction that is observed during Mg-vapor thermal processing. No further contraction occurs after the washing steps. Figure 5.1d presents the high angle XRD, showing the presence of Si and MgO after magnesylation, and the presence of only Si after an acidic wash to remove the MgO, confirming that the films are crystalline Si. Scherrer analysis of the domain size from the diffraction peak width indicates that the crystallite diameter in the film is \sim 13 nm.

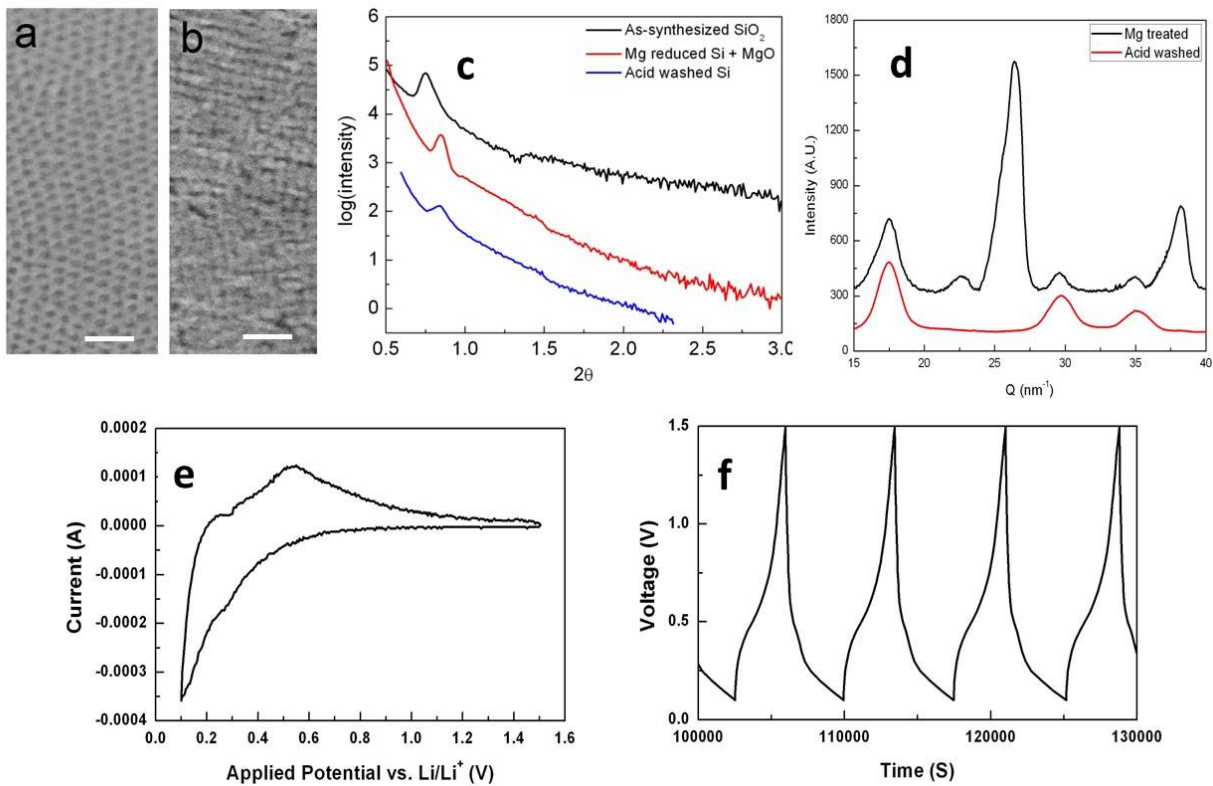


Figure 5.1 A summary of physical characterization and Li-ion insertion studies of templated porous Si films from previous work in submission by C. Kang. (a) SEM of silica, scale bars are 100 nm. (b) same film after magnesylation followed by HCl/HF treatment. (c) low angle XRD of templated mesoporous silica and silicon. After magnesylation, diffraction peaks shift to lower angle, indicating pore shrinkage in the out-of-plane direction. (d) high-angle XRD, after Mg treatment. Diffraction peaks corresponding to crystalline Si at 17.5, 29.0, and 34.0 nm⁻¹. Peaks corresponding to MgO at 22.5, 26.5, and 28.0 nm⁻¹. After acid treatment, MgO peaks disappear and only Si peaks remain. (e) CV of porous magnesylated and acid-washed Si at 50 mV/s. (f) galvanostatic cycling of templated porous Si. The rate was 1 A/g, corresponding to approximately 1C.

5.3.2 Li⁺ Insertion

Nanoporous silicon films were cycled as half cells in a flooded three electrode cell against Li/Li⁺, using either galvanostatic or potentiostatic methods. This analysis was also performed in previous work by C. Kang. In summary, the templated porous Si films showed high Li-ion capacities and high cycle life. The first cycle contained a large an irreversible capacity, resulting from SEI layer formation, which was omitted from both plots. Figure 5.1e shows a typical cyclic voltammogram (CV) obtained after SEI formation at a scan rate of 50 mV/s rate collected between 0.07 V and 1.5 V versus Li/Li⁺. Li insertion is observed at low potentials, below 0.2 V, and a peak corresponding to Li extraction is observed at 0.51 V. This data is consistent with CV curves in the literature for other forms of silicon.¹⁵ Galvanostatic data in Figure 5.1f shows selected cycles at a rate of 2C between 0.07 V and 1.5 V versus Li/Li⁺. Insertion occurs at potentials of 0.2 V and below, and de-insertion occurs at potentials of 0.5 V and above. These values match well with CV data presented in Figure 5.1e. Silicon had previously been established as an anode material that shows high capacity, but poor cycling stability. The stable cycling shown in these porous silicon films is a testament to the role that nanoscale architecture plays in modifying the cycling stability of materials that undergo a large volume expansion upon Li-ion insertion.

5.3.3 Electrochemical Exploration of the Monovalent Cations Na⁺ and K⁺

After summarizing the physiochemistry and Li-ion electrochemistry of the films, we can explore their electrochemical performance as potential battery anodes for a variety of energy storage systems. While Li-ions cycle stably in and out of the porous silicon at over 1000 mAh/g for hundreds of cycles, the same films show

difficulty establishing a stable capacity for sodium insertion. In Figure 5.2, it can be seen that the porous silicon films have some capacity for sodium. There is a reduction peak in the CV as the voltage approaches 0 V vs Na/Na⁺, and a corresponding oxidation that is spread over a wide range, but has a peak at around 2.5 V. Unfortunately, this is a large voltage hysteresis, indicating a large kinetic barrier that would yield poor energy efficiency in a battery. Oxidation at this high voltage was not seen in other Na-ion systems.^{4,4,6} Our system may have a slow electron transfer step, possibly removal of sodium from the crystalline Si lattice.

Examining the sodium insertion into the porous silicon films galvanostatically in Figure 5.3, the same insertion and de-insertion reactions are seen. Here, there is a capacity fade in every cycle. Additionally, there is a poor electrochemical efficiency. The efficiency and capacity fade could be related to the poor electrical kinetics that cause the irreversibility in Figure 5.2. They could also be related to the high voltage required in the CV for de-insertion of sodium. Possibly 2.5 V isn't high enough of a voltage range for our system, and more sodium is inserted every cycle than can be removed. However, 2.5 V is the upper limit of an acceptable value for a battery anode, and a survey of previous studies saw de-insertion at much lower voltages.¹⁶ Solving the problem of irreversibility as well as the problem of the capacity fade is required.

However, despite the low efficiency and capacity fade, sodium cycles with very high capacities. At very slow rates of 50 μ A ($\sim 1 \times 10^{-5}$ C), our films display reversible capacities of over 600 mAh/g in Figure 5.3. When cycled at even slower 10 μ A rates, the initial capacities are even higher, but reversible capacity over many cycles is near the same. It seems that \sim 600 mAh/g is the limit that can be

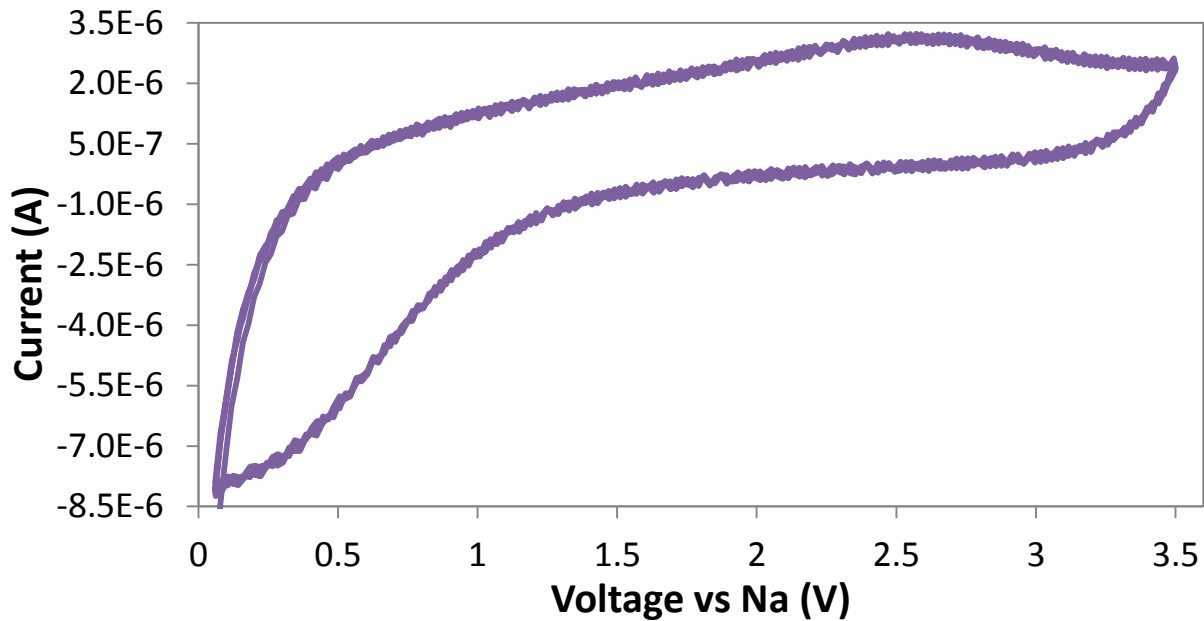


Figure 5.2. Cyclic voltammogram of a porous silicon thin film in a sodium perchlorate flooded cell vs a sodium reference electrode, at 4 mV/s. The first 2 cycles are shown, and the capacity does not appear to fade between cycles.

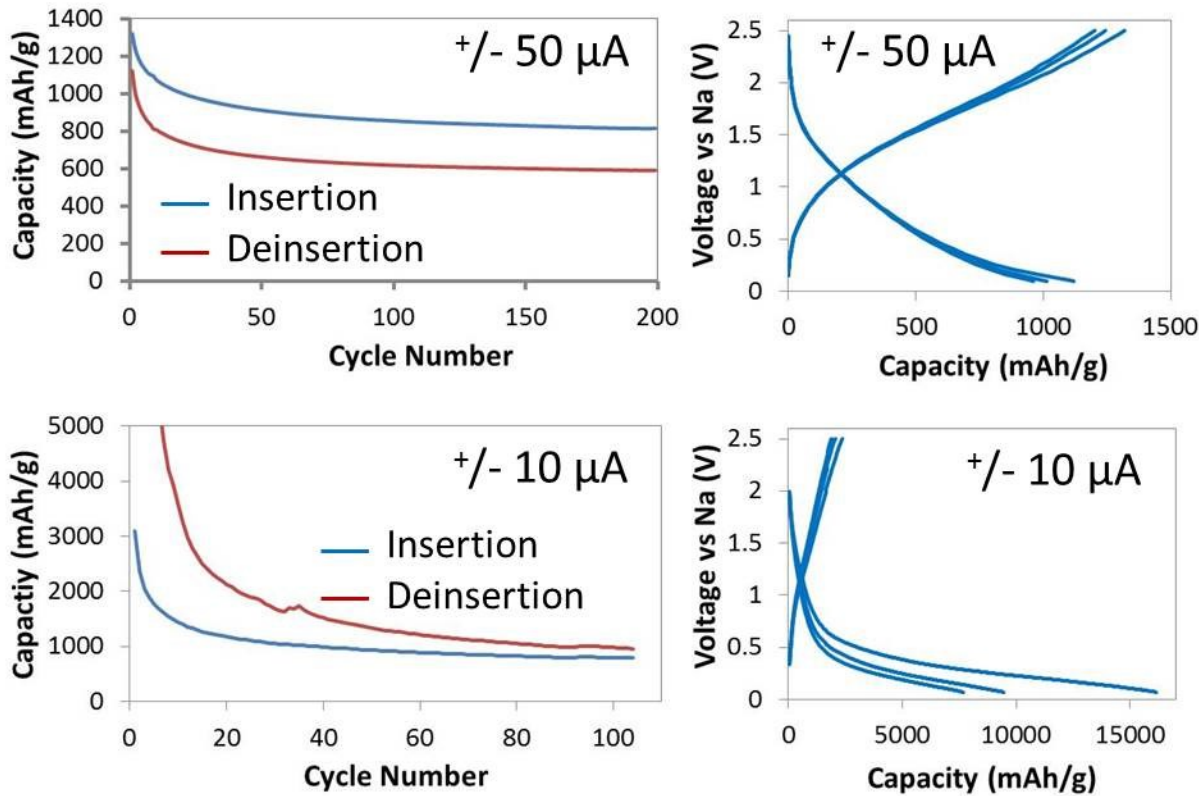


Figure 5.3. Galvanostatic cycling of porous silicon thin films in a sodium perchlorate flooded cell. In each case, the capacity over many cycles is shown on the left. To the right, the capacity for a selection of cycles is displayed. The slower rate of $10 \mu\text{A}$ leads to a much higher capacity in initial cycles, but only a slightly improved capacity approaching 100 cycles.

reached by cycling more slowly. This value is as high as could be seen in the Sb-C composite films, and much higher than seen for lead and Sb-Sn-C systems, and can likely be improved through optimization of cycling parameters, as judging by the poor efficiency and the high amount of cycle fading, which is not seen in the other materials.^{5,6} It will also be beneficial to explore Na-ion insertion at higher rates so as to better be able to compare to literature values.

The cyclic voltammetry and galvanostatic cycling data for potassium insertion into a porous silicon thin film is shown in Figure 5.4. Here the capacity seen on the CV scan is low, and there may not be discernable redox peaks present. The films were analyzed by galvanostatic cycling as well, and display a quick capacity fade to less than 10 mAh/g in only a few cycles. The galvanostatic data is featureless. Potassium has difficulty cycling in our silicon system.

Examining the possible causes for the low and fading capacity, and also the irreversible reaction, of sodium into porous silicon films, we first examine the redox potentials of sodium in comparison to lithium. The relative energies of the alkali metal redox couples changes as the electrolyte solvent changes.¹⁷ The values most commonly referred to are those in water, where Li/Li⁺ is 0.34 V below Na/Na⁺, but only 0.12 V below the K/K⁺ couple. However, in propylene carbonate, which we have used for our measurements, the relative voltages of the sodium and potassium couples are lower relative to the lithium redox couple. Na/Na⁺ is only 0.2 V above Li/Li⁺, and the K/K⁺ couple actually sits at a voltage of almost 0.1 V *below* the Li/Li⁺ couple.¹⁷ The lower voltages of sodium and potassium in the solvents used by battery electrolytes is advantageous for their respective battery systems. Additionally, the similarity in reduction potentials between Li⁺ and Na⁺

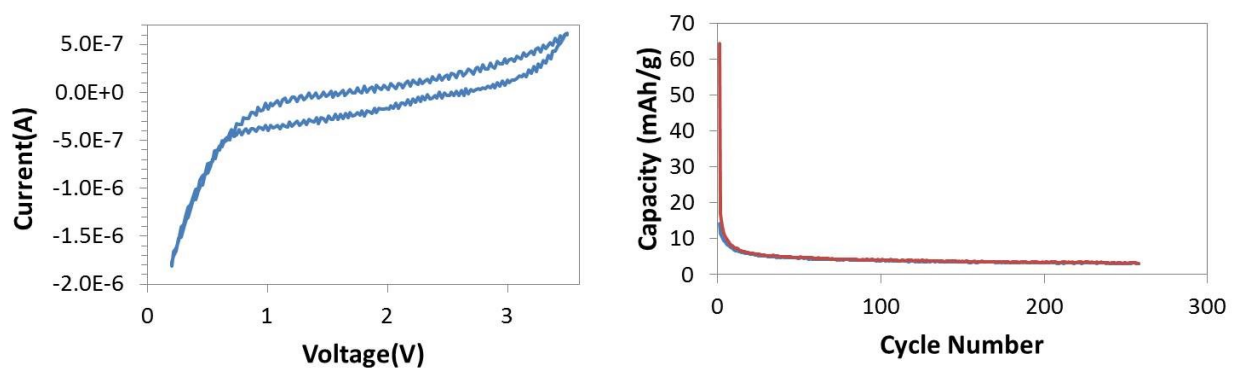


Figure 5.4. (left) cyclic voltammogram and (right) galvanostatic cycling of a porous silicon thin film in potassium perchlorate. Capacities are negligible beginning in early cycles.

makes it unlikely that the reactivity of the metal is correlated to the differing insertion properties in silicon.

Now that the reduction potentials have been examined and found similar, the solubilities of liquid sodium and lithium in silicon can be compared. Their solubilities in solid silicon at elevated temperatures can be compared to gauge their relative ease of electrochemical insertion at room temperature. At the lowest temperatures examined for sodium, crystalline P-type silicon (10^2 Ohm-cm) in contact with liquid sodium dissolved a constant 2.4×10^{-5} atom fraction from 570 to 650°C .¹⁸ In contrast, at only 398°C , silicon dissolves 0.002 atom percent lithium from a molten reservoir.¹⁹ At a more comparable 590 or 600°C (measurements by 2 separate groups), the solubility is even higher, and silicon dissolves between 0.009 and 0.016 atom percent lithium.¹⁹ The solubility of lithium in silicon appears to be on the order of 1000 times higher than that of sodium.

In addition to the solubility in already crystallized silicon, the thermodynamically stable Na-Si phases available for synthesis from Na and Si precursors can be examined from partial phase diagrams.¹⁸ Using solid state synthesis methods, the first stable mixed phase crystalizes at around 50 mole percent Na, at high pressures, in a silicon zintyl phase. This zintyl phase decomposes into a variety of lower-sodium silicon phases, which are not formed directly from sodium and silicon precursors. Of these phases, the lowest Na-containing phase is $\text{Na}_4\text{Si}_{23}$, at 15% Na. It is difficult to tell whether, when inserting sodium electrochemically, these lower sodium phases would form, or if a disordered state would exist up to the formation of the zintyl phase near 50%. At sodium concentrations below 15%, a nonstoichiometric phase exists, which may be a solid

solution. Upon de-insertion of sodium from the zintyl phase, the lower sodium content phases would be more likely to play a role since they form thermodynamically upon the decomposition of the zintyl phase.

A favorable comparison to the lithium-silicon system depends on whether the 15% or the 50% Na phase is the first formed electrochemically. In a lithium insertion into silicon, the first stable phase is $\text{Li}_{12}\text{Si}_7$, which is 36.8% Li.¹⁹ This leads to a large range for easy lithium intercalation. If the sodium system stays disordered until 50%, it may have a larger insertion range than the Li system. If the sodium system forms a new crystalline phase at 15%, it would have a much smaller range for easy, non-phase-forming insertion. At around 600 mAh/g, we're only inserting about 8×10^{-4} mole fraction of Na now, so optimization of the system should allow for much higher capacities.

Additionally, the phases and local atomic structure of silicon upon lithiation/delithiation have been examined in depth by pair distribution function analysis and NMR.¹⁵ It was found that upon initial lithiation of crystalline silicon, the breakup and amorphization of the silicon framework was kinetically slow, such that clusters of silicon were lithiated preferentially to further lattice breakdown. During this electrochemical lithiation, the thermodynamic lithium-silicon phases do not form at each thermodynamic Li:Si ratio, due to remaining silicon lattice bonds. Instead, no crystalline lithium-silicon phases appear until complete amorphization of the silicon lattice (<50 mV).¹⁵ The total amorphization of the silicon lattice is the limiting step to electrochemical lithiation, and is likely to be the limiting step in electrochemical insertion of other alkali metals. Overcoming this limiting step may be a problem for alkali metals with lower solubilities and fewer

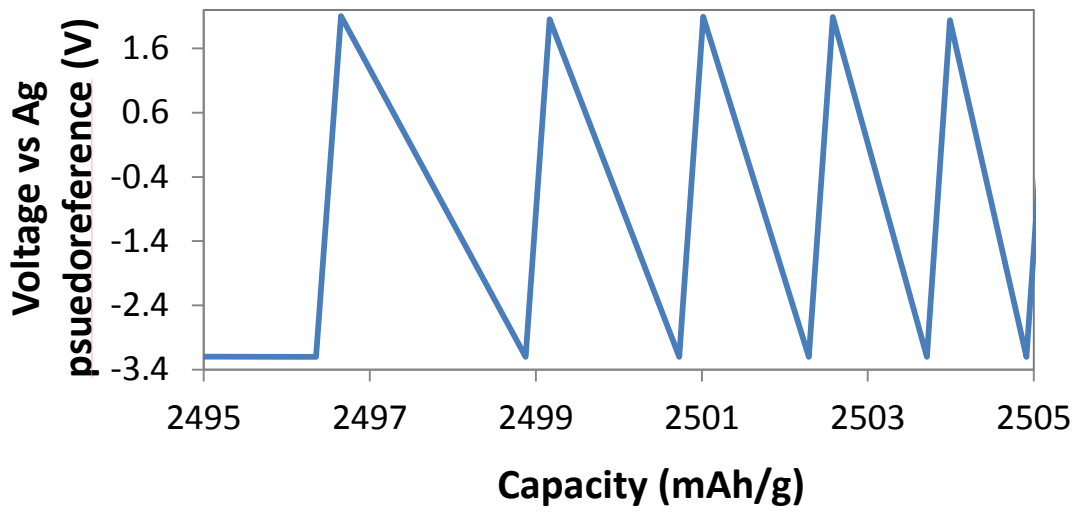


Figure 5.5. Galvanostatic cycling of a porous silicon thin film in a magnesium perchlorate flooded cell, at 10 μ A. The film showed a negligible capacity, with only ~ 1 mAh/g per cycle.

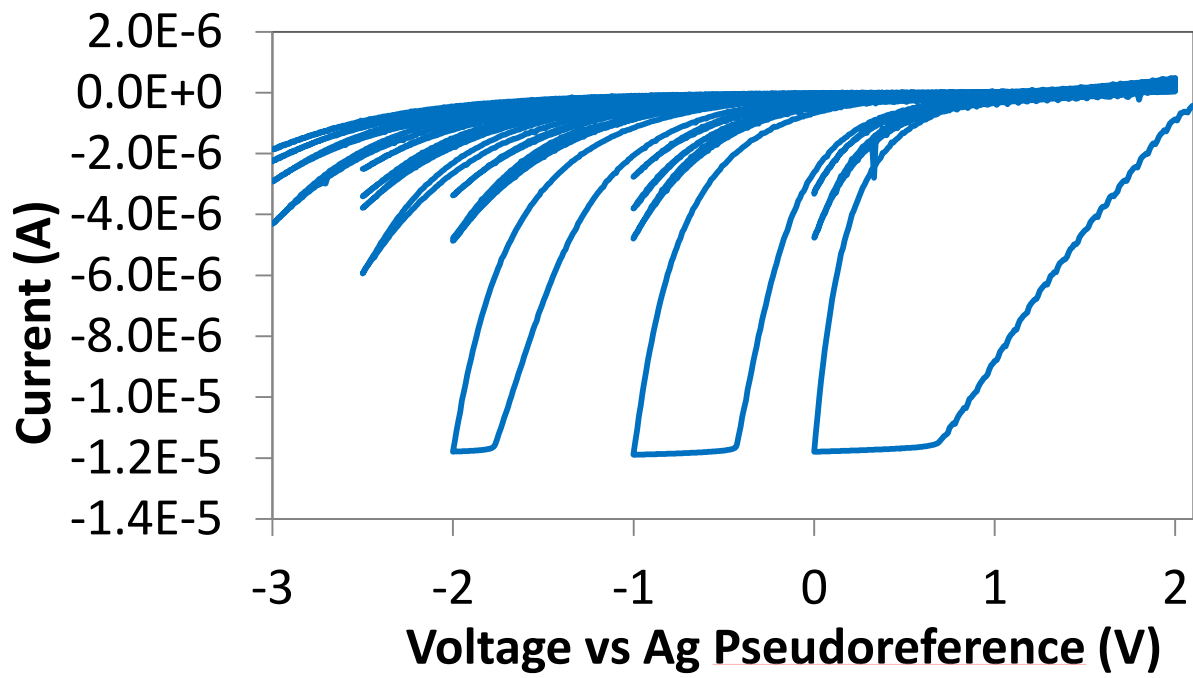


Figure 5.6. Cyclic voltammogram of a porous silicon thin film in a magnesium perchlorate flooded cell. The material was cycled three times at each voltage window: from 2 V to 0 V, to -1 V, to -2 V, to -2.5 V, and to -3 V. On the first cycle of each of the voltage windows above -2 V, the SEI layer forms. Each time negligible current is seen on the oxidation sweep, suggesting that the reduction current is from an irreversible process, such as SEI formation, and not due to magnesium insertion. On the second and third cycle, no current is seen on either sweep, suggesting that the silicon surface has grown a self-limiting SEI at these voltages. However upon increasing the reductive voltage, a new SEI-forming region is exposed. Once below -2 V vs the Ag pseudoreference, SEI formation is finished and no further capacity is seen.

thermodynamiclly in silicon than lithium.

The cycle depth of lithiation affects the subsequent cycling as well. In a shallow lithiation cycle, down to 85 mV, many spreadout isolated Si clusters remain. Upon subsequent delithiation, the remaining clusters nucleate and the silicon lattice partially reforms.¹⁵ However, silicon lithiated all the way past the amorphous state, until silicon atoms are isolated and crystalline $\text{Li}_{15}\text{Si}_4$ forms, follows a different pathway upon delithiation. Only a few Si clusters form, and amorphous Si domains grow from these.¹⁵ The amorphous silicon is a new material for lithiation for subsequent cycles, and follows a different, kinetically easier, lithiation pathway. If it were true that alkali metals with lower solubilities may have difficulty fully inserting into silicon, it would follow that such metals may not be able to insert fully, causing subsequent cycles to be kinetically more impeded. The silicon would not become nearly as amorphous as it does following a full (<50 mV) lithium insertion, hindering insertion in later cycles. This may explain the irreversible reaction observed for Na^+ insertion, and the difficulty of observing insertion for K^+ .

5.3.4 Electrochemical Exploration of the Divalent Cation Mg^{2+}

In Figure 5.5, a negligible galvanostatic capacity of Mg^{2+} in Si can be seen. By the second cycle, the capacity has fallen below 2 mAh/g. Not enough points were taken in order to examine the shapes of the insertion/de-insertion traces for such small capacities. Cyclic voltammetry was used to examine the voltage dependence of the low capacities, as shown in in Figure 5.6. The films were cycled three times at the voltage window of 2-0 V vs the Ag pseudoreference. In the first cycle, a large peak was observed in the reductive sweep. No corresponding

oxidation was seen on the reverse sweep, suggesting SEI formation or another side reaction. In the next 2 cycles in the same voltage window, no oxidation or reduction was observed, suggesting the SEI was fully formed for that voltage window. Upon increasing the voltage window of 2 to -1 V, a reduction peak was observed in the new portion of the voltage window, again with no corresponding oxidation peak, and no current observed on the second or third cycle. This also corroborates SEI formation, as more SEI will form when the voltage is lowered for the first time. Again the voltage window was expanded, to 2 to -2 V, and again SEI formation was seen on the reducing sweep. As the window was expanded below -2 V, the SEI formation had finished, and no further features were visible. When the CV extends to -5.3 V vs the Ag pseudoreference, Mg begins to plate (not shown).

Optimization of the Mg insertion should lead to improved performance, if the insertion correlates with the miscibility suggested from the tentative Mg-Si phase diagram.²⁰ The first thermodynamically stable phase does not occur until a Mg concentration of 33%, giving a possible window for easy Mg insertion on the order of the Li-Si system (36.8% Li).

Extending the correlation of high temperature solubility with room temperature electrochemical insertion, the solubility of magnesium in silicon is examined. At the lowest temperature explored, 940°C, silicon dissolves between 0.8×10^{-4} and 0.9×10^{-4} atom percent Mg. At lower temperatures, such as 650°C, where values are listed for Li and Na solubilities, the solubility of Mg would be even lower. This may explain the trouble observing electrochemical insertion of Mg into crystalline silicon.

To explore this possibility, a porous silicon film was pre-lithiated by galvanostatic cycling in a lithium perchlorate flooded cell (Figure 5.7). The SEI

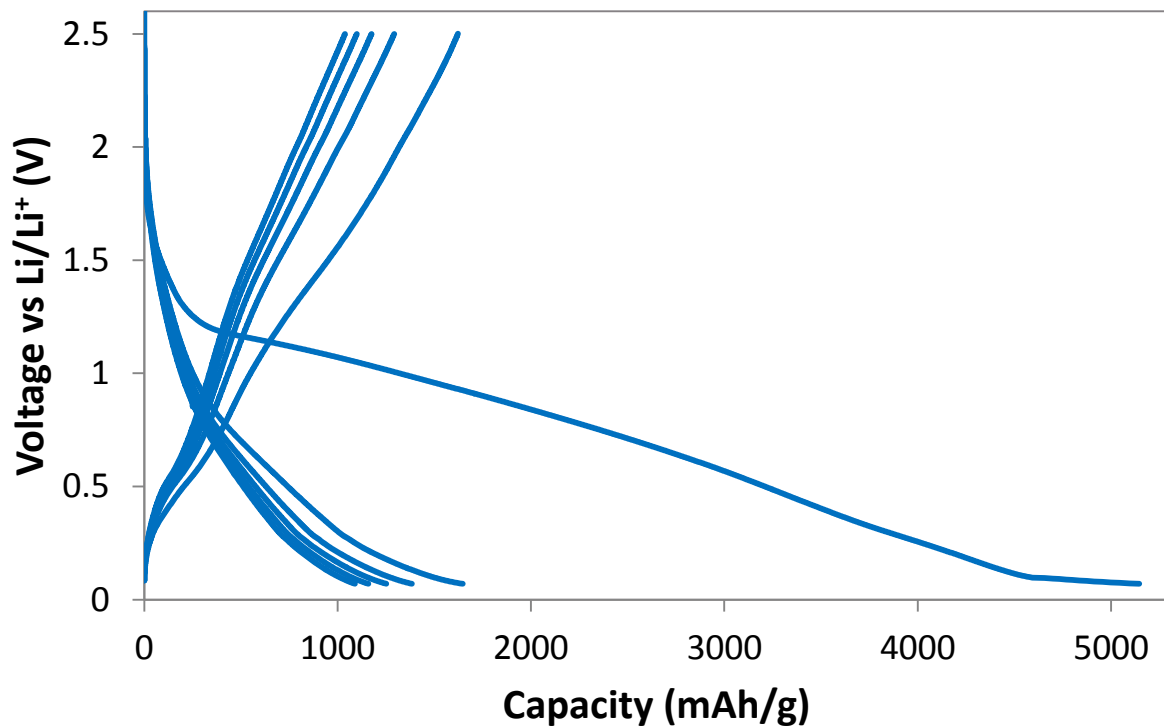


Figure 5.7. Pre-lithiation by galvanostatic cycling of a porous silicon thin film in lithium perchlorate, including the initial SEI-forming step. By the third cycle, the film is expected to be amorphous. After 5 cycles, the film was lithiated one final time (shown).

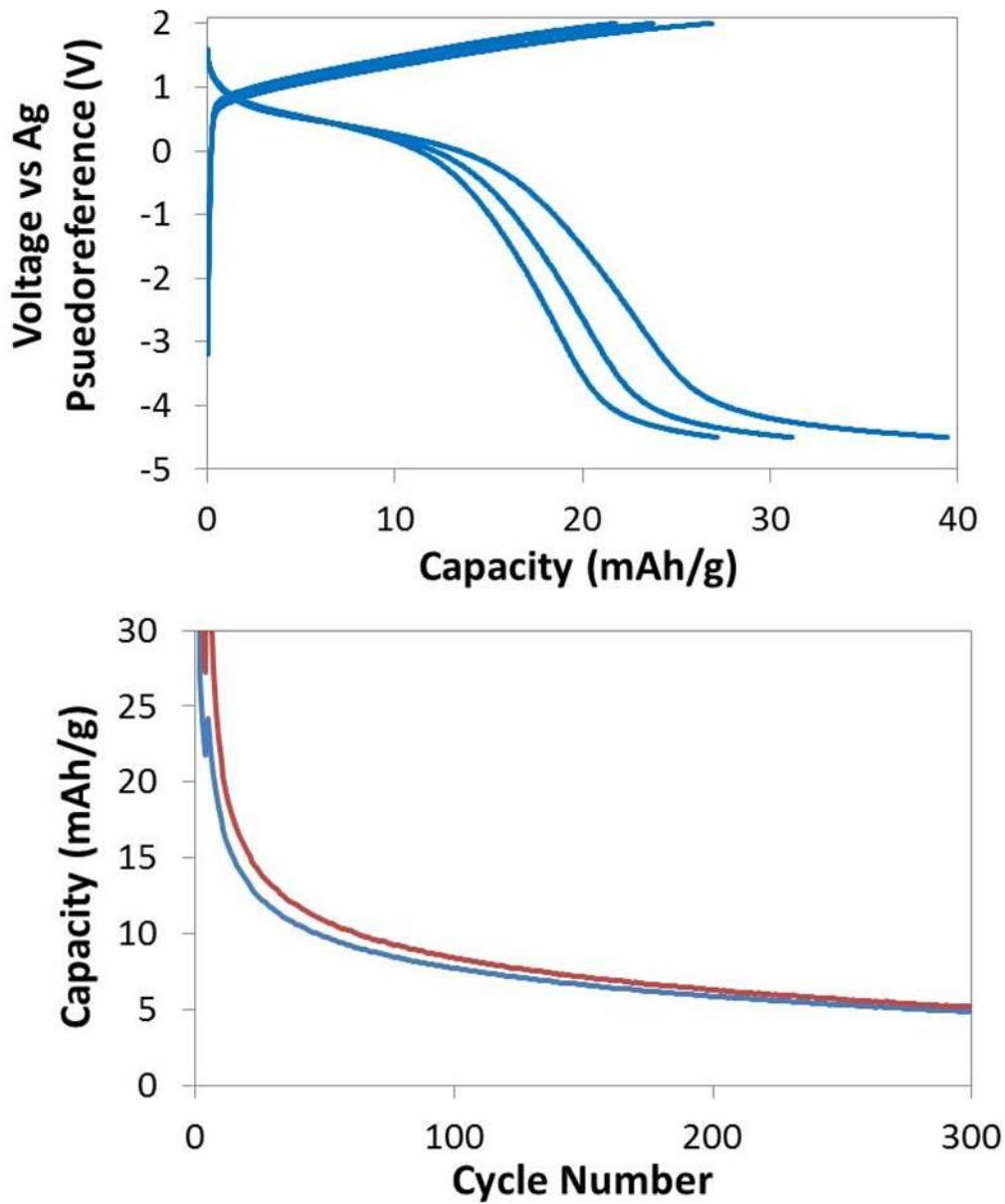


Figure 5.8. Galvanostatic cycling of a porous silicon thin film that has been pre-lithiated and is amorphous. The film underwent an oxidation step in the magnesium perchlorate before cycling to remove lithium, and the film was held at 2 V vs the Ag pseudoreference in order to ensure all of the lithium was removed. An improved Mg capacity is seen compared to silicon films that are crystalline and have not been pre-lithiated.

layer was formed in the lithium perchlorate cell, and the film was cycled (lithiated and de-lithiated) 5 times in order to insure that the silicon was amorphous. Following the cycling, the film was lithiated one final time, and the sample was removed from solution, rinsed with clean PC, and used immediately in a flooded cell filled with magnesium perchlorate for magnesium insertion.

The pre-lithiated silicon showed a greatly improved Mg capacity (Figure 5.8). Initial cycles show a reversible Mg capacity of over 20 mAh/g, quickly dropping down to 5 mAh/g in later cycles. The lithiated silicon was oxidized at 50 μ A until a voltage of 2 V vs the Ag pseudoreference was reached in the magnesium perchlorate before cycling to remove the lithium. In order to ensure the film was de-lithiated, it was held at 2 V vs the Ag pseudoreference for an additional 2 minutes. The pre-lithiated films display 2 voltage plateaus in the galvanostatic data, where none were visible in films that were not pre-lithiated. These 2 plateaus correspond to 2 different chemical reactions, a higher voltage, reversible insertion step, and a nonreversible lower voltage step. The lower voltage plateau corresponds to the voltage at which magnesium appears to plate the electrodes by cyclic voltammetry.

5.4 Conclusions

It was expected that porous silicon would be a versatile anode for many battery chemistries, due to the alloying mechanism of cation insertion and the cycling stability imparted by the porous structure. However, poor initial electrochemical performance was observed with Na^+ , K^+ , and Mg^{2+} insertion. It was noted that the kinetically difficult step of Li^+ insertion into Si was the breaking

of the Si lattice into isolated Si atoms. After this step, the Si was amorphous and cycling was less hindered. Using solubility alloying data to infer relative ease of electrochemical alloying, it was observed that the alloying of Li should be orders of magnitude easier than the alloying of Na, K, and Mg. This led to the demonstration that a pre-lithiated, amorphous Si film has greatly improved cycling performance with Mg^{2+} than a crystalline Si film that has not been pre-lithiated.

This observation is very useful for future experiments. It would be interesting to see if increased cycling efficiency of lithium is seen for cycling below 50 mV vs Li, as that leads to the complete separation of Si atoms, and a completely amorphous sample. It may be that even a single low voltage cycle would increase the performance of future cycling behavior. It would also be interesting to repeat the Mg insertion experiment for lithiation < 50 mV, and to extend the pre-lithiation study to Na and K systems.

5.5 References

1. Scrosati, B. Power sources for portable electronics and hybrid cars: lithium batteries and fuel cells. *Chem. Rec.* **5**, 286–297 (2005).
2. Padhi, A. _ K., Nanjundaswamy, K. S. & Goodenough, J. B. d. Phospho-olivines as Positive-Electrode Materials for Rechargeable Lithium Batteries. *J. Electrochem. Soc.* **144**, 1188–1194 (1997).
3. Richman, E. K., Kang, C. B., Brezesinski, T. & Tolbert, S. H. Ordered Mesoporous Silicon through Magnesium Reduction of Polymer Templatated Silica Thin Films. *Nano Lett.* **8**, 3075–3079 (2008).

4. Qian, J. *et al.* High capacity Na-storage and superior cyclability of nanocomposite Sb/C anode for Na-ion batteries. *Chem. Commun.* **48**, 7070 (2012).
5. Xiao, L. *et al.* High capacity, reversible alloying reactions in SnSb/C nanocomposites for Na-ion battery applications. *Chem. Commun.* **48**, 3321 (2012).
6. Jow, T. R., Shacklette, L. W., Maxfield, M. & Vernick, D. The role of conductive polymers in alkali-metal secondary electrodes. *J. Electrochem. Soc.* **143**, 1730–1733 (1987).
7. Eftekhari, A. Fabrication of all-solid-state thin-film secondary cells using hexacyanometallate-based electrode materials. *J. Power Sources* **132**, 291–295 (2004).
8. Wessells, C. D., Peddada, S. V., Huggins, R. A. & Cui, Y. Nickel Hexacyanoferrate Nanoparticle Electrodes For Aqueous Sodium and Potassium Ion Batteries. *Nano Lett.* **11**, 5421–5425 (2011).
9. Singh, N., Arthur, T. S., Ling, C., Matsui, M. & Mizuno, F. A high energy-density tin anode for rechargeable magnesium-ion batteries. *Chem. Commun.* **49**, 149 (2013).
10. Aurbach, D. *et al.* A comparison between the electrochemical behavior of reversible magnesium and lithium electrodes. *J. Power Sources* **97-98**, 269–273 (2001).
11. Aurbach, D. *et al.* Prototype systems for rechargeable magnesium batteries. *Nature* **407**, 724–727 (2000).

12. Muldoon, J. *et al.* Electrolyte roadblocks to a magnesium rechargeable battery. *Energy Environ. Sci.* **5**, 5941 (2012).
13. Allgaier, J., Poppe, A., Willner, L. & Richter, D. Synthesis and characterization of poly [1, 4-isoprene-b-(ethylene oxide)] and poly [ethylene-co-propylene-b-(ethylene oxide)] block copolymers. *Macromolecules* **30**, 1582–1586 (1997).
14. Hillmyer, M. A. & Bates, F. S. Synthesis and characterization of model polyalkane-poly (ethylene oxide) block copolymers. *Macromolecules* **29**, 6994–7002 (1996).
15. Key, B., Morcrette, M., Tarascon, J.-M. & Grey, C. P. Pair distribution function analysis and solid state NMR studies of silicon electrodes for lithium ion batteries: Understanding the (de)lithiation mechanisms. *J. Am. Chem. Soc.* **133**, 503–512 (2011).
16. Sun, Y. *et al.* Direct atomic-scale confirmation of three-phase storage mechanism in $\text{Li}_4\text{Ti}_5\text{O}_{12}$ anodes for room-temperature sodium-ion batteries. *Nat. Commun.* **4**, 1870 (2013).
17. Wibowo, R., Aldous, L., Jones, S. E. W. & Compton, R. G. The electrode potentials of the Group I alkali metals in the ionic liquid N-butyl-N-methylpyrrolidinium bis(trifluoromethylsulfonyl)imide. *Chem. Phys. Lett.* **492**, 276–280 (2010).
18. Songster, J. & Pelton, A. D. The Na-Si (sodium-silicon) system. *J. Phase Equilibria* **13**, 67–69 (1992).
19. Okamoto, H. The Li-Si (lithium-silicon) system. *Bull. Alloy Phase Diagr.* **11**,

306–312 (1990).

20. Franke, P. & Neushutz, D. 2 binary systems: Mg-Si. in *Bin. Syst. Part 3 Bin. Syst. Cs-K Mg-Zr* **19B3**, 1–3 (Springer Berlin Heidelberg, 2005).

CHAPTER 6

Conclusions

This work demonstrated the versatile impact that nano-architected materials have on material properties for energy storage applications. High surface areas, exposed nanoparticle surfaces, and open space are useful for the addition of energy and power densities, allowing for wiring of electrolyte and ions through the materials, and allowing for increased flexibility of materials in terms of handling volume changes.

We designed and constructed an instrument suitable for the deposition of polymeric coatings over 3D electrodes for a new class of microbattery. 3D microstructured electrodes have higher surface areas that enable sufficient energy densities per footprint in microbatteries. These electrodes require the deposition of a conformal solid state electrolyte coating in order to operate as a component of a full battery. Our instrument for plasma deposition was optimized for the deposition of PEO-like films from vapor-phase tetraglyme. The RF power source and power delivery to the chamber was optimized to allow for reproducible plasma ignition and polymeric deposition. The gas manifold was designed to give full control over deposition parameters. It was crucial that a region in parameter space be found to allow for retention of precursor functionality.

We used the instrument to deposit PEO-like films which we examined by impedance spectroscopy for their merit as electrolyte coatings. We first optimized the depositions such that the films were reproducible in thickness and chemical

composition. The depositions were further optimized to produce PEO-like films, by finding the allowable parameter window of plasma power, chamber pressure and temperature, precursor flow rate, and deposition distance from the plasma discharge. Some films were deposited over an adhesion layer, and the effect of the adhesion layer on the ionic conductivity was examined by impedance spectroscopy. It was found that films with no adhesion layer or films deposited over a 1 s adhesion deposition showed acceptable ionic conductivities at all Li-ion concentrations examined. Films with thicker adhesion layers only show limited ionic conductivities.

In a separate application, it was found that expressing maghemite iron oxide in a high surface area aerogel produces a material that functions as a cathode for Li-ion batteries. The defects in un-doped iron oxide lie primarily on the surface, and so are amplified by creating iron oxide in a form that is mostly surface. Highly defective iron oxides are known to have enhanced Li-ion storage. We examined the processing conditions for the aerogel, and found that heating in air allowed for the retention of surface area and defects, and optimized the capacity and cycle life of the material. We achieved reversible capacities over 100 mAh/g.

Additionally, we have found that when using a nanoporous architecture, silicon potentially functions as the anode for a variety of battery chemistries. Porous silicon has shown great promise in extending the cycle life of silicon as an anode for Li-ion batteries. We examined the intercalation of Na^+ , K^+ , and Mg^{2+} and found small capacities for Na^+ intercalation, and negligible capacities for K^+ and Mg^{2+} insertion. However, preliminary studies have shown that pre-lithiation of the crystalline silicon to give amorphous silicon greatly enhances the Mg^{2+} capacity,

when the silicon is in a nanoporous architecture. It seems likely given the kinetic barrier of the silicon transition from the crystalline to the amorphous state, and the much higher solubility of Li in crystalline silicon than the other elements examined, that optimization of the pre-lithiation process would allow for higher capacities for all three elements.